PSFC/RR-99-8

RF Edge Physics on the Alcator C-Mod Tokamak

James C. Reardon

May 1999

This work was supported in part by the U. S. Department of Energy Contract No. DE-FC02-99ER54512. Reproduction, translation, publication, use and disposal, in whole or in part by or for the United States government is permitted.

RF Edge Physics on the Alcator C-Mod Tokamak

by

James Christian Reardon

B.S. Physics, B.S. Astronomy, B.A. English, University of Maryland (1988)

Submitted to the Department of Physics
in partial fulfillment of the requirements for the degree of

Doctor of Philosophy in Physics

at the

MASSACHUSETTS INSTITUTE OF TECHNOLOGY

June 1999

Author .....
Department of Physics
May 3, 1999

Certified by .....
Professor Miklos Porkolab
Director of the Plasma Science and Fusion Center
Thesis Supervisor

Accepted by .....
Thomas J. Greytak
Associate Department Head for Education

RF Edge Physics on the Alcator C-Mod Tokamak

by

James Christian Reardon

Submitted to the Department of Physics
on May 3, 1999, in partial fulfillment of the
requirements for the degree of
Doctor of Philosophy in Physics

Abstract

Alcator C-mod is a compact, high-field, RF-heated tokamak which has been operational since 1993. RF heating uses the fast magnetosonic wave at the fundamental frequency of the minority ion species. The behavior of the fast wave is studied using probes located in the plasma edge. A fast-reciprocating Langmuir probe unaffected by RF was built and used to measure the modification of the plasma edge caused by RF and by RF-induced H-mode. The plasma edge was seen to not significantly change during RF, but the electron density decreased during H-mode by a factor of 2. Comparison with another fast-reciprocating probe revealed substantial variations of electron temperature and density along magnetic field lines outside the separatrix. The ion saturation current density profile implies that about 50 kW of RF is dissipated in the edge due to RF sheaths surrounding the antennas and the limiters. A second diagnostic, an array of loop probes mounted behind tiles on the inner wall opposite one of the RF antennas, was built and installed to measure the fraction of power transmitted through the plasma. This was seen to vary with minority concentration during D(H) heating at 5.4 T but not during D(^{3}He) heating at 8 T. The probe measurement agreed very well with the prediction of the full-wave code FELICE, and with an analytic theory of single-pass absorption, extended to include the effect of an internal resonator on the low-field side of the central evancescent layer. During shots the probe signal was seen to vary synchronously with the sawtooth instability in the plasma center. The sense of this variation reversed as the minority concentration in D(H) was raised, in accordance with the analytic theory. The Parametric Decay Instability (PDI) was observed on a third diagnostic, a pre-existing set of Langmuir probes on poloidal limiters. The observance of PDI during magnetic field ramps was correlated with the passage of the $f_{RF} = 3f_{CD}$ cyclotron harmonic layer by the antenna Faraday Screen, and with the observation of energetic Deuterium flux by the Charge Exchange diagnostic, but not with the observation of impurities.

Thesis Supervisor: Professor Miklos Porkolab
Title: Director of the Plasma Science and Fusion Center

Acknowledgments

I received assistance from every member of the C-Mod group. From Richie Danforth, Bob Sylvia, Bill Keating, Charles Cauley, and Steve Tambini I received patient instruction in the craft of machining stainless steel. In Ed Fitzgerald I had a model of resourcefulness. Jack Nickerson, Bill Beck and Tom Toland helped me get things done. From Steve Kochan, Bob Childs, and Tom Hsu I received education in the principles of mechanical design, while Bill Parkin showed me how to troubleshoot electronic circuits. Dave Arsenault taught me how to weld. From Sam Pierson, Andy Pfeiffer, and Rick Murray I learned the necessity of maintaining a hopeful attitude during the demands of work. From Frank Silva, dedication to duty and the need to keep things moving. From Josh Stillerman, the usefulness of thinking quickly when dealing with computers. Steve Fairfax and Dave Gwinn were patient in explaining the power systems and engineering, from the top down.

My thesis advisor, Professor Miklos Porkolab, made sure that I never had to worry about funding and that I was able to get run time when I needed it. I thank him in addition for scientific discussions which kept this thesis on track. Steve Golovato started me on this dissertation work. Yuichi Takase and Paul Bonoli initiated me into the mysteries of RF. Brian LaBombard introduced me to edge physics. I profited greatly from discussions about RF with Steve Wukitch. I thank Rejean Boivin, Prof. Ambrogio Fasoli, Catherine Fiore, John Goetz, Bob Granetz, Martin Greenwald, Jim Irby, Bruce Lipschultz, Spencer Pitcher, John Rice, Joe Snipes, Jim Terry, and Steve Wolfe for the time they spent in scientific discussions concerning this dissertation. I thank my readers, Earle Lomon and Earl Marmar.

I salute my fellow students on C-Mod, Peter O'Shea, Darren Garnier, Chris Rost, Rob Nachtrieb, Paul Stek, Daniel Lo, Cindy Christensen, Alex Mazurenko, Jeff Schachter, Chris Kurz, Joe Sorci, Thomas Pedersen, Maxim Umansky, Dmitri Pappas, and Jim Weaver; Yijun Lin, Eric Nelson-Melby, Yongkyoon In, Chris Boswell, Howard Yuh, Teresa Tutt, and Davis Lee.

I thank my parents, John D. Reardon and Mary Lynn Reardon, with all of love.

Contents

Chapter 1

Introduction

This dissertation describes research into magnetically confined fusion grade plasmas. It has been funded entirely by the US government (Department of Energy, contract DE-AC02-78ET51013). Magnetically confined plasmas are a possible source of energy, and could replace fossil fuels as the main source of energy for the nation's power grid. Current experiments do not, however, produce energy. Magnetically confined plasmas which can be produced in the lab are generally quite different than magnetically confined plasmas which are found in nature, and experiments such as the Alcator C-Mod tokamak are designed to learn facts about magnetically confined plasmas which will one day be used to design an energy-producing reactor. In particular, it seems likely that a reactor will have to have RF heating of some type. The subject of this dissertation is that subset of interactions of RF waves and fusion-grade plasmas which can be observed by probes located just outside the plasma edge.

1.1 Important Plasma Parameters

The most important plasma parameters are the plasma density, the plasma temperature, and the magnetic field. From these may be calculated a set of characteristic length and time scales which often give insight into complex situations. A complete summary of plasma parameters, including many not described below, is given in the

Plasma Formulary published by the Naval Research Laboratory[1] [1]. A good introduction to plasma physics is **Introduction to Plasma Physics and Controlled Fusion** [2], by Chen, who illustrates the exposition with diagrams and data from important experiments.

1.1.1 Cyclotron motion

Individual ions and electrons gyrate around magnetic field lines as a result of the Lorentz force law

$$\mathbf{F} = q(\mathbf{E} + \mathbf{v} \times \mathbf{B}), \tag{1.1}$$

which implies gyrofrequencies

$$\omega_{ci} = \frac{q_i B}{m_i}, \quad \omega_{ce} = \frac{q_e B}{m_e} \tag{1.2}$$

referred to as the ion and electron *cyclotron frequencies.* Numerically $\omega_{ce} = 28$ GHz/T.

1.1.2 Thermal Velocity

The random motions of particles in the plasma are often found to satisfy a Maxwellian distribution of velocities, given in one dimension by the distribution function

$$f = n_j \sqrt{\frac{m_j}{2\pi k T_j}} \; e^{-\frac{mv^2}{2kT_j}}, \tag{1.3}$$

which defines the thermal velocity

$$v_t = \sqrt{\frac{kT_j}{m_j}}, \tag{1.4}$$

where j refers to a particular species (ion, electron). Different species have different temperatures; quasineutrality usually enforces $n_e = \sum Z_j n_j$. The distribution

[1] Also available at http://www.spp.astro.umd.edu/htmls/formula/toc.html

functions are often Maxwellian even in situations where the mean free path between particle collisions is much longer than the size of the plasma.

1.1.3 Larmor Radius

A particle moving with a thermal velocity orbits a magnetic field line at a radius

$$r_{Lj} = \frac{v_{tj}}{\omega_{cj}} = \frac{\sqrt{m_j k T_j}}{q_j B}. \tag{1.5}$$

Ion orbits are generally larger than electron orbits.

1.1.4 Plasma Oscillations

Consider an infinite homogenous plasma of massive ions and electrons, in which the number density of electrons is n_e. If a slab of electrons is displaced by a small distance δ relative to the ions, it will experience a Coulomb restoring force which is linear in δ, leading to oscillations with frequency

$$\omega_p e = \left(\frac{ne^2}{m\epsilon_0}\right)^{1/2}. \tag{1.6}$$

This is called the *electron plasma frequency.* An anologous frequency may be defined for the ions.

1.1.5 Debye Shielding

Plasmas shield out externally imposed electric fields on a length scale

$$\lambda_d = \left(\frac{\epsilon_0 k T_e}{ne^2}\right)^{1/2}. \tag{1.7}$$

This can be recognized as the ratio of the thermal velocity to the plasma frequency.

1.2 Magnetic Confinement of Plasma

A plasma consists of a large number of mutually interacting independent particles, yet the knowledge of the interaction potential, which is the Coulomb potential

$$\phi = \frac{1}{4\pi\epsilon_0}\frac{Ze^2}{r} \tag{1.8}$$

for the interaction of two charges e, Ze, gives little insight into the behavior of the plasma, which is dominated by collective effects. The discrete nature of the charges can often be neglected, and the plasma treated as a magnetoactive fluid. A self-consistent model has been developed to describe this magnetoactive fluid, called *ideal magnetohydrodynamics*. The standard guide to ideal MHD is **Ideal Magnetohydrodynamics** [3] by Freidberg. This model includes oscillations slower than ω_{pe} and of longer wavelength than λ_d. For faster modes, or shorter wavelengths, a different analysis is required, often perturbative in nature; see **The Theory of Plasma Waves** [4], by Stix.

1.2.1 Ideal MHD

The equations of ideal MHD are given by [3]:

$$\frac{\partial\rho}{\partial t} + \nabla\cdot\rho\mathbf{v} = 0 \qquad \text{continuity} \tag{1.9}$$

$$\rho\frac{d\mathbf{v}}{dt} = \mathbf{J}\times\mathbf{B} - \nabla p \qquad \text{force balance} \tag{1.10}$$

$$\frac{d}{dt}\left(\frac{p}{\rho^\gamma}\right) = 0 \qquad \text{equation of state} \tag{1.11}$$

$$\mathbf{E} + \mathbf{v}\times\mathbf{B} = 0 \qquad \text{Ohm's law} \tag{1.12}$$

$$\nabla\times\mathbf{E} = -\frac{\partial\mathbf{B}}{\partial t} \qquad \text{Faraday's law} \tag{1.13}$$

$$\nabla\times\mathbf{B} = \mu_0\mathbf{J} \qquad \text{Ampere's law} \tag{1.14}$$

$$\nabla\cdot\mathbf{B} = 0 \qquad \text{no magnetic monopoles} \tag{1.15}$$

These equations describe a single fluid of mass density ρ and pressure p, which moves with velocity $\mathbf{v}$, and is electrostatically neutral. In the ideal MHD model the plasma and the field move together, the field lines acting as mass-loaded strings, so the field is said to be "frozen in" the plasma. ρ and p are constant on a field line.

The single-fluid equations of ideal MHD follow from the more general two-fluid equations, which describe independent ion and electron fluids, by taking the limits $m_e/m_i \rightarrow 0$ and $\epsilon_0 \rightarrow 0$, so that $\rho_i \rightarrow \rho$, $\mathbf{v}_i \rightarrow \mathbf{v}$, $p_e + p_i \rightarrow p$, and the displacement current is neglected. The two-fluid equations in turn follow from taking moments of the Boltzmann equation for each species α

$$\frac{\partial f_\alpha}{\partial t} + \mathbf{u} \cdot \nabla f_\alpha + \frac{q_\alpha}{m_\alpha}(\mathbf{E} + \mathbf{u} \times \mathbf{B}) \cdot \nabla_{\mathbf{u}} f_\alpha = \left(\frac{\partial f_\alpha}{\partial t}\right)_c \quad , \tag{1.16}$$

where f_α is the distribution function for species α and the right-hand side describes the effect of collisions. To arrive at the two-fluid equations, both fluids are assumed to be collision-dominated.

1.2.2 Equilibrium

The ideal MHD equations (Equations 1.9—1.15) satisfy the Virial Theorem, which has as a consequence that a plasma cannot be confined solely by the action of its own electric and magnetic fields [3]. A simple example of a plasma confined in equilibrium by external magnetic fields is given by the *theta pinch*, a one-dimensional configuration illustrated in Figure 1.1. An longitudinal magnetic field $\mathbf{B}$ is provided by external magnets. As the field is ramped up it induces a plasma current I_{plasma} in the azimuthal direction, which in turn creates a $\mathbf{J} \times \mathbf{B}$ force which is radially inward and confines the plasma. The theta pinch was the first magnetic confinement configuration to produce substantial amounts of fusion.

There are two problems with the theta pinch. The plasma is not confined in the longitudinal direction, and is free to leak out the ends of the device. The characteristic time to lose the plasma is $\tau \sim L/v_{ti} \sim 10$ μs for typical device length L. The second problem is that the equilibrium configuration is only neutrally stable: if the plasma

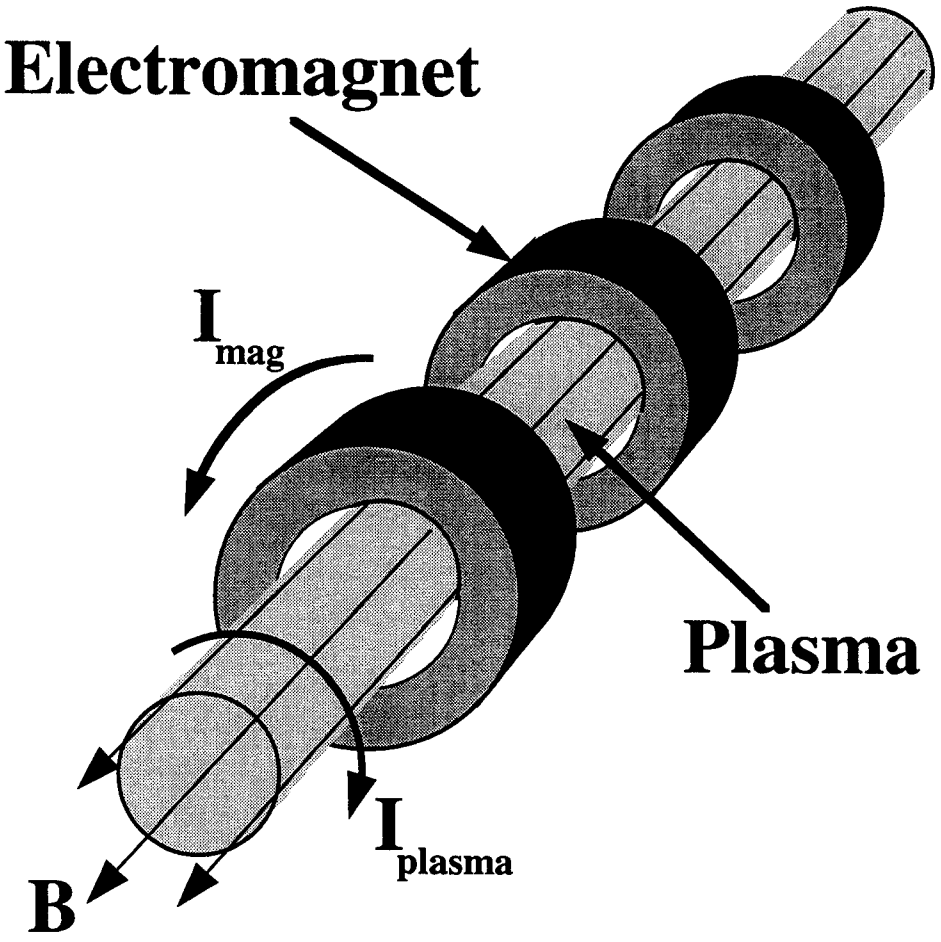

Figure 1.1: Diagram of Theta Pinch

column is displaced from the cylinder axis there is no restoring force, so that the plasma drifts into the vacuum vessel wall. The equilibrium is therefore sensitive to small field errors.

Both problems may be solved by bending the theta pinch into a torus (see Figure 1.2 for toroidal coordinates). The equilibrium of systems with toroidal symmetry is described by the Grad-Shafranov equation:

$$\Delta^* \psi = -\mu_0 R^2 \frac{dp}{d\psi} - F \frac{dF}{d\psi} \ , \tag{1.17}$$

where the elliptic operator Δ^* is

$$\Delta^* = R\frac{\partial}{\partial R}\left(\frac{1}{R}\frac{\partial \psi}{\partial R}\right) + \frac{\partial^2 \psi}{\partial Z^2}. \tag{1.18}$$

The pressure p and $F = RB_\phi$ are free functions of flux function ψ, defined by

$$B_R = -\frac{1}{R}\frac{\partial \psi}{\partial Z}, \qquad B_Z = \frac{1}{R}\frac{\partial \psi}{\partial R}. \tag{1.19}$$

Surfaces of constant ψ (*flux surfaces*) form a set of nested toroids.

1.2.3 Stability

Magnetically confined plasmas are beset by many instabilities which grow exponentially with time. These can be divided into two categories, the current-driven modes, dependent on the current $J_\parallel$ which flows parallel to the magnetic field, and the pressure-driven modes, which require a pressure gradient ∇p perpendicular to the magnetic field. The stability of a plasma configuration against a particular instability is determined by calculating the change in plasma free energy caused by the perturbation associated with the instability.

Consider a plasma equilibrium in which the magnetic field is $\mathbf{B} = \mathbf{B}(\mathbf{x})$. Suppose the plasma is displaced by a small amount $\xi = \xi(\mathbf{r})$ at time t=0. Since the field lines are frozen in, this is accompanied by a small change in the magnetic field $\mathbf{Q} = \nabla \times (\xi \times \mathbf{B})$. This will cause for example a small change in the magnetic field line tension $\kappa B^2/\mu_0$ ($\kappa = \mathbf{b} \cdot \nabla \mathbf{b}$). After considerable algebra, the free energy change is found to be [3]:

$$\delta W_F = \frac{1}{2}\int_P d\mathbf{r}\left[\frac{|\mathbf{Q}_\perp|^2}{\mu_0} + \frac{B^2}{\mu_0}|\nabla \cdot \xi_\perp + 2\xi_\perp \cdot \kappa|^2 + \gamma p\,|\nabla \cdot \xi|^2 - 2(\xi_\perp \cdot \nabla p)(\kappa \cdot \xi_\perp^*)\right.$$
$$\left. - J_\parallel(\xi_\perp^* \times \mathbf{b}) \cdot \mathbf{Q}_\perp\right]. \tag{1.20}$$

The first term is the energy required to bend magnetic field lines. The second corresponds to the increase in magnetic field energy caused by compressing the magnetic

field. The third term is the energy needed to compress the plasma adiabatically. These terms are always positive, and therefore serve to stabilized the plasma. The fourth and fifth terms can be positive or negative. When they are (individually) negative they correspond to the pressure-driven modes and current-driven modes, respectively, mentioned above.

1.3 The Tokamak

Both of the problems of theta pinches can be resolved by bending the theta pinch into a torus and causing the plasma to carry a current in the toroidal direction. This configuration is called a *tokamak* and is illustrated in Figure 1.2[2]. Toroidal coordinates are defined by r, θ, and ϕ, the minor radius, poloidal angle, and toroidal angle. Cylindrical coordinates are also often useful: R, Z, and ϕ, the major radius, height above midplane, and toroidal angle. For equilibrium an additional vertical field is necessary to prevent the plasma major radius R_0 from growing until the plasma runs into the vacuum vessel. This field is provided by the Equilibrium Field coils.

The plasma current creates a poloidal magnetic field, which stablizes the plasma so long as it is not large enough to excite current-driven modes. The plasma current is driven inductively by a changing current in the Ohmic Transformer Stack inserted in the axis of the torus. **Tokamaks** [5] by Wesson provides a longitudinal survey of all of tokamak physics, liberally illustrated and with lengthy bibliography. Table 1.1 lists some recently operating tokamaks (data from [5]).

1.4 Inductive Heating

In addition to helping to stablize the plasma, the inductively driven current also heats the plasma due to resistive losses in the plasma. This inductive heating term is

$$P_{ind} = 2\pi R \int_A dA \;\; \eta J^2 \;, \tag{1.21}$$

[2]This figure courtesy Dr. Darren Garnier

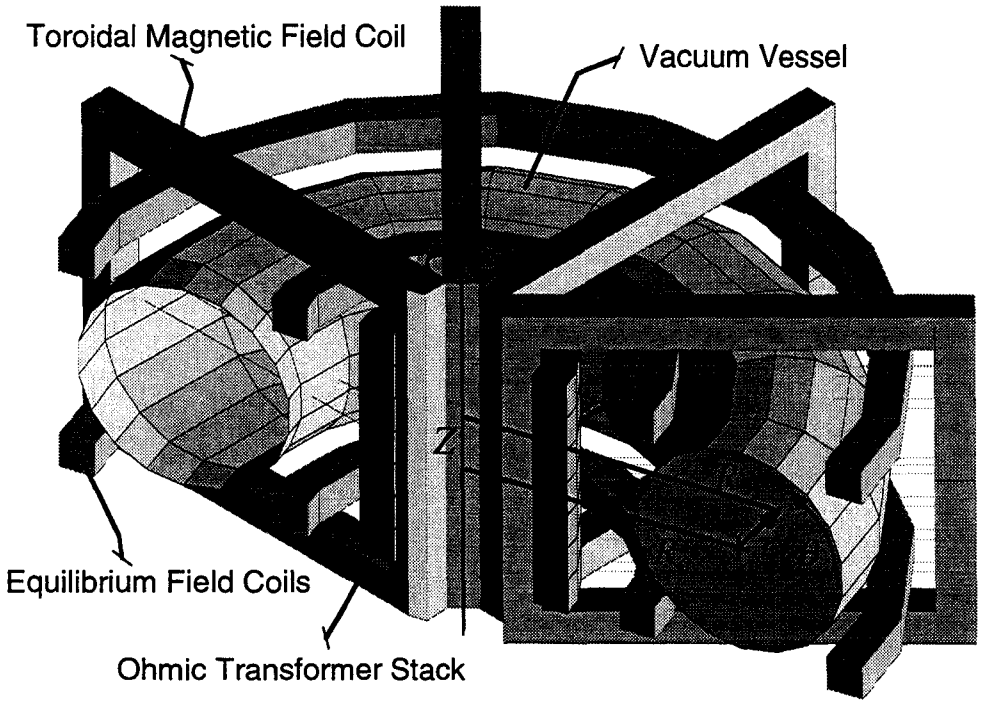

Figure 1.2: Diagram of Tokamak

Device Name	Year	Major Radius (m)	Minor Radius (m)	Toroidal Field (T)	Plasma Current (MA)	Location
Alcator C-Mod	1993	0.67	0.22	9.0	1.4	MIT
ASDEX-Upgrade	1991	1.65	0.5	3.9	1.4	Germany
D-IIID	1986	1.67	0.67	2.1	1.0	San Diego
FT-Upgrade	1990	0.93	0.3	8.0	1.3	Italy
JET	1983	3.0	1.25	3.5	7.0	England
JT-60U	1991	3.4	1.1	4.2	5.0	Japan
TFTR	1982	2.4	0.8	5.0	2.2	Princeton
Tore Supra	1988	2.37	0.8	4.5	2.0	France

Table 1.1: Recently Operating Tokamaks

where η is the resistivity, R is the major radius of the plasma, and dA the differential poloidal cross-section.

Plasmas conduct electricity well, but show one important difference from metallic conductors. The resistivity of a metallic conductor increases with increasing temerature. A pure metal with no geometric imperfections to mar its perfect crystalline lattice would, at T = 0 K, be a perfect conductor. At finite temperatures an electron moving through the conductor will scatter from thermally-induced imperfections in the lattice. A typical atom may be characterized by a vibration amplitude x, describing its displacement from the zero-temperature position. The atom then presents a scattering target with an area $\sigma \propto x^2$. To lowest order the electrostatic potential which binds the atom has the from of a simple harmonic oscillator, so that $x^2 \propto K.E.$, where K.E. is the kinetic energy of the atom. Averaged over time $< K.E. > \propto kT$, where T is the absolute temperature. Thus, in a pure metal, $\eta \propto T$.

On the other hand, the resistivity in a plasma is governed by the cross-section of scattering for charged particles from charged particles—Rutherford scattering. The current carriers are still electrons, but the scattering cross section is now $\sigma \propto v^{-4}$, where v is the thermal velocity of the electrons. The resistivity of a plasma is dominated by electron-ion collisions. The collision frequency $\nu_{ei} = n\sigma v \propto v^{-3}$ implies a

resistivity first calculated by Spitzer:

$$\eta \approx \frac{\pi e^2 m^{1/2}}{(4\pi\epsilon_0)^2 (kT_e)^{3/2}} \ln \Lambda \ , \tag{1.22}$$

in MKS units, where m is the electron mass and $\Lambda = 12\pi n \lambda_d^3$, so that $\ln \Lambda$ is typically of order 10. A 100 eV Hydrogen plasma has resistivity $\eta = 5 \times 10^{-7}\ \Omega m$, similar to stainless steel. A 1 KeV Hydrogen plasma has resistivity $\eta = 2 \times 10^{-8}\ \Omega m$, equal to Copper. The resistivity of the plasma decreases with increasing temperature, setting an upper limit to the maximum temperature that can be attained by forcing a current through it, once energy losses have been taken into account.

1.5 RF Heating

The temperatures that can be attained through inductive heating alone are not high enough to achieve significant amounts of fusion in existing tokamaks. Two alternative heating strategies have beeen pursued, the first involving injection of monoenergetic beams of atoms (neutral beam heating), and the second using radio frequency (RF) waves launched from antennas or waveguides outside the plasma. Neutral beam heating has been used in the highest-yield fusion plasmas attained to date, but is not available on C-Mod and is not considered in this dissertation.

RF heating works by transferring wave energy to particle energy, for example through Landau or cyclotron damping of the wave. In Landau damping the phase velocity of the wave is similar to the parallel thermal velocity of one of the plasma species

$$\frac{\omega}{k_\parallel} = v_{tj}, \tag{1.23}$$

so that as long as there are slightly more particles moving a little slower than the wave than moving a little faster than the wave, energy is transferred from the wave to the motion of particles along the magnetic field lines. For cyclotron damping to occur, the wave must possess an electric field component which is polarized with respect to

the magnetic field lines in the same sense as the particle gyration (left-hand circularly polarized for the ions, right-hand circularly polarized for the electrons). The wave frequency must also match the particle gyrofrequency. In this case the particles acquire perpendicular energy.

For any given finite-temperature plasma there are three different propagating waves which are candidates for RF heating. Selection of which wave to use are governed by heating efficiency and wave accessibility. Since tokamak plasmas are inhomogenous, a particular wave is likely to be damped only in a small spatial region. By suitable choice of wave frequency, this region can be set to occur near the center of the plasma, where heating is desired. Then the energy transferred to the particles in the absorption region can be calculated (see [4] for the method of calculation), and the heating efficiency computed as P_{abs}/P_w, the ratio of the absorbed power to the power in the wave. However, it may be difficult to couple energy from the antenna near-fields to the propagating plasma wave. There may be regions where the wave does not propagate in between the antenna and the absorption region, or there may not be room to install the antenna (particularly on the smaller-major-radius side of the tokamak).

1.6 Alcator C-Mod Overview

Alcator C-Mod, being the third in a series of tokamaks named Alcator, was proposed in 1985 [6]. Alcator A had been a proof of the principle that decent plasma confinement could be achieved in a small, high-field tokamak, while Alcator C held the world record for $n\tau_E$ of 8×10^{19} m^{-3}s from 1983 to 1986 [7]. There was no Alcator B. Alcator C-Mod differs from Alcator C in offering improved control of magnetic field geometry, in having a divertor, in having more auxilliary RF heating power, and in having a greatly enhanced plasma diagnostic capability.

On C-Mod, the antenna is installed on the larger-major-radius side of the tokamak and couples power to the fast magnetosonic wave, as will be discussed in detail in Chapter 5. There is a narrow region in between the antenna and the plasma edge

where the wave does not propagate, but the thickness of this region is small compared to a wavelength, and the wave fields efficiently "tunnel through" it to the main plasma. The wave then propagates to the center and is absorbed there by by cyclotron damping. More than 90 % of the power leaving the antenna has been observed to heat the plasma center (see Figure 5.7).

1.7 RF Edge Physics on Alcator C-Mod

Outside of the plasma edge, the plasma density and temperature rapidly decrease. Ideal MHD does not apply in this region, called the Scrape-Off Layer (SOL). Large RF electric and magnetic fields exist in the vicinity of the RF antenna. How do these fields modify the SOL? Does the modification to the SOL itself affect the width of the region where the RF wave does not propagate? Can the absorption in the center of the plasma be understood from measurements made in the SOL? These questions are the subject of investigation in this thesis. The plan of this thesis is as follows:

Chapter 2 describes the Alcator C-mod tokamak.

Chapter 3 describes the experimental tools built for this thesis research .

Chapter 4 shows measurements of plasma edge conditions, and how they affect the launching of RF power.

Chapter 5 shows measurements of RF power that has crossed the plasma, and presents an experimental measurement which confirms a simple analytic theory and a complex computer code.

Chapter 6 investigates a mechanism by which the RF power is known to be absorbed in the edge of the plasma before reaching the center.

Chapter 7 summarizes all results.

Chapter 2

The Alcator C-Mod Tokamak

This chapter will introduce Alcator C-Mod to the experimental physicist who may not be acquainted with the particulars of this project, but is familiar with other projects of a similar scale. C-Mod operates under an annual budget of $14 million dollars and employs about 20 scientists, with a similar number of students and as many technical support staff. It is a center of collaboration with scientists from other universities and laboratories, in particular Princeton, the University of Texas, and the University of Maryland. It is overseen by the Office of Energy Research within the US Department of Energy. The largest subsystem of C-Mod is the magnets and magnet power supplies, which allow flexibiity in the creation of magnetic field geometries, specifically the creation of a diverted plasma, which is then heated by up to 4 MW of RF power (with 4 MW more power soon to be available).

2.1 Magnets

Figure 2.1 shows a cross section of C-Mod in which each of the three magnet sets may be seen. None of them lie within the vacuum vessel. The large toroidal magnetic field is created by the TF magnets, of which there are twenty, spaced 18° apart in the toroidal direction. These are made of copper, and cooled with liquid nitrogen in order to reduce the resistivity and to withstand greater stress. The designed current limit is 250 kA, corresponding to 9 T magnetic field at the center of the plasma. Toroidal

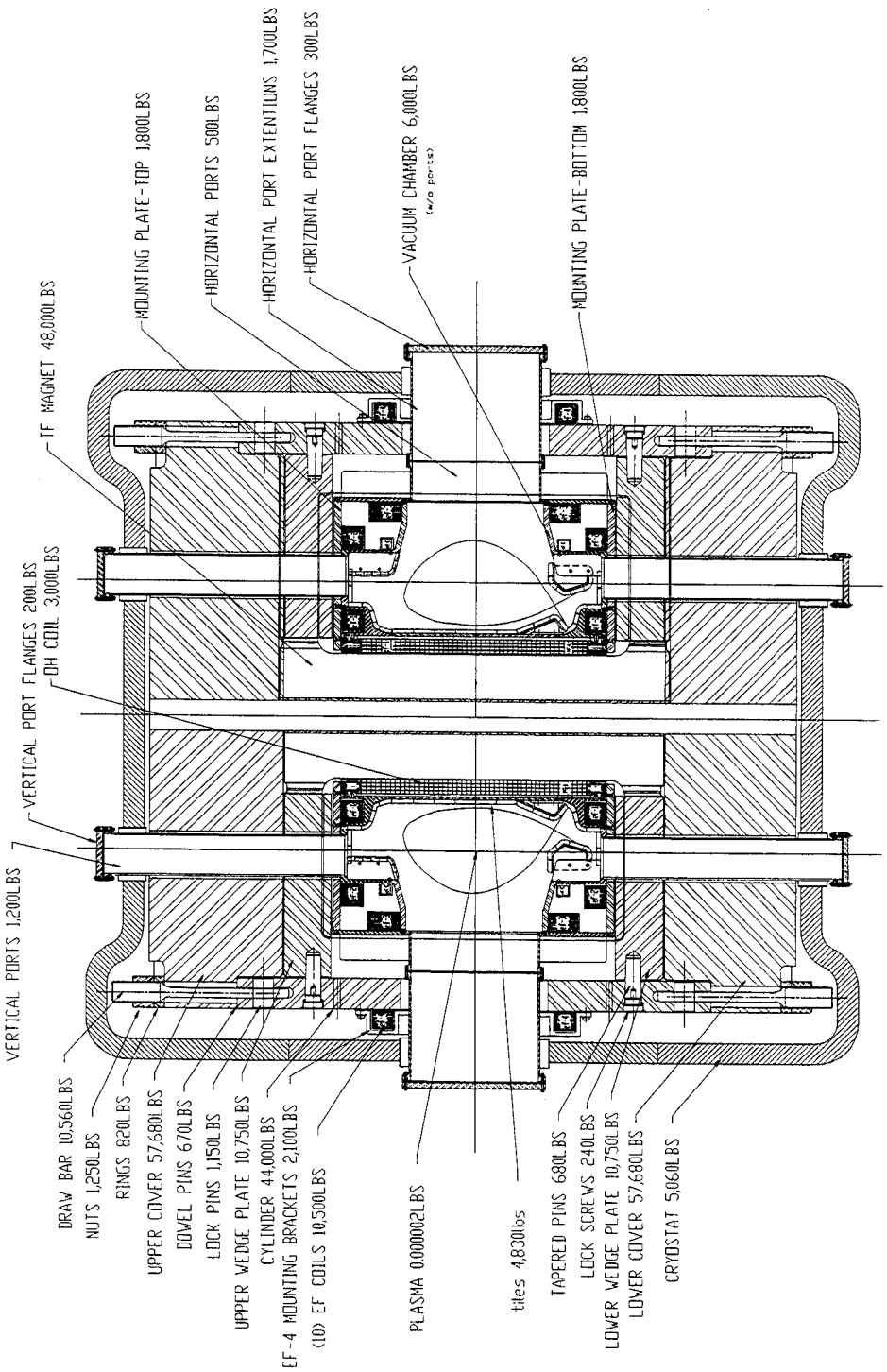

Figure 2.1: Cross-section of the Alcator C-Mod tokamak.

field ripple (correction to axisymmetry due to the discrete nature of the TF magnets) has been calculated to be less than 0.5% within the plasma [8]. With the exception of the toroidal field ripple the magnetic geometry is axisymmetric.

The plasma current is driven by the ohmic transformer, which consists of the three OH magnets, OH1 and OH2 upper and lower. These magnets serve as the primary coil of the transformer, and induce a loop voltage in the plasma (the secondary) of typically about 1 V. The magnet power supplies are summarized in Table 2.1. The remaining external field (EF) magnets are responsible for shaping the plasma (with

Supply Name	Bipolar Current	Full-Load Voltage		Maximum Current	Flat-Top	Comments
		Rectify	Invert			
TF	No	900	700	260 kA	1 sec	Robicon Auto-tap
OH1	Yes	500	375	±50 kA	1 sec	Robicon
OH2U	Yes	100	75	±50 kA	1 sec	Robicon
OH2L	Yes	100	75	±50 kA	1 sec	Robicon
EF1U	Yes	300	200	±15 kA	2 sec	Robicon
EF1L	Yes	300	200	±15 kA	2 sec	Robicon
EF2U	No	550	400	8 kA	1 sec	4 TMX
EF2L	No	550	400	8 kA	1 sec	4 TMX
EF3	No	2400	1800	22 kA	1 sec	Brown Bovari
EF4	Yes	1000	850	±15 kA	2 sec	Robicon
EFC	No	700	600	3 kA	3 sec	3 TMX, chopper

Table 2.1: Summary of Alcator Magnet Power Supplies

some help from OH2), as, for example, in the creation of an x-point (see Section 2.1.1) during diverted operation, and in restraining the growth of instabilities on the ms time scale. In the last effort, the current in the EF magnets is controlled by a hybrid controller. This object uses a digitally programmed matrix to program analog hardware to calculate the magnet currents given the input flux loop signals, which signify the plasma position (more precisely, the position of the current carried by the plasma). If this is seen to change from the nominal equilibrium position the appropriate magnet is energized to push the plasma back towards the desired equilibrium. The feedback time is limited by the power supply response time, not

computational speed.

The magnets require approximately 80 MJ in total to sustain the plasma for one second. This peak power demand of 80 MW necessitates pulsed operation. The ultimate source of the magnet power is a Cambridge Electric 13,800 V line running underneath the fusion center. This power is used to spin up a heavy alternator. The magnet power is generated by the rapid deceleration of the spinning alternator. It takes about 15 minutes to spin the alternator back up to speed, which limits the duty cycle of C-Mod to a one-second plasma *shot* in approximately 15 minutes.

2.1.1 Divertor

The large number of independently controllable coils allows the creation of an axisymmetric field null, or *x-point*, at which the poloidal field (including the field produced by the plasma current) goes to zero. The magnetic field is diagnosed by an array of flux loops and B_{pol} coils (which measure the poloidal magnetic field), and the total plasma current is measured by a Rogowski Coil (see [9] for descriptions of these diagnostics). All coils are inside the vessel. The computer program EFIT [10] takes the signals from these diagnostics and calculates the 2D plasma equilibrium by solving the Grad-Shafranov equation (toroidal symmetry is assumed). A typical C-Mod equilibrium field calculated by EFIT is shown in Figure 2.2.

The magnetic field lines which lead to the x-point define the edge of the plasma, or *separatrix*, for those which are inside the separatrix wind around the torus forever while those which are outside the separatrix terminate in a material surface. Particles which are lost from the main plasma due to collisions find themselves on the separatrix, and follow a specific magnetic field line through the x-point and into the cold, dense plasma contained in the *divertor*, which appears in Figure 2.2 as the region immediately below the x-point. The first tokamak to use a divertor was apparently T-12, at the Kurchatov Institute in Moscow, in 1972 [5].

On C-Mod the divertor plasma temperature is typically 5 eV. The divertor plates are mostly nearly tangent to the field lines, to spread the heat load over the largest possible surface area and to minimize the recycling of sputtered impurites back into

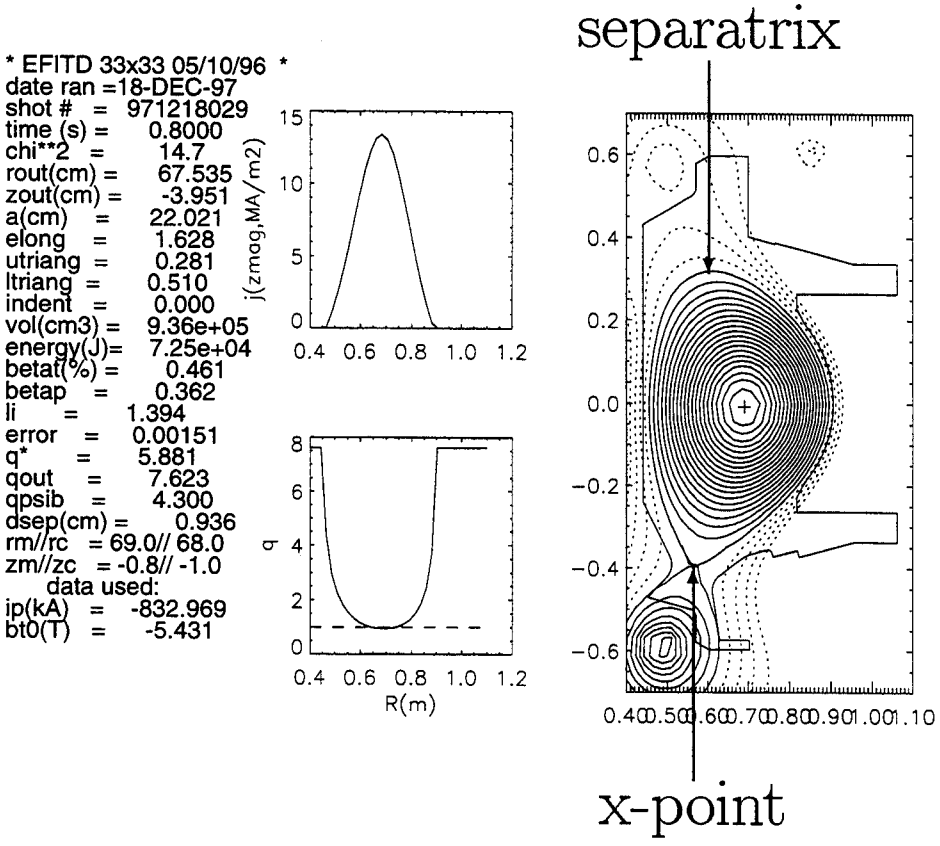

Figure 2.2: EFIT Reconstruction of Magnetic Flux Surfaces

the main plasma. There is a substantial population of neutral atoms in the divertor thanks to recombination of ions and electrons; the *compression ratio* of neutral pressure in the divertor to neutral pressure in the edge of the main plasma chamber can be as large as several hundred. High neutral pressure in the divertor is desirable so that collisions between unconfined plasma particles and neutrals will cause some of the kinetic energy of the unconfined plasma particles to be radiated away before the particles reach the divertor plates.

2.2 C-Mod RF System

In C-Mod the auxillary RF heating power exceeds the ohmic heating power from the OH magnets by up to a factor of 5. Up to 3.5 MW of RF power has been coupled to the plasma by the two C-Mod two-strap antennas [11], which are shown in Figure 2.3. There are two antennas, each with two current straps. Each antenna is protected

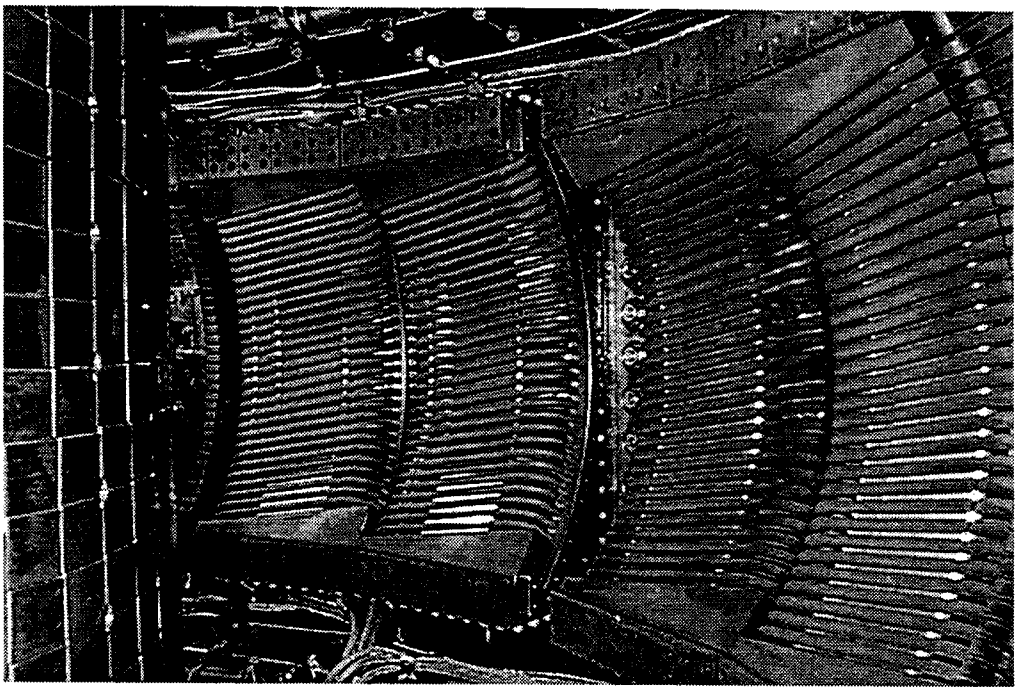

Figure 2.3: Alcator C-Mod Two-strap Antennas

from direct contact with the plasma by a *Faraday shield*, visible as a poloidal array of slanted rods. The angle of the rods matches the angle of the magnetic field lines at the plasma edge for typical values of the toroidal field and toroidal plasma current (which generates a poloidal field). The Faraday shield not only protects the antenna from damage due to contact with the plasma, but also prevents any electrostatic wave fields[1] generated by the antenna from leaking out into the plasma.

Behind the Faraday shields may be seen the four current straps which run in the poloidal direction. The oscillating poloidal current produces an oscillating toroidal magnetic field. Each current strap is grounded at the midplane (the horizontal center of the picture) and fed at the top and bottom, π out of phase, producing a current which peaks on the midplane and has the narrowest possible poloidal mode spectrum. Adjacent straps are driven π out of phase. The resultant toroidal mode spectrum peaks at $N_\phi = 10$ (there are two current straps per access port, and 10 access ports spaced evenly around the toroidal direction, though only two access ports

[1] An "Electrostatic wave" is not an oxymoron, but rather a wave which carries most of its energy in an oscillating electrostatic potential $\tilde{\phi}$. Its correlate is "electromagnetic wave".

have antennas in them). The oscillating poloidal current in the current straps produces an electromagnetic wave in the plasma that has an oscillating magnetic field in the toroidal direction.

Cold-plasma wave theory predicts a the existence of a low-frequency wave, with $\tilde{\mathbf{B}}$ parallel to the unperturbed field $\mathbf{B_0}$, that propagates perpendicular to $\mathbf{B_0}$. This is called the magnetosonic wave. It is a branch of the Alfven wave, and to lowest order obeys the dispersion relation: $\omega = k_\perp v_A$, where v_A is the Alfven velocity $v_A = B/\sqrt{\mu_0 n_i m_i}$. The antenna fields couple to this wave through a thin layer where it is evanescent. The magnetosonic wave then propagates to the plasma core and its power is abosorbed. A detailed guide to fast-wave heating is provided by [12].

The frequency of the RF for the data shown in this thesis was 80 MHz. The RF power is provided by two FMIT transmitters, each with 2 MW capacity and an output impedance of 50 Ω. Matching to the plasma was accomplished by a series phase-shifter and stub-tuner. The loading resistance R_L, which is the real part of the impedance presented by the plasma to the antennas, is 4 $\Omega < R_L <$ 20 Ω. When R_L gets too small, the voltage between the inner and outer conductors exceeds a preset limit of about 40 kV, and the transmitter is shut off to prevent a high-voltage arc in the transmission line. R_L does not exceed 20 Ω in normal operation.

2.3 C-Mod Core Diagnostics

The diagnostics that measure plasma parameters of the core of the C-Mod plasma are listed in Table 2.2. New diagnostics (and new diagnosticians) are slowly being added as the program budget permits. The theory and operation of plasma diagnostics are described in **Principles of Plasma Diagnostics** [9] by Hutchinson. Two of these diagnostics (besides EFIT) are located outside the vacuum vessel: the directional couplers are installed in the RF transmission line, and the fission detectors sit in large cans next to and under the tokamak.

parameter	diagnostic	description
n_e	Two-Color Interferometer (TCI)[13]	Measures line-integrated refractive index, and thus line-integrated electron density. There are 9 vertical chords. Local density obtained by Abel inversion. Time resolution 0.1 ms
T_e	Michelson Interferometer[14], Grating Polychromator[15]	Michelson: T_e profile, absolutely calibrated, time resolutuion ~10ms GPC: T_e at 9 major radii; time resolution ≥ 6 μs
I_p	Rogowski Coil[16]	Measures change in toroidal current giving I_p after one integration. Time resolution 0.1 ms
B	Flux loops[16]	27 of which located around the vacuum vessel allow calculation of the fields caused by the plasma. 0.1 ms time resolution
P_{RF}	Directional couplers	Provide separate measurements of RF power travelling towards and away from the RF antenna; power coupled to the plasma is the difference. 0.1 ms time resolution
T_D	Fission detectors	Measures global neutron flux and thus implies core T_D
v_{tor}	X-ray Spectrometer	Impurity rotation via Doppler broadening of impurity line radiation
impurities	Moly. Monitor [17]	Molybdenum line radiation; can be cross calibrated with MacPherson Spectrometer (see Table 2.3 to give Moly. density
q	EFIT [10]	2D code which reconstructs magnetic flux geometry from magnetics signals. Time resolution generally 20 ms.

Table 2.2: Alcator C-Mod Core Diagnostics

parameter	diagnostic	description
Total radiation	2π Bolometer	Integrates over main plasma and divertor
Line radiation: Tunable Deuterium line	MacPherson spectrometer[18] D_α diode array	Can distinguish H and D lines and give [H]/[D] estimate many diodes and views
n_e	Reflectometer[19]	Transit time of microwaves reflected from plasma gives location of density surface
$f_i(E_i)$	Charge Exchange (CX)[20]	Bins neutrals according to energy, used primarily as an edge diagnostic on Alcator
n_e, T_e, V_f	Langmuir Probes	48 in divertor [21], 4 on fast-scanning probe [22].

Table 2.3: Alcator C-mod Edge Diagnostics

2.4 C-Mod Edge Diagnostics

Plasma parameters measured in the plasma edge are likely to show significant variation with toroidal and poloidal position, due to the nonsymmetric shape of the first material surface. Some plasma edge diagnostics, such as the 2π bolometer, provide averages over large toroidal or poloidal extent, while others, such as Langmuir probes, give very localized measurements. Data from edge diagnostics may be influenced or dominated by plasma-surface interactions, so it can be difficult to separate the plasma physics from device-dependent phenomena, and it is not possible to cross-calibrate all edge diagnostics. The best of the edge diagnostics are shown in Table 2.3. The Langmuir probes in the last line of the table are different from the Langmuir probes described in this thesis. In measuring the densities and temperatures of the divertor plasma, the divertor probes directly measure the heat flux to the divertor plates, and provide indirect information about the conditions in the edge of the main plasma, "upstream" along a field line. The upstream conditions are directly measured by the fast-scanning probe, which can penetrate a few millimeters inside the separatrix without ill effect.

2.5 Important C-Mod Phenomena

Of the plasma phenomena that have been seen on so many tokamaks, and have such distinctive signatures in data from multiple diagnostics, that they have been awarded names, three are of particular importance to C-Mod, and to this thesis: sawteeth [23], H-mode [24], and Edge-Localized Modes (ELMs) [25].

Sawteeth are named for the shape of the time history of the central electron temperature. They were first noted in 1974 on the Princeton Large Torus (PLT), built at Princeton University, on the soft X-ray emission diagnostic [23]. See Figure 2.4 for an illustration of sawteeth, as detected by the Grating Polychromator (GPC) measurement of the electron temperature on C-Mod. The GPC diagnoses the 2^{nd}

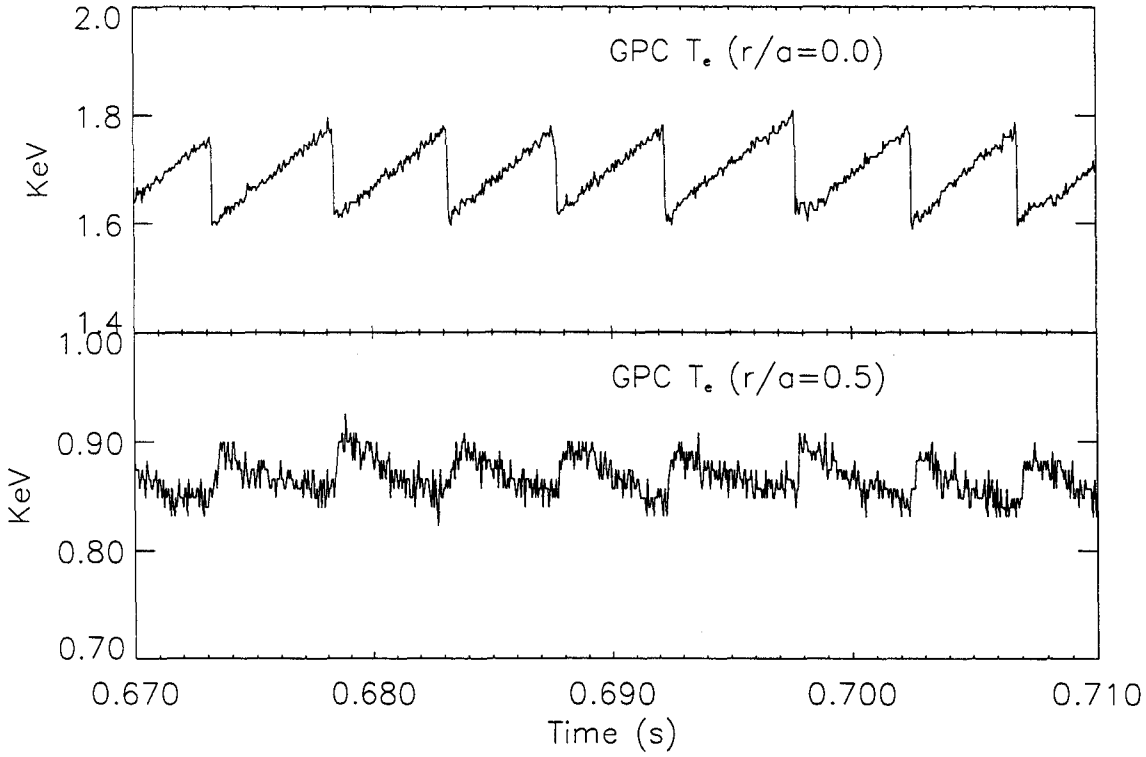

Figure 2.4: Sawtooth Instability on C-Mod

harmonic electron cyclotron emission, which on C-Mod has frequency 150 GHz < f < 600 GHz [26]. A diffraction grating is used to distribute the radiation as a function of frequency across nine microwave detectors, each of which is then measuring radiation from a different major radius of the tokamak due to the $1/R$ dependence of magnetic field. T_e can then be deduced from the intensity of radiation.

Both Ohmic and RF heating preferentially heat the center, so the central temperature rises faster than the temperature just outside the center. When the central temperature gets high enough, some kind of MHD instability develops, and a magnetic reconnection event occurs which mixes the hot particles from the center with the cooler particles from just outside the core. The central temperature then crashes (a "sawtooth crash") and a heat pulse, in the form of a more or less sudden increase in T_e, is seen to propagate outward from the core. Eight sawtooth crashes may be seen in the central T_e in the first trace in Figure 2.4, which produce the eight blunted heat pulses in the second trace, T_e halfway to the plasma edge. The *inversion radius* demarcates the inner regions, where sawtoothing is seen, and the outer regions where *inverse sawtoothing* appears. The inverse sawtooth peak generally becomes less sudden and more blunted further from the core. Sawteeth affect n_e and I_p much less than they affect T_e.

H-mode was first seen on ASDEX in 1982 [24]. The "H" stands for "High", as in the phrase "High confinement", signifying an increase in both particle and energy confinement times. The energy confinement time τ_E of an RF-heated tokamak plasma is estimated as

$$\tau_E = \frac{\int^{separatrix} \sum_{j=i,e} \frac{3}{2} n_j T_j dV}{V_{loop} I_p + P_{RF}}, \tag{2.1}$$

where the numerator is the particle stored energy (the integral is taken inside the separatrix) and the denominator is the input power[2]. When the plasma goes into H-mode, the energy confinement time suddenly increases, sometimes more than doubling. On C-mod, it has been found that, after the walls of the vacuum vessel are coated with Boron, H-mode can be repeatably achieved by the application of approximately 1 MW of RF power, as seen in Figure 2.5. The outstanding signs of a transition into H-mode are an increase of the slope of the central density, and a sudden decrease of the visible line radiation emitted by neutral deuterium (the D_α

[2]In tokamaks with neutral beam heating, an additional term P_{NBI} would appear in the denominator.

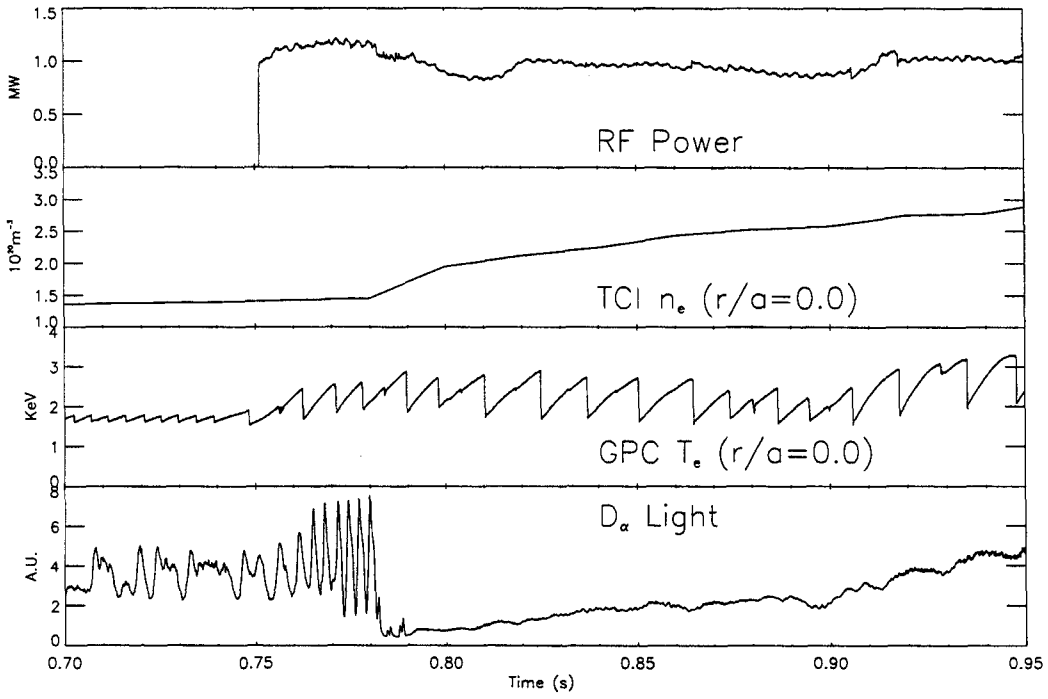

Figure 2.5: RF-induced H-mode

light). The density increases because the particle confinement time is increasing; the D_α light presumably dims because so little energy is leaking out of the plasma that the neutral atoms immediately outside the separatrix are no longer being ionized. The RF stablizes the sawteeth so that the sawtooth period increases, and the temperature increases slightly. H-mode is caused by the appeareance, near the plasma edge, of a barrier to particle and energy transport outwards, which may be identified by steep gradients in T_e and X-ray emissivity (data from C-Mod are presented in [27]). This barrier is itself generally thought to be caused by the growth of a layer of large magnetic shear, related to a large $\mathbf{E} \times \mathbf{B}$ flow shear just inside the edge of plasma [28].

ELMs have beset H-modes since the discovery of H-modes ([24], although the name ELM wasn't applied until [25]). An ELM is apparently a rapidly growing MHD instability in the plasma edge which leads to the sudden loss of the outermost layer of the plasma. ELMs appear as sharp upward spikes in the D_α light and can also turn up as upward spikes in the RF antenna loading (see Figure 2.6).

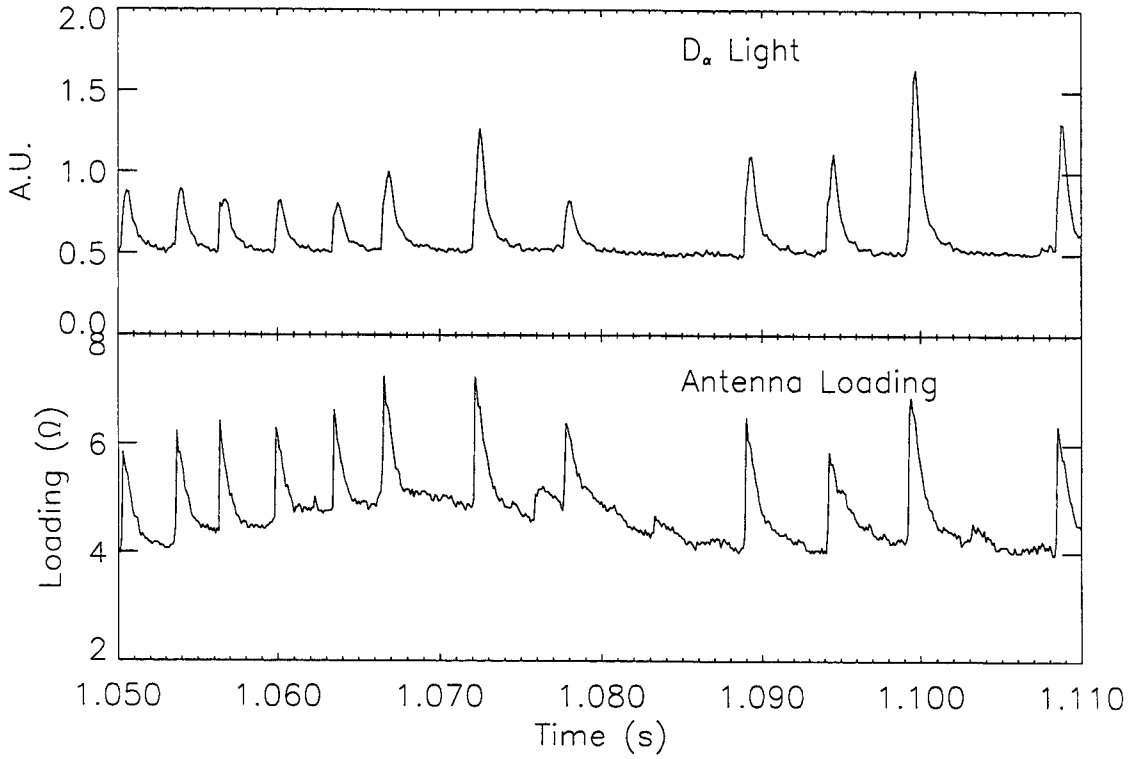

Figure 2.6: Type III ELMs on C-Mod

In general, the shorter the time between the ELMs, the less energy is lost per ELM. H-modes in C-Mod tend to be characterized either by small, high-frequency *Type III ELMs*, or no ELMs at all [29]. This is fortunate for C-Mod, for other tokamaks have observed that as the input power is raised, Type III ELMs progress to large, low-frequency *Type I ELMs*, in which significant fractions of the plasma stored energy is lost. The newly unconfined particles proceed along a field line to a material surface, which they present with a sudden power flux which challenges the integrity of even the toughest substances known to material science. Type III ELMs are far more benign, and therefore C-Mod is among the "friendliest" of the major tokamaks to new probe designs.

A fourth phenomenon that is of concern to tokamak diagnosticians is the disruption, or the sudden loss of the entire plasma due to an uncontrolled instability [30]. In effect, it is as if a lightning bolt strikes the plasma-facing surfaces. Disruptions happen regularly on C-Mod and are the leading cause of probe failures. In 99 % of C-Mod disruptions, the plasma is lost vertically, and in 80 % the plasma is lost to-

wards the x-point [31], which is below the midplane. In order the escape disruptions the ASP was installed above the midplane, away from the x-point.

Chapter 3

RF Probes on C-Mod

Much of this thesis is based on data taken by the author with RF probes on the Alcator C-Mod tokamak. "RF probe" is used here to refer to any probe with a bandwidth $f_{pr} \geq f_{RF}$, where f_{RF} is the maximum frequency of the RF heating system, which is 80 MHz. Two independent RF probe diagnostics were built specifically for this research. A fast reciprocating Langmuir probe array was built from an existing design, modified to maintain 50 Ω transmission line to within 14 cm of the probe tip. This was installed on A-port (horizontal), 3 ports away from the RF antennas, and is referred to as the A-port Scanning Probe (ASP) to distinguish it from the original scanning probe at the bottom F-port vertical port—the F-port Scanning Probe (FSP). The FSP was designed and built by Dr. Brian LaBombard. Its bandwidth is limited by the in-vacuum probe wires, which are not coaxial, to $f_{pr} \sim 1$ MHz. The FSP has reliably operated since 1993 and has been used to benchmark the ASP. Also built for this research was an array of 8 loop probes, mounted on the inner wall at midplane, behind the protection tiles, directly opposite the E-port antenna. These inner-wall loop probes measure the transmission of fast wave power from the antennas directly through the plasma. In addition, data is shown herein from Langmuir probes on the D-port ICRF antenna side protection tiles, and on the poloidal limiter in between G and H ports. These were built and installed by Dr. Yuichi Takase. There is an extensive literature of Langmuir probe theory; relevant results are summarized in Appendix A.

3.1 Locations of Probes in Tokamak

Figure 3.1 represents a horizontal cross-section of the tokamak showing the ASP and inner-wall loops. The ASP is three ports away from the nearest RF antenna, while the FSP is immediately adjacent to the E-port RF antenna.

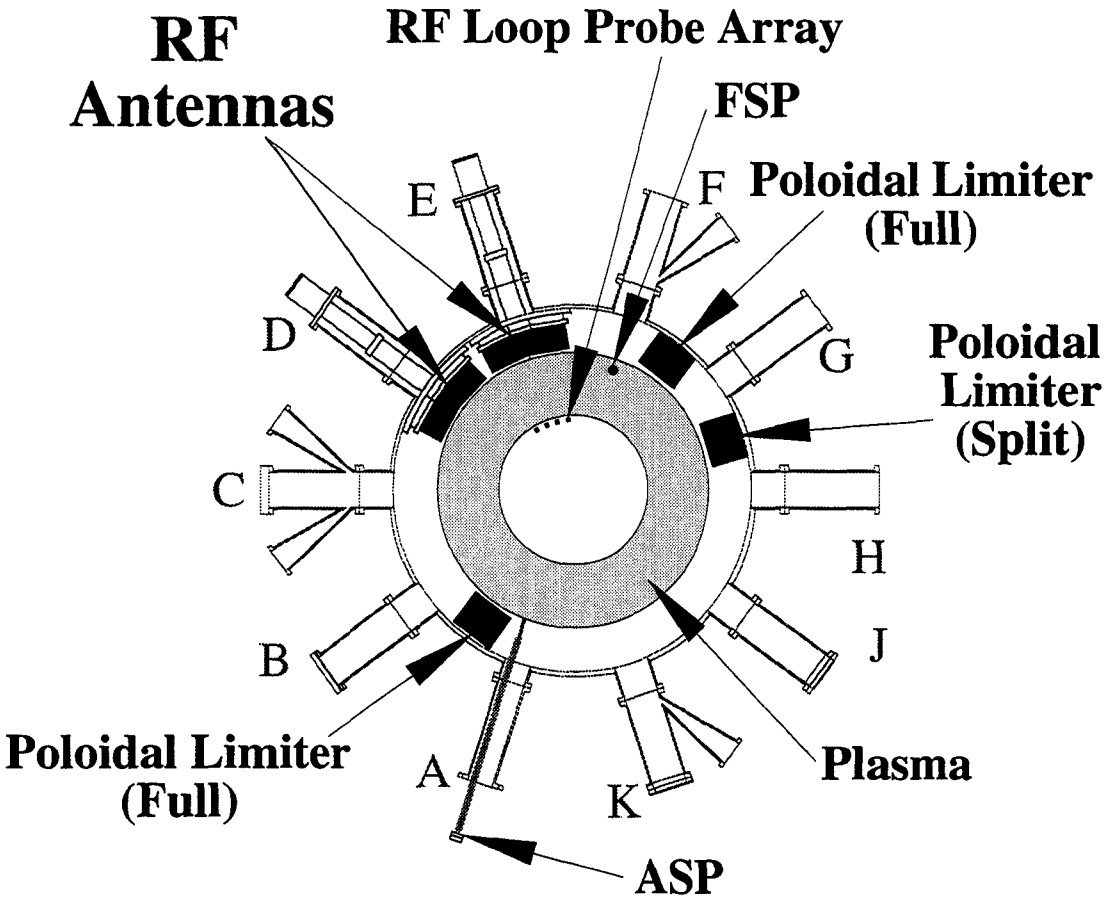

Figure 3.1: Horizontal cross-section of C-mod

A better idea of the locations of those probes on the outer wall of the tokamak can be gotten from Figure 3.2, which shows what the outer wall would look like if it were somehow unrolled and flattened. The slanting line represents the trajectory of a magnetic field line, calculated by the magnetic field reconstruction program EFIT (described in Section 2.1.1), for the cross-calibration shot which is described in the

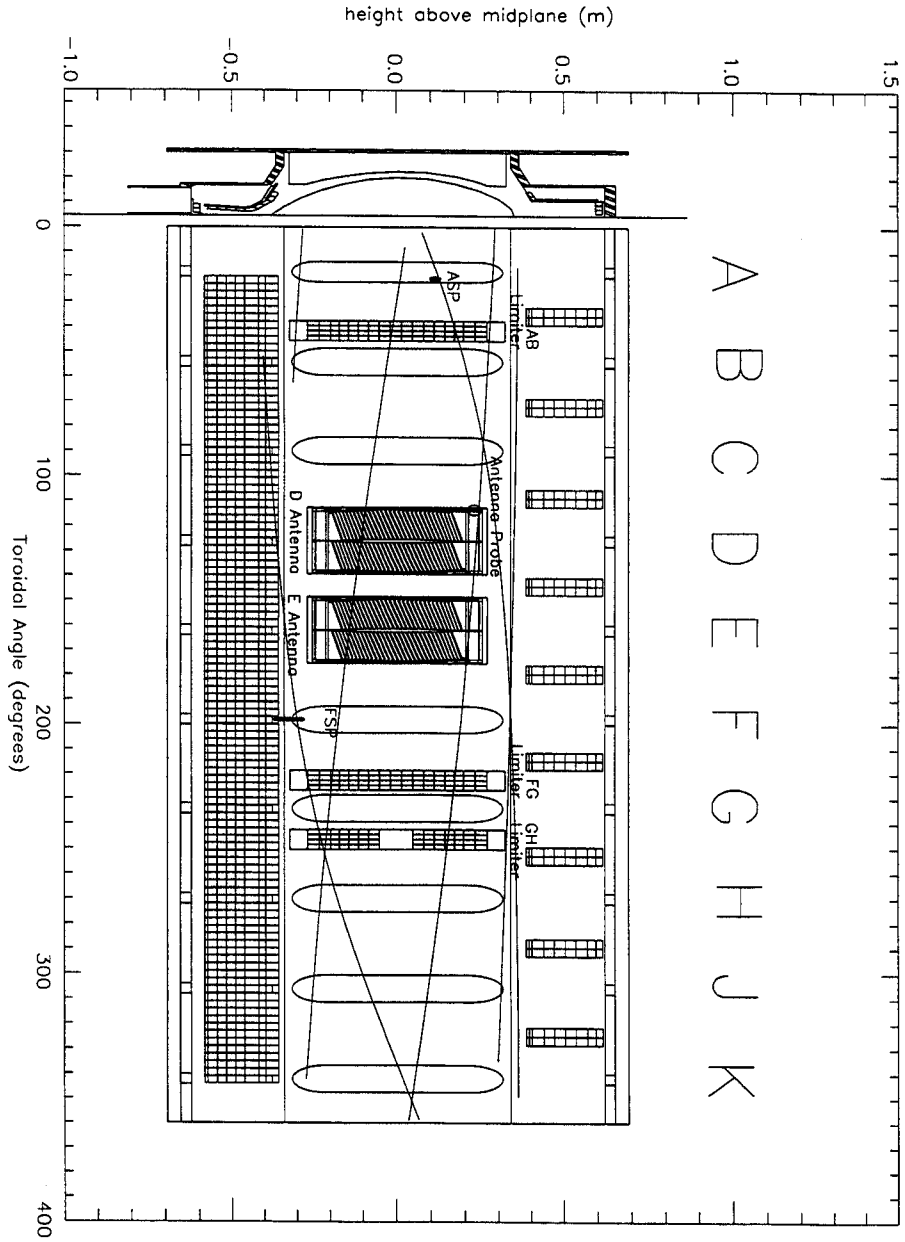

Figure 3.2: Location of Langmuir Probes

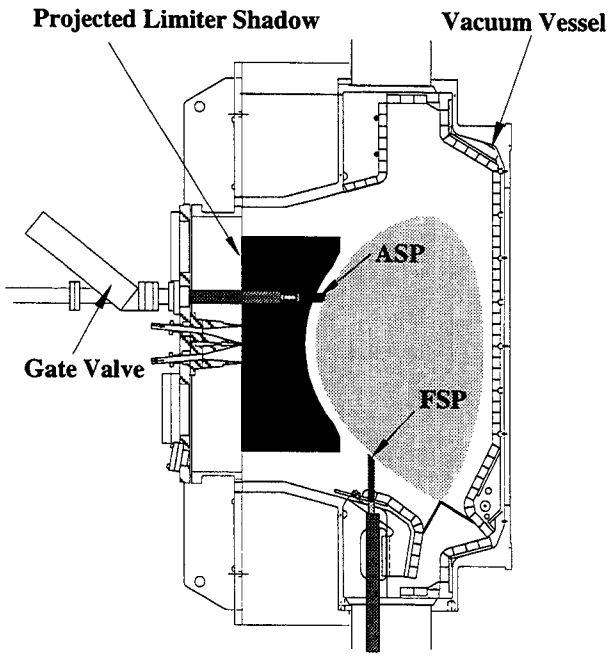

Figure 3.3: C-mod poloidal cross-section, showing ASP

next chapter. Note that the ASP and the FSP lie very nearly on the same field line for this shot (the shot parameters of $B_T = 5.7$ T, $I_p = 1$ MA are common values for C-Mod), and that this field line does not cross in front of either of the RF antennas.

A poloidal cross section of C-Mod, Figure 3.3, shows the poloidal locations of the two scanning probes, although these probes are not at the same toroidal location. Also shown is the limiter outline and the cross-section of a typical C-Mod plasma.

3.2 Construction of RF Langmuir Probes

The most intricate instrument built during the course of this work was the ASP, which consists of 4 RF Langmuir probes mounted on a pneumatically-driven probe head. Data were also taken with RF Langmuir probes mounted on a poloidal limiter, and an RF Langmuir probe mounted on the box protecting one of the RF antennas, which were built by Dr. Yuichi Takase.

3.2.1 A-port Scanning Probe

The ASP was mounted on A-Horizontal port, immediately adjacent to the AB poloidal limiter, at a height of 11.4 cm above the tokamak midplane. This location provides excellent protection from disruptions (most C-Mod disruptions are downward). The probe head was electrically isolated from all other metallic objects in the tokamak. The probe's radial position was measured relative to the inner wall to an accuracy of $\pm$ 2 mm. The ASP was typically scanned once during the plasma shot, taking 200 ms to travel 6 cm in major radius (100 ms going in, 100 ms coming out). The probe was attached to the machine via a long bellows and could be withdrawn behind a gate valve without affecting machine vacuum.

A cross section of the probe head is shown in Fig. 3.4. It was machined from upset-forged TZM molybdenum by Rembar, Inc of Dobbs Ferry, NY. Electrical isolation was achieved by means of a 0.01" coating of plasma-sprayed alumina spinel, applied to the probe head holder by Eastern Coating Systems of Framigham, MA. The 68° relief angle represents the tangent to the last closed flux surface, at the location of the probe, for a typical C-mod equilibrium. The probe tips were made to stick out past the probe head by 2.5 mm, an unusually large distance for this sort of probe, in order to minimize the perturbation to the plasma being measured caused by the probe head. Upon removal from the tokamak after collecting the data shown herein, the probe tips were found to be undamaged.

The Langmuir probe wires were made of Vacuum Metalized Tungsten (VM Tungsten), 99.95% tungsten doped with a small percentage of aluminum and other impurities, manufactured by Metallwerk Plansee GmbH, Austria, and machined to shape in-house. The VM Tungsten proved to be far more resilient than pure tungsten; no VM Tungsten probe wires broke in action. The probe wires were then coated with plasma-sprayed alumina, which in turn was coated by plasma-sprayed molybdenum (plasma-spray coatings again by ECS) to maintain coaxiality. Teflon-based coax (Storm Products P/N 421-298) with 50 Ω characteristic impedance was used to within 14 cm of the probe tip.

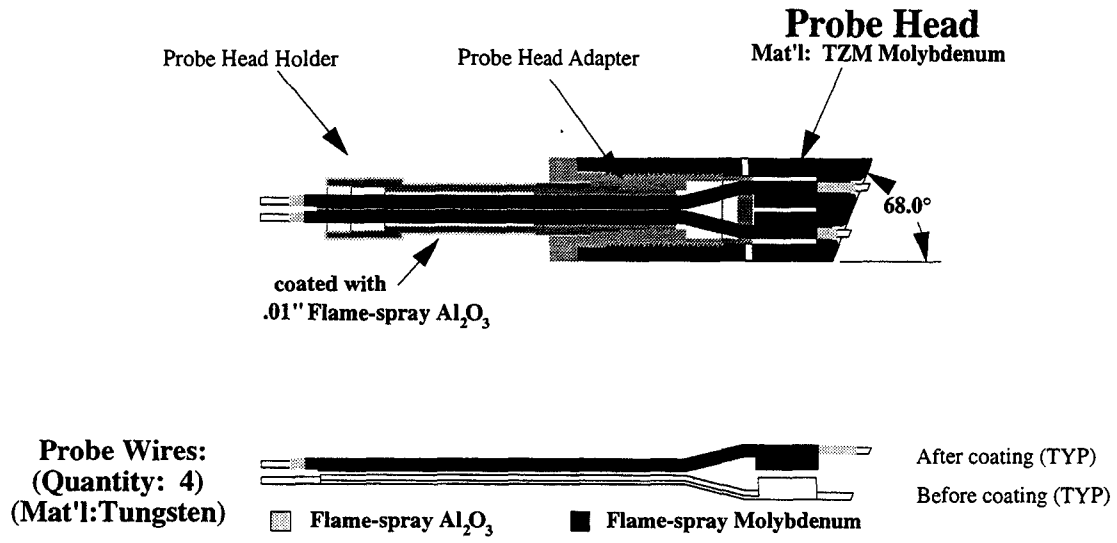

Figure 3.4: Cross-section of ASP Probe Head

3.2.2 Limiter and Antenna probes

The limiter and antenna probes were made from molybdenum and are 50 Ω to within 3 cm of the probe tip. The antenna probes were thinner and longer than the limiter probes, as may be seen in Table 3.1, in which the sizes of the three types of RF Langmuir probes, and typical plasma conditions they were exposed to, are summarized.

Probe:	ASP	Limiter	Antenna
radius (mm)	.75	1.0	.75
length (mm)	3.0	0.5	1.0
T_e (eV)	20	20	20
n_e (m^{-3})	10^{19}	10^{19}	10^{19}
M_i	$2M_H$	$2M_H$	$2M_H$
A (cm^2)	0.09	0.02	0.01
V_{Bohm} (cm/s)	1.5×10^6	1.5×10^6	1.5×10^6
I_{sat} (A)	< 0.2	< 0.05	< 0.03
R_{sh}	9 $k\Omega$	40 $k\Omega$	80 $k\Omega$

Table 3.1: RF Langmuir Probe Parameters

The RF Langmuir probes are all cylindrical, and protrude from the surfaces in which they are embedded. The Langmuir probes on the FSP are of a more complicated

shape and do not protrude (they were designed to allow measurement of Mach flows and are semi-directional).

3.3 Inner Wall Loop Probes

The second diagnostic built for this thesis research was an array of loop probes installed on the inner wall (Fig. 3.5). The array consists of four pairs of loop probes, spaced in the toroidal direction, each loop probe being sensitive to $\dot{B}_{tor}$. It is located on the inner wall at the midplane, directly opposite the E-port antenna. The pairs of loops are set ± 6.0 cm and ± 11.2 cm away from the centerline of the E-port antenna. The toroidal extent of the array is 29.25°. The array spacing was chosen to be sensitive to the spectrum of toroidal modes $1 \leq N_{tor} \leq 25$ expected to be launched by the RF antennas.

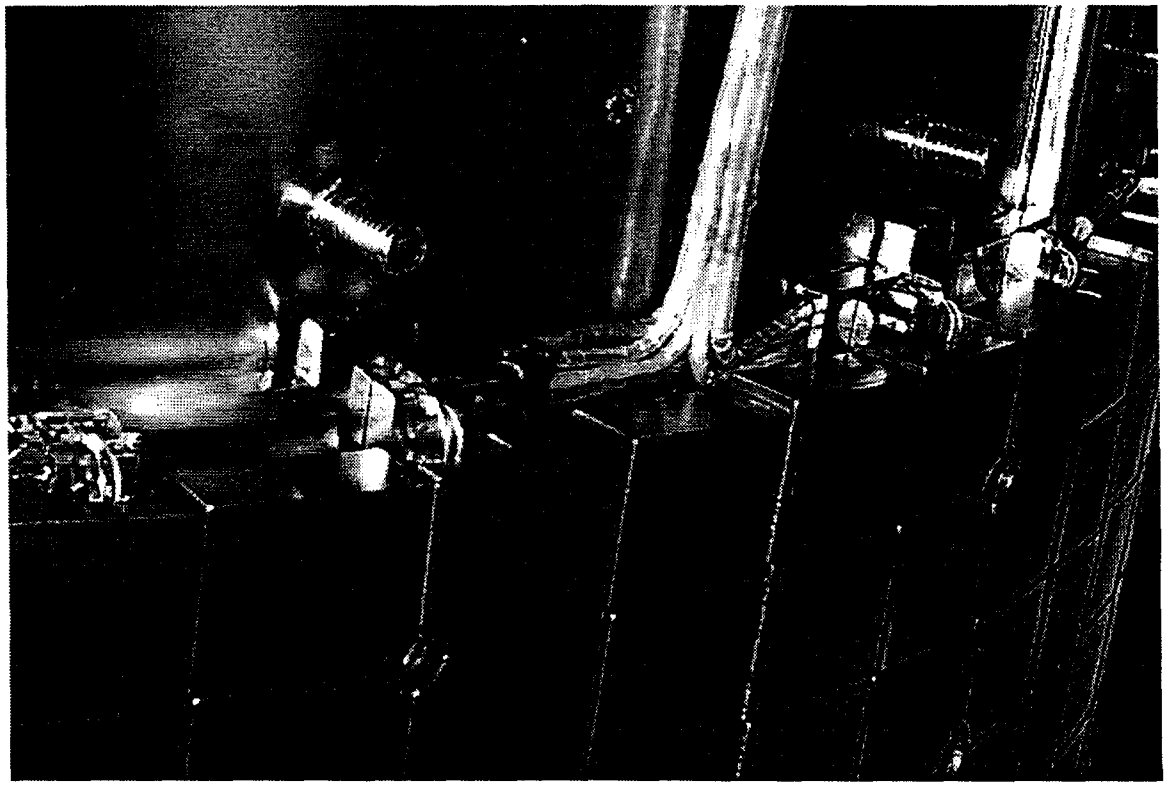

Figure 3.5: Inner wall loop probes during installation

The loop probe signals were recorded either by a fast digitizing oscilloscope (Tektronix TDS-540, 4 channels @ 250 Msa/s, 50000 data points), or amplitude/phase detectors designed at PPPL [32]. The fast scope can capture 0.2 msec of probe signal once per shot; the amplitude/phase detectors produce a DC output proportional to the input RF power, which was then digitized at 10kHz for the entire shot duration. The scope data was run through the complex demodulation code CDM[1] to recover the amplitude and the absolute phase of the spectral compenents at 80 MHz (corresponding to the E-port generator frequency) and 80.5 MHz (corresponding to the D-port generator frequency). The amplitude/phase detectors integrate over 500 kHz< f <100 MHz. For the 1997-1998 run campaign, four channels of fast digitization and four channels of RF detection were used.

Absolute calibration of the response of the loops to known electromagnetic fields through the slits between the tiles was estimated from a bench test. A small hole was machined in the outer conductor of a piece of 9" OD 50 Ω coaxial transmission line. The transmission line was connected to an RF source and terminated in a 50 Ω load. At 50 W forward power $I_{rms} = 1$ A flows in the center conductor. The azimuthal magnetic field just inside the inner surface of the outer conductor (at $R = a$) is

$$B_{az}(r = a) = \frac{\mu_0 I}{2\pi a}. \tag{3.1}$$

The hole was plugged with a slotted fixture with dimensions chosen to mimic the tiles and B_{az} was measured in a small cavity behind the slots. The penetration factor is estimated as the ratio of B_{az} measured in the cavity to B_{az} calculated at the inner surface of the coax. This penetration factor was found to depend sensitively on the depth of the slot, though not on the width of the slot (for greater than a threshold width). For the depth and width of the actual tile slots on C-Mod, the penetration factor was estimated to be 0.05.

Relative calibration of the signals of different loops was performed in situ during

[1] courtesy Dr. David Winslow, UT-FRC.

manned access to the vacuum vessel following the end of the 1997-1998 run campaign. The signal of each loop was measured when a small loop antenna ($A_{loop} \sim 2$ cm^2) was brought up to the tile gap in front of it. The powers measured by the different loops varied by a more than a factor of two, being roughly proportional to the width of the slit in front of the loop (minimum slit width, 0.010"; maximum slit width, 0.050"). The average penetration factor (estimated from a calculation of the field created by the small loop antenna) turned out to be 0.05, in agreement with the bench test.

Suppression of electrostatic pickup is accomplished in two ways. First, the molybdenum tiles behind which the probes are located act as Faraday shields, the electromagnetic component penetrating the slots between the tiles while the tiles themselves block the electrostatic component. Second, the loops were constructed with anti-parallel normals (a configuration known to electric guitarists as a "humbucking" pickup). Electrostatic pickup is eliminated by taking the difference of the signals of two loops.

Following the installation of the inner-wall loops, the electrostatic component of the signals of two loops from a pair was directly measured. The RF frequency was 80 MHz and the probe signals were captured by an oscilloscope digitizing at 250 MHz. All data showed the two signals to be 180° out of phase, to within the error of the phase measurement. It was therefore concluded that the electrostatic component of the probe signal was negligible. For the remainder of the tokamak run campaign each of the 8 loops were run independently, under the assumption that there was no electrostatic pickup.

3.4 Measurement of Electrical Length

The electrical lengths of the RF Langmuir probes and the loop probes were determined with the help of a network analyzer (Hewlett-Packard, model HP8753C), which can simuluate Time-Domain Reflectometry (TDR), the measurement of the reflections of an electrical pulse incident on a one-port device (such as a probe cable). TDR not only diagnoses the electrical length of the cable but also provides information about

its integrity, and the location of any mismatches. The electrical lengths of the in-vacuum portions of the RF Langmuir probe transmission lines must be known before the stub tuner can be installed in the proper place (see Figure 3.5), while the overall electrical length of the inner-wall loop transmission lines has to be subtracted out to allow an accurate comparison the loop probe signals' phases.

3.5 Stub cancellation

Langmuir probe characteristics taken during RF heating in tokamaks are often untrustworthy, due to the presence of an unknown amount of RF sheath rectification (see Appendix A). If the RF fluctuations in the plasma are of a single, known frequency, then the simplest way to remove the sheath rectification involves the placement of a quarter-wave stub in the transmission line, an odd number of quarter-wavelengths away from the probe [33]. The stub effects two results: it acts as a band-block filter by virtue of its length, and it places an impedance maximum at the probe due to its position in the transmission line[2]. This thesis records the first attempt to use these stubs on Langmuir probes in a tokamak.

The stubs were constructed from semi-rigid cable, Storm Products Co. P/N 421-298, and SMA connectors. The HP8753C network analyzer was used to monitor the center of the filter shape as the stubs were tuned to the correct length (approximately 76 cm for 80 MHz).

It is easy to make a stub which acts as a filter, but more difficult to ensure that the sheath rectification is prevented. If the stub is in the right place, and the transmission line is ideal, then the stub will send a reflected wave back to the probe of the same amplitude as the original wave, and there will be a current node and a voltage anti-node at the probe tip. Thus the voltage at the probe will exactly track the fluctuating voltage on the other side of the sheath and no rectified current will be drawn. This

[2]The impedance values calculated in [33] appear to ignore losses in the dielectric, which results in impossibly high values ($\sim 2M\Omega$) for the impedance maximum. Taking dielectric losses into account gives a maximum impedance of $\sim 2k\Omega \gg 50\Omega$, which is still adequate for suppressing sheath rectification.

corresponds to an infinite impedance being presented to the RF fluctuation.

If the transmission line is not ideal or the stub is not in the right place, then a finite impedance will be presented to the RF fluctuation. Whether this finite impedance is large enough to prevent the rectification may be estimated from the likely values of T_e and n_e encountered at the probe. Langmuir probes near the floating potential are known to be surrounded by a non-quasineutral region called a *sheath*, of thickness $\sim 3\lambda_D$ [9]. At RF frequencies this sheath may be modeled with lump circuit elements, as shown in Figure 3.6. When $\lambda_d \ll l$ the sheath capacitance C_s is estimated as

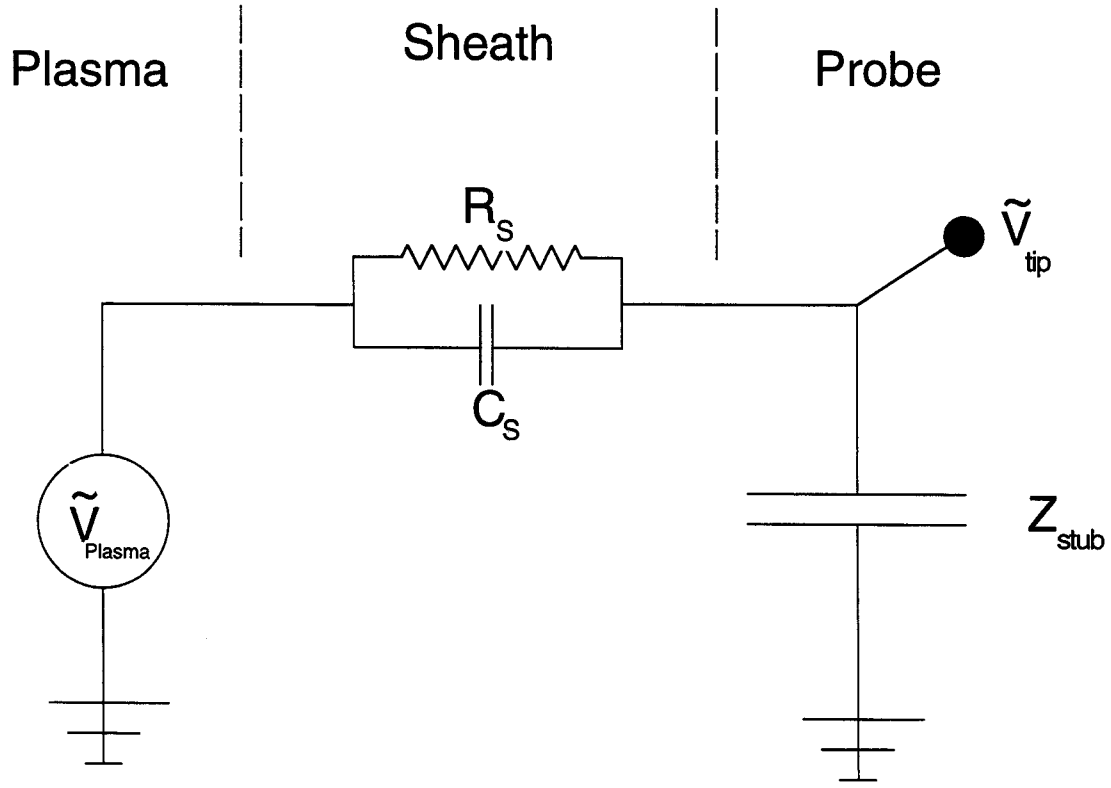

Figure 3.6: Langmuir Probe Sheath Equivalent Circuit

$$C_s = \epsilon_0 \frac{A}{3\lambda_d}, \tag{3.2}$$

where l and A are the probe thickness and area. The sheath resistance R_s is [34]

$$R_s = \left.\frac{1}{dI/dV}\right|_{V=V_f} = \frac{T_e}{eI_{sat}}, \tag{3.3}$$

where the relation of V and I, the bias voltage applied to the probe and the current drawn by the probe, is given in Appendix A, Equation A.1.

For $n_e = 2 \times 10^{19} m^{-3}$ and $T_e = 30eV$, $R_s \sim 150\ \Omega$. Taking $\omega = \omega_{RF} = 5 \times 10^8 s^{-1}$, $Z_c = 1/\omega C_s \sim 8 \times 10^4 \Omega$, and the sheath is resistive. The requirement for effective stub cancellation is then

$$Z_{stub} \gg R_s \sim 150\Omega. \tag{3.4}$$

When this is met, the RF voltage falls between the probe tip and ground, rather than between the plasma and the probe tip, so that the potential difference across the sheath is a constant during the RF cycle and no rectification occurs. The maximum achieveable value of $Z_{stub} \sim 2k\Omega$ should allow effective stub cancellation.

3.5.1 Estimation of Stub Cancellation

In TDR the measuring device sends a pulse down a transmission line and measures the reflections as a function of time [35]. A perfect transmission line will produce no reflections. From the time delays of the reflections the measuring device deduces the locations of imperfections in the transmission line, and from the sign and the time derivative of the reflected pulse, the measuring device can infer their nature (capacitive or inductive, incorrectly high or low resistance).

A TDR evaluation of one of the C-mod RF Langmuir probes is shown in Figure 3.7. Two sets of 4 lines can be seen. The quadruplication is due to 4 different methods of terminating the probe, such as shorting to ground, shorting it to the probe head, etc. The set of 4 lines which exits the plot to the right with negative values of the ordinate represent the reflected voltage, while those which exit with ordinate near zero are the derivative of the reflected voltage. The uppermost trace of both sets was

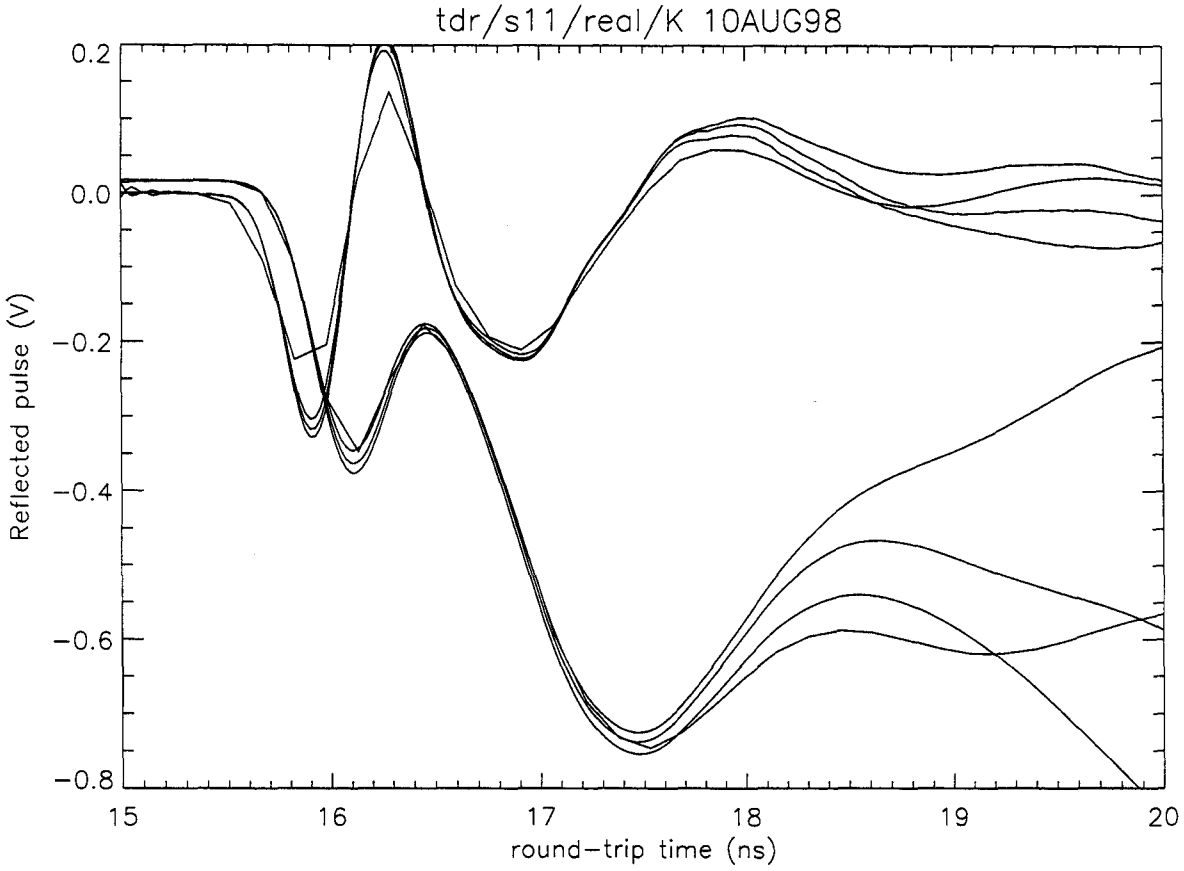

Figure 3.7: TDR of RF Langmuir Probe

taken with the probe as it was used on the tokamak. The abscissa is the round-trip time down the in-vacuum section of the transmission line.

The end of the 50 Ω section of the coax corresponds to the first minimum in the derivative of the reflected voltage. The probe wires have a characteristic impedance of about 3 Ω, which causes the derivative to tend towards −1 at a delay of 17 ns. The probe tip is located about where the set of derivatives begins to diverge, at 18.0 ns.

The measurement of the electrical delay to the probe tip allows the quarter-wave stub to be put in the correct location. The one-way electrical delay of the probe transmission line is 9.0 ns, while the nearest odd number of quarter wavelengths at 80 MHz is (conveniently) at $d_e = 3/4 \times 12.5$ ns $= 9.375$ ns, allowing the stub to be put just outside the vacuum vessel.

The capacitance of the probe wires to ground may be estimated from the char-

acteristic fall-off time of the reflected pulse at the location of the probe tip. For the probes on the ASP this fall-off time, estimated as the best fit of an exponential to the uppermost of the lowest set of 4 traces, was about 20 ns, corresponding to a capacitance of 400 pF. This was verified by using an AC LCR meter (Wayne-Kerr model 4250). This large capacitance is formed between the probe wires and the probe head, which is isolated from both the wires and from ground. It corresponds to a roll-off frequency $f_0 = (2\pi RC)^{-1} \sim 8$ MHz. This ruins the attempt to use the stubs to prevent sheath rectification. The wave which is reflected from the stub is attenuated—twice—before it returns to the probe tip, and can no longer cancel the original RF signal. Unfortunately, this determination of the probe capacitance was made after the last chance to take data using the ASP.

The antenna and limiter probes have better TDR characteristics, implying higher roll-off frequencies. Two identical limiter probes were chosen for a comparison test. A stub was installed on one probe. No difference was observed in the data. The RF levels at the probes during this test may have been too small to cause significant sheath rectification, however. The only suitable RF probe known to be dominated by sheath rectification is the antenna probe. A stub was installed on the probe on the day the TF magnet failure ended the 1997-1998 run. The probe was run only in floating mode (it was not swept). In general the RF causes a large decrement to the floating potential (discussed in Chapter 4), and this did not change when the probe was installed.

3.6 Data Acquisition

Langmuir probe characteristics analyzed in Chapter 4 were taken using electronics designed by Dr. Brian Labombard [21], which are shown in figure A.1. RF fluctuations of V_f shown in Chapter 6 were captured using several generations of HP spectrum analyzers: 2 HP8554B on loan from Princeton by kind permission of Dr. Richard Majewski, an HP8565A left over from Alcator C, and a new HP8593A. Loop probe signals shown in Chapter 5 were captured using Amplitude/Phase detectors

designed for use on TFTR [32] and a Tektronix TDS540 1GHz digitizing oscilloscope. Slow digitization transpired via Joerger TR16s2 digitizers which were generally run at 10kHz.

Data were acquired, stored and retrieved by the C-Mod data acquisition system, which is described in [36]. The data acquisition software is MDSPlus [37]. Data from the ASP and the limiter and antenna probes were collected and stored in tree structures identical to the tree structures in which FSP data were stored. Data analysis programs were written in IDL. The initial data processing program used to calculate plasma parameters from Langmuir probe sweep raw data is called RFLPANAL and was adapted by Dr. Brian LaBombard from the program LPANAL which he wrote to analyze FSP probe data. The method by which RFLPANAL fits Langmuir probe characteristics is summarized in Appendix A.

Chapter 4

RF Langmuir Probe Measurements on Alcator C-Mod

Langmuir probes measure plasma density and temperature sufficiently reliably that they are considered core diagnostics on most modern tokamaks. However, their reliability can be compromised during RF heating by the sheath rectification effect (see Appendix A). In this chapter are presented Langmuir probe measurements of n_e, T_e, and V_f taken during RF fast-wave minority heating. Sheath rectification is seen to be largest on probes closest to the antenna. The n_e and T_e measurements of the A-port Scanning Probe (ASP) (three toroidal ports away from the antennas) are found to be unaffected by sheath rectification, while data from the F-port Scanning Probe (FSP) (one toroidal port away from the antennas) shows rectification during RF L-mode but not RF H-mode. The antenna probe signal is dominated by rectification in both L-mode and H-mode. The signals from the limiter probes (between two and three toroidal ports away from the antennas) appear to show rectification during the RF turn-on transient. ASP edge profiles are used to estimate the evanescence of the fast wave at the plasma edge, and the amount of power invested in RF sheaths on field lines that connect the antenna to the limiter. The chapter begins with the comparison of the RF Langmuir Probes against other C-Mod diagnostics during Ohmic operation.

4.1 Langmuir Probe Data During Ohmic Operation

For a tokamak plasma in MHD equilibrium, the quantities n_e, T_e, and V_f are constant on a flux surface. However, on Alcator C, a limiter tokamak, a poloidal array of Langmuir probes was used to diagnose factor-of-two poloidal variations in n_e at the last closed flux surface [38], so there is reason to suspect variations on a flux surface on C-Mod. There is no corresponding poloidal probe array in C-Mod, but the placement of probes (Figure 3.2) allows comparison of data from isolated probes at the same poloidal location, and also from probes on the same field line. Comparison of the plasma parameters measured by the FSP "upstream" along a field line with those measured "downstream" by the probes in the divertor [22] is central to the current understanding of transport in the divertor (including the identification of detachment and the high-recycling regime). The possible variation of plasma parameters upstream of the FSP has hitherto not been investigated.

4.1.1 Comparison of ASP and Limiter Probe Data

The ASP at A-port has nearly the same poloidal location as two of the probes on the GH limiter, being only about 1 cm further from the midplane. Since the SOL is expected to be toroidally symmetric, comparison of data between these probes amounts to an independent check of the radial position of the ASP, which was determined by measuring its position with a ruler, relative to the tiles on the inner wall, to an accuracy of ± 2 mm.

In Figure 4.1, data taken by ASP and GH limiter probes during Ohmic operation are compared. The abscissa is the normalized flux coordinate ρ, the distance between the intersection of the magnetic field line sampled by the probe with the midplane, and the intersection of the separatrix with the midplane. This comparison was quantified by averaging the GH limiter data over 100 ms centered on the ASP scan (391 data points), and averaging all of the ASP data for which $|\rho_{ASP} - \rho_{GH}| \leq 1.5$ mm (15 data

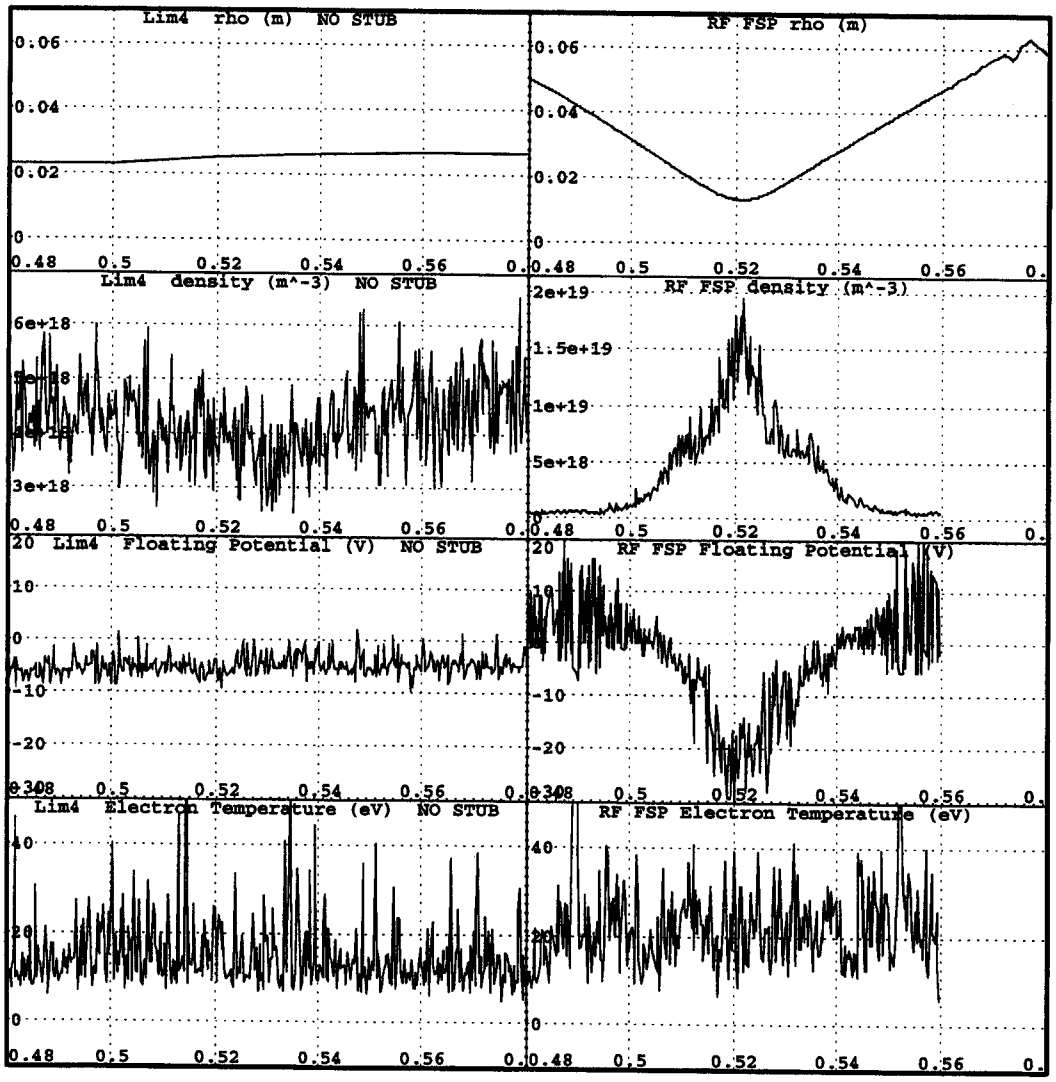

Figure 4.1: Comparison of ASP and Limiter Probe Data

points) [1]. For this shot the averaging gives:

	GH Limiter		ASP
Quantity	Average	RMS Fluctuation	Average
V_F (V)	-4.9	1.5	-2.3
n_e (/m^3)	4.2×10^{18}	5×10^{17}	4.4×10^{18}
T_e (eV)	14.5	5	21.9

Table 4.1: Limiter Probe-ASP comparison

This agreement is very good, considering the uncertainties in ρ and the fitting algorithm, and supports the assertion that the radial position of the ASP has been correctly measured. It also assuages any lingering uncertainty that the measured quantities depend on the probe size (Table 3.1).

4.1.2 Comparison of ASP and FSP Data

This subsection shows data taken during a series of 6 discharges at $B_T = 5.7$ T, $I_p = 1$ MA, on which the ASP and FSP were scanned simultaneously. The two probes come close to sharing a magnetic field line, although the FG and GH limiters are imposed between them for $\rho \geq 1.6$ cm.

Composite profiles from these six shots are shown in Figure 4.2. The RF data is the average of the two probes on the ASP which were swept, while the edge data is the average of all four FSP probes, which were all swept. The profiles of $J_{sat} \sim n_e T_e^{1/2}$ are similar. The ASP n_e is considerably lower than the FSP density in the outer portion of the scrape-off layer. The ASP T_e profile is much flatter than the FSP T_e profile and shows larger fluctuations.

The apparent spikes in the FSP T_e and V_f profiles at $\rho \sim 2.4$ cm are due to the turn-on of the RF, which occured 30 ms after the probes had reached full-in. The positive increment in T_e and the negative increment in V_f are consistent with RF-induced sheath rectification, as will be discussed in the next section. No similar spike is seen in the ASP data.

The density data suggest that the CMOD scrape-off layer can be divided into

[1] The length of the probes on the ASP is 3 mm.

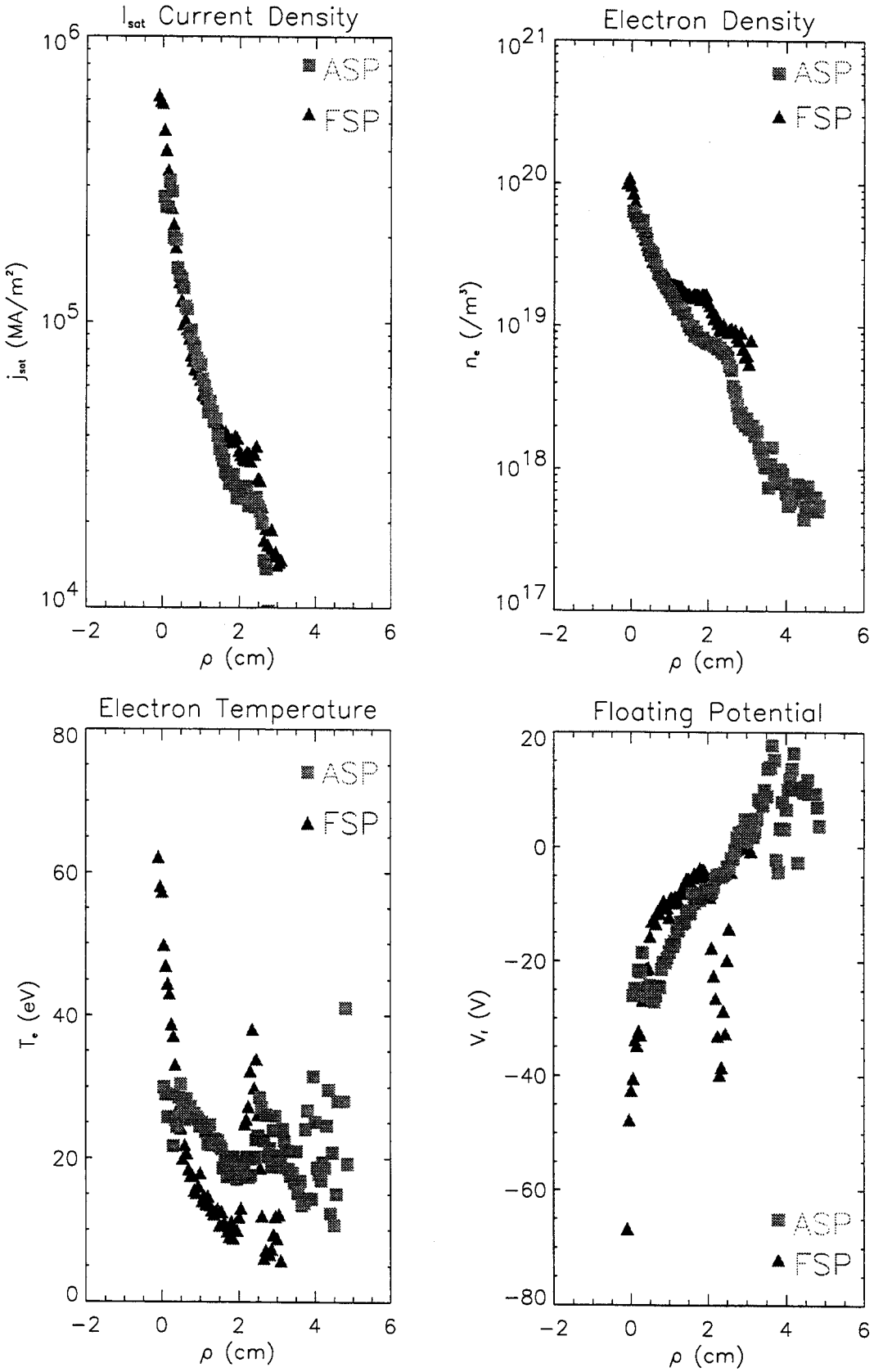

Figure 4.2: Comparison of ASP and FSP Data

three regions: $\rho < 0.5$ cm, $0.5 < \rho < 2.7$ cm, and $\rho > 2.7$ cm. In the first region, closest to the plasma, the densities measured by the two probes are similar, and are characterized by a short density gradient scale length, $L_n \sim 2$ mm. In the middle region L_n is bigger and $L_n^{FSP} > L_n^{ASP}$. The third region is demarcated by the steep density fall-off at $\rho \sim 2.7$ cm, and extends all the way to the wall at $\rho \sim 6$ cm. The limiter was at $\rho \sim 1.5$ cm for these shots. It is possible that at large ρ the densities are anomolously low because the probe has depleted the flux tube it is measuring.

The electron pressure p_e and the plasma potential V_p are loosely calculated as $p_e = n_e T_e$ and $V_p = V_f + 3T_e$. The composite profiles shown in Figure 4.3 indicate that p_e measured by the two probes is similar, except that the perpendicular pressure gradient measured by the FSP increases inside of $\rho = 0.5$ cm while the pressure gradient measured by the ASP does not. It is remarkable that the two probes measure the same p_e outside the limiter radius $\rho = 1.5$ cm. A greater mystery is presented by the ASP V_p profile, which differs greatly from the ASP V_P profile, being nearly completely flat inside the limiter radius, indicating the absence of radial electric field $E_r = 0$. The FSP finds $E_r \sim 10$ KeV/m just outside the separatrix. The flatness of the RF V_p profile may be traced to the flatness of the T_e profile.

4.2 Parallel Ohm's Law

The most sophisticated test of the relation between data from the two scanning probes is the attempt to verify Ohm's law along a magnetic field line. Starting from the two-fluid equations, and neglecting electron inertia and viscous effects, the momentum equation for electrons reads

$$\nabla p_e - en\left(\vec{\mathbf{E}} + \vec{\mathbf{u}} \times \vec{\mathbf{B}}\right) + \vec{\mathbf{R}} = 0,$$

where $\vec{\mathbf{u}}$ is the electron flow velocity and $\vec{\mathbf{R}}$ describes the momentum gained by electrons from collisions with ions. Taking the parallel component of this equation

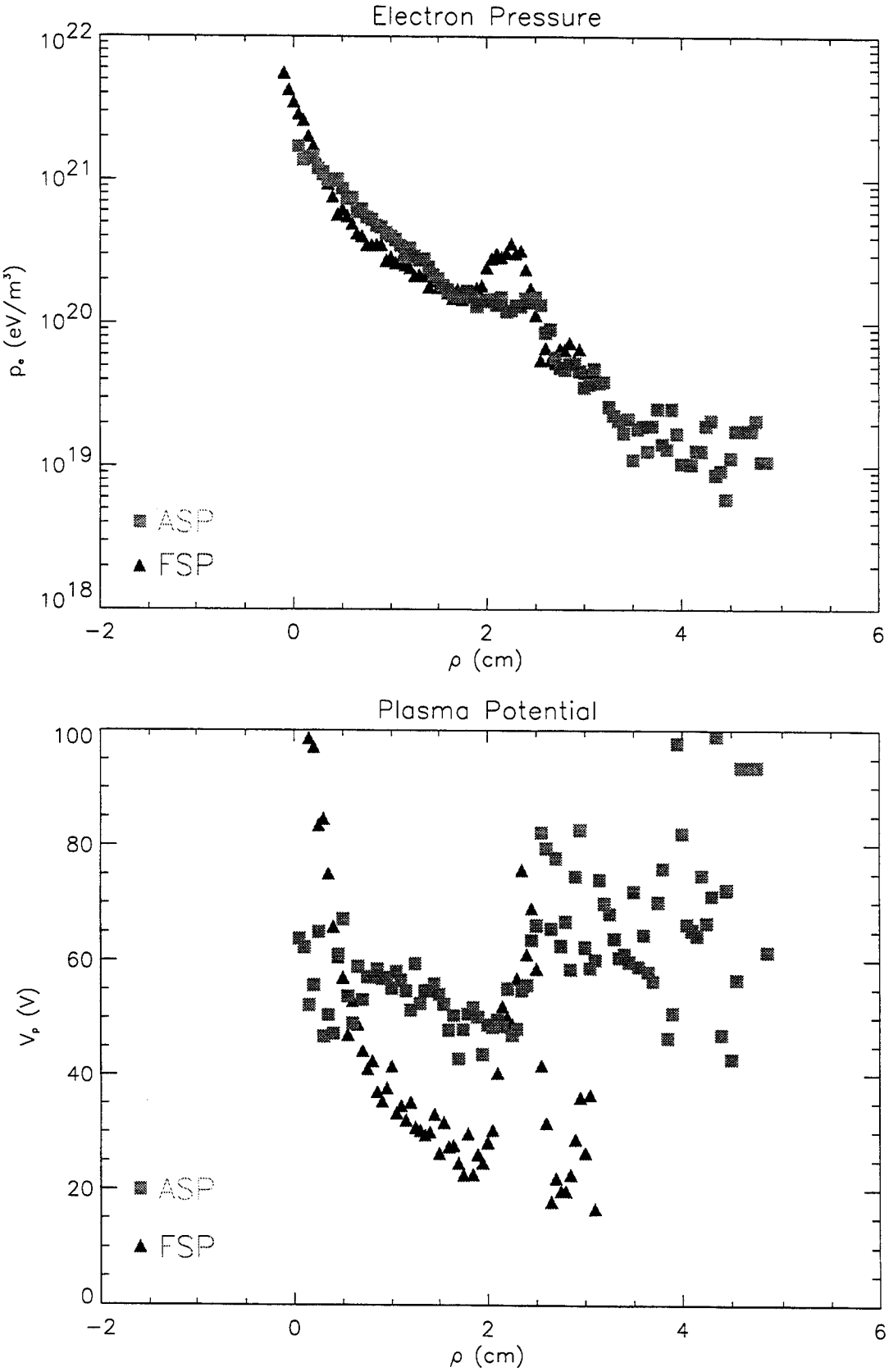

Figure 4.3: Comparison of ASP and FSP p_e and V_p

gives [39]:

$$-\frac{\partial p_e}{\partial x} + en\frac{\partial \phi_p}{\partial x} + en\frac{j_x}{\sigma_{\|}} - 0.71n\frac{\partial T_e}{\partial x} = 0,$$

where ϕ_p is the plasma potential, j_x is the current along a field line, $\sigma_{\|}$ is the parallel conductivity, and x denotes the coordinate which increases along a field line. For the temperatures measured by the probes, the parallel resistivity $1/\sigma_{\|} \leq 5 \times 10^{-6}$, and under the reasonable assumption that the parallel current $j_x \sim j_{sat}^{ion}$, the friction term is small compared to the other three terms. The parallel Ohm's law becomes,

$$-\frac{\partial p_e}{\partial x} + en\frac{\partial \phi_p}{\partial x} - 0.71n\frac{\partial T_e}{\partial x} = 0, \tag{4.1}$$

in which form it has been used as an input to a 2-D fluid code describing the plasma profiles in the SOL of TEXTOR [40]. This equation is non-linear and cannot be integrated without knowledge of the functional form of $n(x)$. To test whether this law holds by analysis of the data from the two probes at our disposal, we use the density measured by the FSP $n(x) = n^{ed}$, and replace the gradients

$$\frac{\partial}{\partial x} \longrightarrow \frac{\Delta}{d}$$

with the differences Δ between the measurements of the two probes (the distance, d, between the two probes measured along a field line is common to all terms and drops out).

In the Ohmic case, Equation 4.1 appears to be well satisfied, as shown in Figure 4.4. All three terms in Equation 4.1 vary significantly over the final 5 mm of the probe scan, but their sum remains zero.

4.2.1 Comparison to Other Diagnostics

Measurements by all available diagnostics of the edge density profile of an Ohmic plasma are compared in Figure 4.5 [2]. The squares linked by a line is an Abel inversion

[2] A program which facilitated this comparison was provided by Dr. Jim Irby.

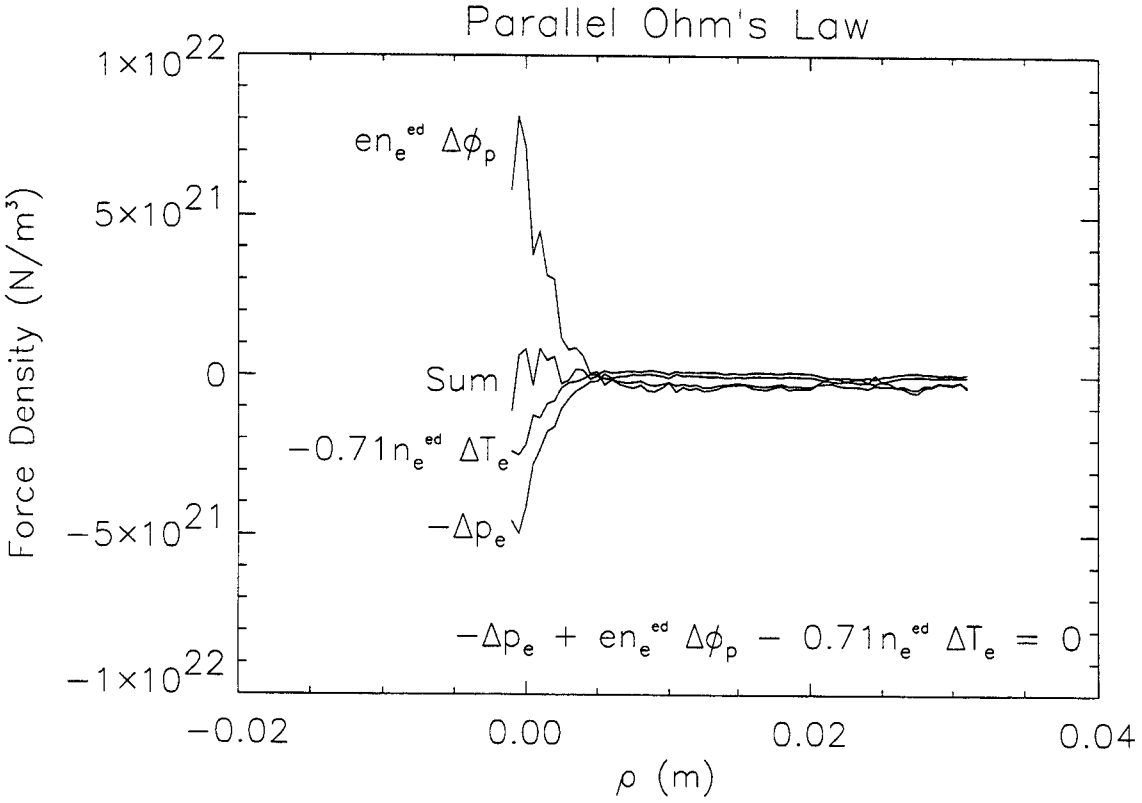

Figure 4.4: Test of Parallel Ohm's Law during Ohmic Operation

of the line-averged densities provided by the 10-channel Two Color Interferometer. The diamonds are from the Thompson Scattering diagnostic. Error bars show the absolute error. The triangles are the uncalibrated reflectometer data. The EFIT separatrix is the vertical line. The two scanning probes provide the best absolute density measurement outside the separatrix for $n_e \geq 3 \times 10^{18}$, and have been used to provide calibration for the reflectometer, which provides continuous density-profile measurements. The reflectometer calibration is not yet independent of the data given to it by the ASP.

4.3 Langmuir Probe data during RF Heating

The RF certainly has some effect on the edge but in order to accurately measure it with Langmuir probes, the possibility of sheath rectification has to be discarded; several previous studies have ignored this issue [41, 42]. Evidence of sheath rectification

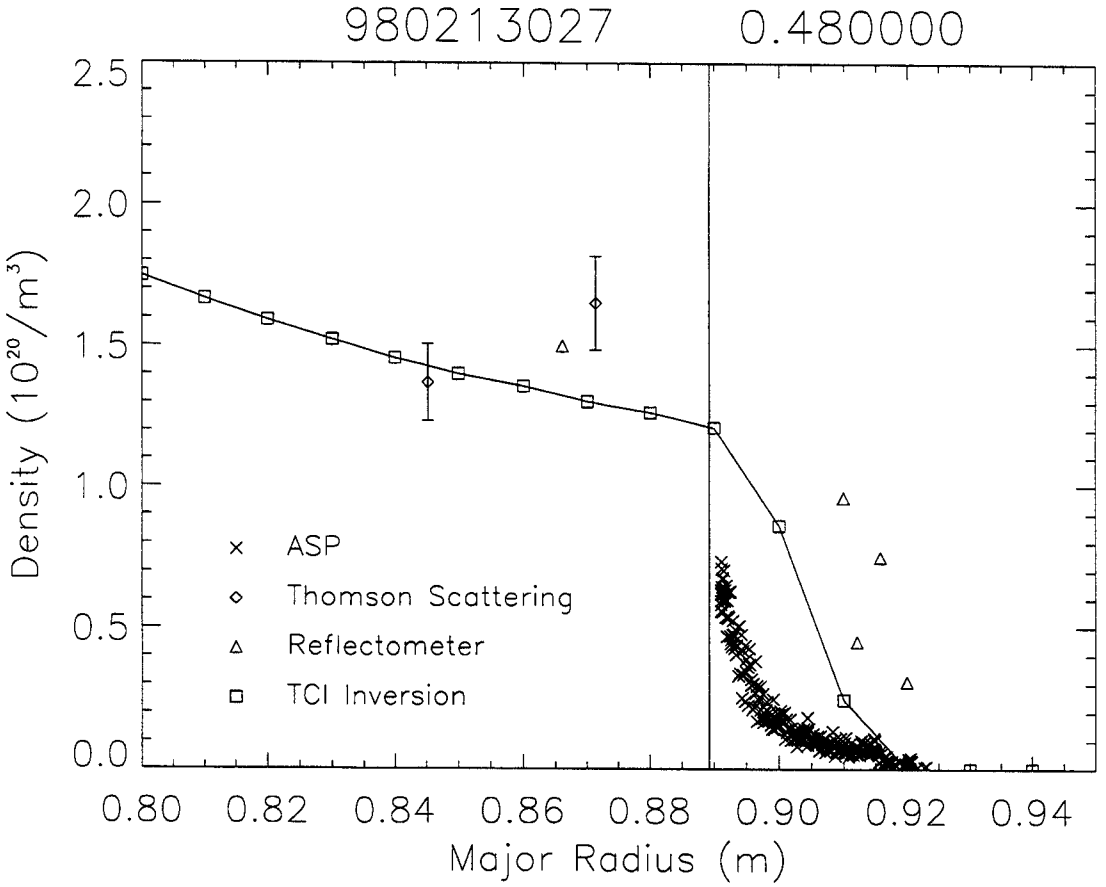

Figure 4.5: Comparison of Edge Density Measurements

is found on an important subset of C-Mod Langmuir probes. A technique of nullifying the sheath rectification by the use of quarter-wave stubs in the probe transmission line was attempted in this research, but mostly on probes which did not (as it turned out) suffer from sheath rectification.

4.3.1 Effect of RF on Langmuir Probes in C-Mod

As described in Appendix A, fluctuating RF potentials in a plasma are rectified in the Langmuir probe sheath, leading to a decrement ΔV_f^{sh} in V_f, an overestimate of T_e, and an underestimate of n_e. ΔV_f^{sh} is a "real" effect which occurs in sheaths surrounding all material objects, and which causes RF power to be lost in accelerating

ions into plasma-facing surfaces, as is discussed in detail in Section 4.6. An example of sheath rectification, taken from an FSP scan into an L-mode plasma during RF heating, is shown in Figure 4.6.

The most obvious signs of fluctuating RF potentials in C-Mod are seen on data from the Langmuir probe mounted in one of the protection tiles on the RF antenna (location shown in Figure 3.2), and on the FSP. $\Delta V_f \leq 350$ V have been seen on this probe, with $\Delta V_f \sim 100$ V being common. The magnitude of ΔV_f does not correlate with the confinement regime or the heating scenario.

The magnitude of ΔV_f seen on the FSP depends on both the confinement regime and on the heating scenario. It is larger in L-mode than in H-mode and larger during D(^{3}He) minority heating at 8 T than during D(H) minority heating at 5.4 T. In the worst case, 8 T L-mode, $\Delta V_f > 200$ V is seen on the FSP, a greater decrement than seen concurrently on the antenna probe. This is probably related to the poor absorption. For one such 8T L-mode shot, the absorbed power fraction was calculated to be $P_{abs} \sim 23\%$ at RF turn-off. During D(H) minority heating at 5.4 T, $P_{abs} \geq 50\%$ during L-mode, and the FSP measures $\Delta V_f \leq 30$ V.

The FSP does not appear to be affected by rectification during H-mode at 5.4 T. This may be due to the decrease in the edge density. The density (measured by the ASP) at the Faraday screen radius drops by a factor of two at the L-H transition, so that the fast wave cut-off density moves from being in the near vicinity of the Faraday screen surface to being 1cm in front of it. It is presumed that in the L-mode case that power can be coupled to waves other than the propagating fast magnetosonic wave which carry a fluctuating $E_{||}$ and lead to rectification when they reach a material surface such as a probe. The Langmuir probes on the front face of the GH limiter experience a greater or lesser amount of RF-related effects depending on their location on the side closer to or further from the RF antenna.

Sheath rectification has never been seen to occur in data from the ASP. Two Langmuir probes were set up to provide a paired comparison test of the method for preventing rectification described in [33]. One probe was outfitted with a quarter-

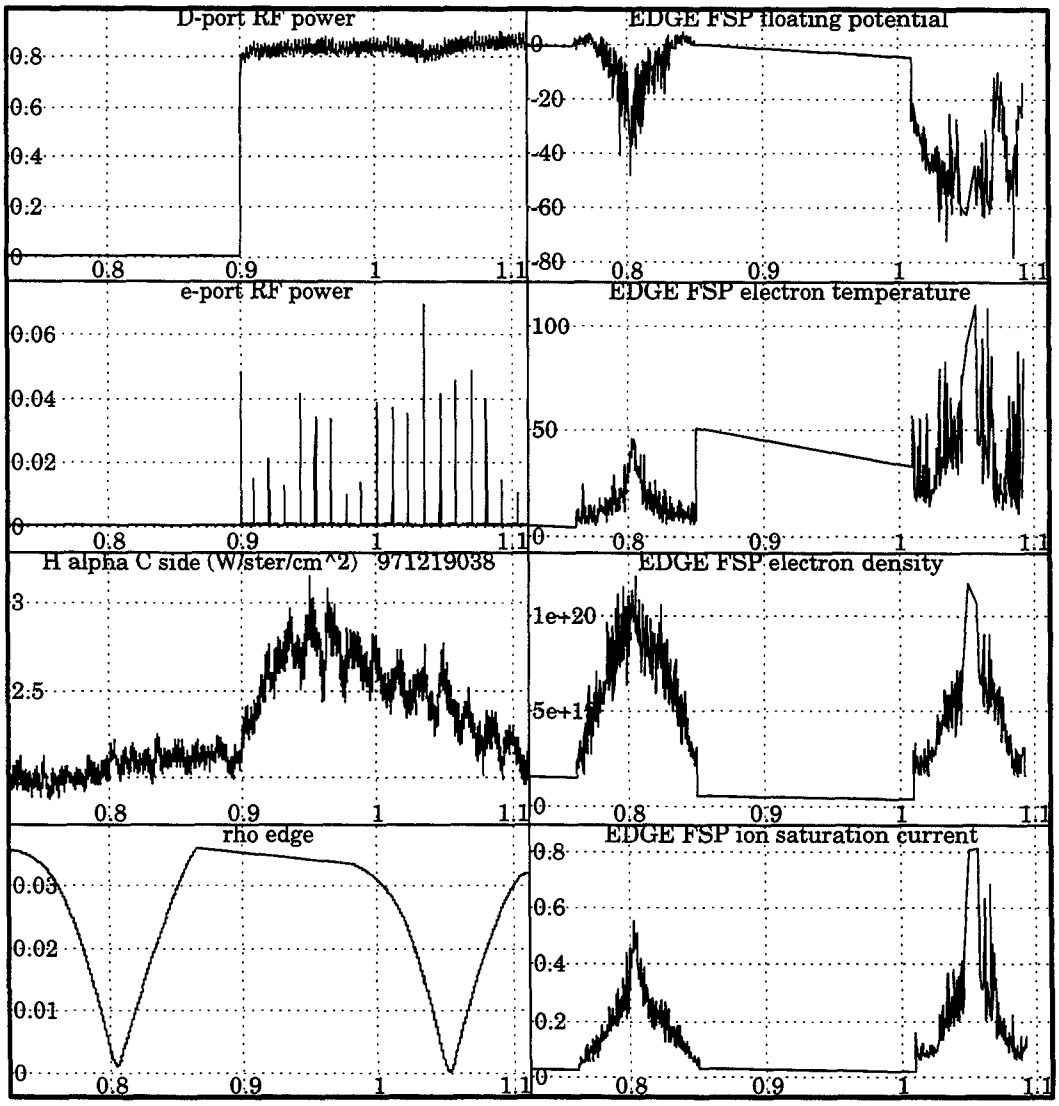

Figure 4.6: Rectification Seen on FSP in RF L-mode

wave stub, attached $3\lambda/4$ away from the probe tip, while another identical probe was not. No statistically significant difference between data from the two probes was observed. Furthermore, on shots where the RF tripped off during a probe scan, no sudden change was observed in the ASP data (changes were apparent at these times in the FSP data). Presumably, the ASP is sheltered from fluctuating RF potentials by its position, several ports away from the RF antennas.

Thus, having benchmarked the ASP against the FSP during Ohmic operation, and having seen no evidence of rectification on the ASP, it is concluded that the ASP provides reliable measurements of edge profiles both during H-mode and L-mode.

4.3.2 Effect of RF on the Plasma Edge

The difference between Ohmic L-mode and RF L-mode can only be measured by the ASP, since the FSP is affected by rectification during RF L-mode; it is not possible to verify the parallel Ohm's law during RF L-mode for this reason. ASP data show that conditions in the RF L-mode edge are similar to the Ohmic L-mode edge, as shown in Figure 4.7. Ohmic H-mode and RF H-mode could be compared if the probes were scanned in the brief time between RF turn-off and the H-L transition. Ohmic H-modes can be obtained readily at low magnetic fields, but these plasmas are more likely to disrupt and damage the probe. No probe scans into Ohmic H-mode have been attempted.

4.4 L-mode and H-mode Density Profiles

ASP measurements of RF L-mode and H-mode edge density profiles, taken on successive identical shots, are compared in Figure 4.8. At this range of locations, well outside the confinement barrier, the H-mode and L-mode scale lengths are seen to be approximately equal. A given density layer is thus approximately 1 cm further from the current strap ($r_{cs} = 0.934\ m$) in the H-mode case than in L-mode case, while the density at a particular material surface in L-mode is about twice what it is in H-mode. In L-mode the fast wave density cutoff $n_{\|}^2 = \mathcal{R}$ (see Section 4.5) occurs in

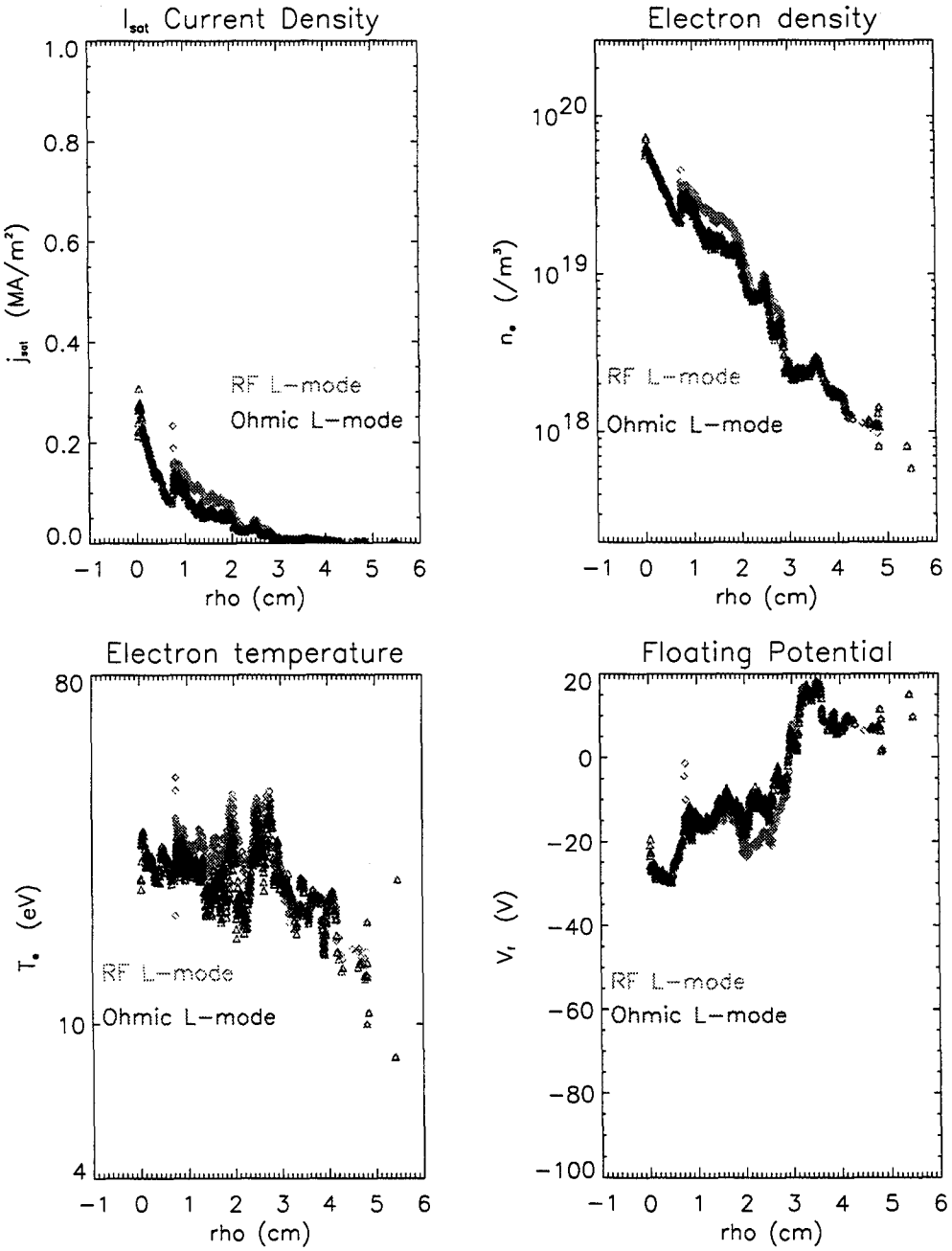

Figure 4.7: Comparison of ASP data during RF L-Mode and Ohmic L-Mode

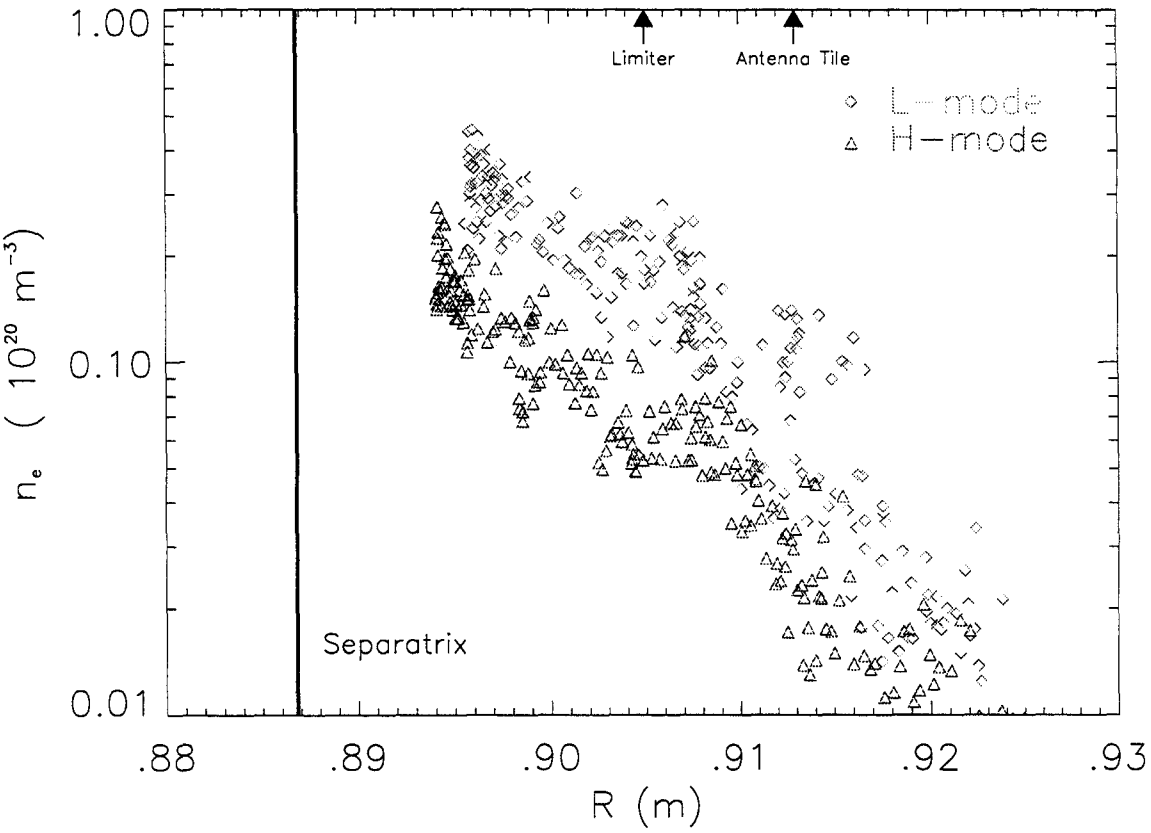

Figure 4.8: Comparison of L-mode and H-mode

the vicinity of the Faraday screen.

4.5 Coupling of RF Power to Propagating Waves

In the cold plasma limit, the edge density profile determines the transfer of fast wave power from the antenna to the plasma, due to the existence of an evanescent layer in the plasma edge. The design of the C-Mod antenna is intended to maximize the power coupled to the Fast Magnetosonic wave, also known as the Compressional Alfven wave, which is the solution of the dispersion relation

$$n_\perp^2 = \frac{(n_\parallel^2 - \mathcal{R})(n_\parallel^2 - \mathcal{L})}{\mathcal{S} - n_\parallel^2} \tag{4.2}$$

for low frequencies, such that $\omega \sim \omega_{ci}$ [43].

It is generally assumed that the $n_{||}$ of the propogating fast wave is fixed by the antenna geometry. The distribution of poloidal current in the antenna current straps may be approximated as a Fourier sum of toroidal modes. The data in this thesis was taken during $(0, \pi, 0, \pi)$ phasing, for which the currents in adjacent antenna current straps are 180° out of phase. Since the two-strap antennas occupy adjacent horizontal ports, of which there are 10, the dominant toroidal mode is $N_\phi = 10$. The different toroidal modes evolve independently.

Each toroidal mode couples to a propagating wave, on which it imposes a boundary condition on n_ϕ, the toroidal index of refraction,

$$n_\phi = \frac{ck_\phi}{\omega} = \frac{c}{\omega}\frac{N_\phi}{R}, \tag{4.3}$$

which is then fixed as the wave propogates away, under the assumption of axisymmetry ($\frac{d}{d\phi} = 0$). $N_\phi = 10$ corresponds to $n_\phi \sim 6.5$, if R is taken to be the major radius of the plasma at outboard midplane ($R = .9$ m).

The magnetic field in C-Mod is predominantly toroidal, so that $n_{||} \approx n_\phi$. If $n_{||}$ is fixed then the wave will be cut off at

$$n_{||}^2 = \mathcal{R}, \tag{4.4}$$

which sets a condition on the density if ω is fixed and ω_{ci} varies slowly:

$$\omega_{pi}^2 = (n_{||}^2 - 1)(\omega + \omega_{ci})\omega_{ci}. \tag{4.5}$$

Taking the dominant $n_{||}$ of the fast wave to be 6.5, and using the parameters of an Alcator fiducial shot ($B_0 = 5.4$ T, $f_{RF} = 80$ MHz), then in the vicinity of the outboard plasma edge this cutoff density is

$$n_{\mathcal{R}} = 6 \times 10^{18}\ m^{-3}, \tag{4.6}$$

which is measured by the scanning probes to occur a few centimeters in front of the current strap (at midplane, the front of the current strap is at R=93.4 cm, the front of the Faraday shield at 91.6 cm). This means that the RF fields must tunnel through an evanescent region in order to couple to the propogating fast wave.

4.5.1 Estimation of Tunneling Factor

In a 1-d slab model where $\mathbf{B} = B(x)\hat{\mathbf{z}}$ and all plasma quantities are functions of x, the electric field which couples to the fast wave is in the $\hat{y}$ direction and is written

$$E_y = E_0 e^{i(k_x x - \omega t)}, \tag{4.7}$$

where E_0 is the electric field at the antenna current strap. Note that k_x is purely imaginary in the evanescent region. The tunneling factor η_{FW} is the ratio of E_0 to $E_{\mathcal{R}}$, the electric field at the cut-off layer, and is given by

$$\eta_{FW} = \int_{current\ strap}^{n=n_{\mathcal{R}}} ik_x dx, \tag{4.8}$$

where $\eta_{FW} \leq 1$ corresponds to good coupling[3], and the efficiency X of fast wave launch is

$$X = \frac{P_{FW}}{P_{c.s.}} = \frac{|E_{\mathcal{R}}^2|}{|E_0^2|} = e^{2\eta_{FW}}, \tag{4.9}$$

[3]Good coupling may even be obtained for $\eta_{FW} \leq 5$ if a perfectly reflecting metallic structure is assumed as the outboard boundary condition, since the wave suffers no absorption in the evanescent layer, through which it may make multiple passes [44].

where P_{FW} is the net forward power leaving the antenna. Solving 4.2 for k_x gives

$$k_x^2 = \frac{\omega^2}{c^2}\left[1 + \frac{\omega_{pi}^2}{\omega_{ci}(\omega_{ci}+\omega)} - n_{\|}^2\right], \tag{4.10}$$

where the right hand side is a function of the density and magnetic field.

The difference in tunneling between L-mode and H-mode ought to be due solely to the different density profiles in the evanescent region. Using the profile fits from Figure 4.8, we find that the coupling should be good in both cases:

$$\begin{aligned} &\text{L Mode:} \quad \eta_{FW} = .17 \quad X = .72, \\ &\text{H Mode:} \quad \eta_{FW} = .27 \quad X = .58 \end{aligned} \tag{4.11}$$

Due to the possiblility that the wave may make multiple passes through the evanescent layer in front of the antenna, the coupling is not a good predictor for the heating efficiency P_{abs}/P_{FW} (which, in fact, is seen to be higher in H-mode than in L-mode). Instead the coupling should be proportional to the loading resistance, which is generally lower in H-mode than in L-mode.

4.5.2 Effect of Edge Profiles on Antenna Loading

If the antenna loading were dominated by power coupled to the fast wave, changes in coupling to the fast wave would be indicated by changes in antenna loading. Movement of the evanescent layer could therefore be responsible for changes in the antenna loading between L-mode and H-mode of on the order of 20 %. A similar conclusion was reached concerning antenna loading on D-III-D during a different heating scenario (high harmonic fast wave heating with a recessed antenna) [45], and on JT-60 [46], where the evanescent layer lies inside the separatrix. Changes in antenna loading of this order are in fact often seen during L-H transitions on C-Mod, and are likely to be due to movement of the evanescent layer.

Figure 4.9 shows the factor-of-two changes in antenna loading which are seen on occassion during L-H transitions and type I ELM's on C-Mod, as they were on D-III-

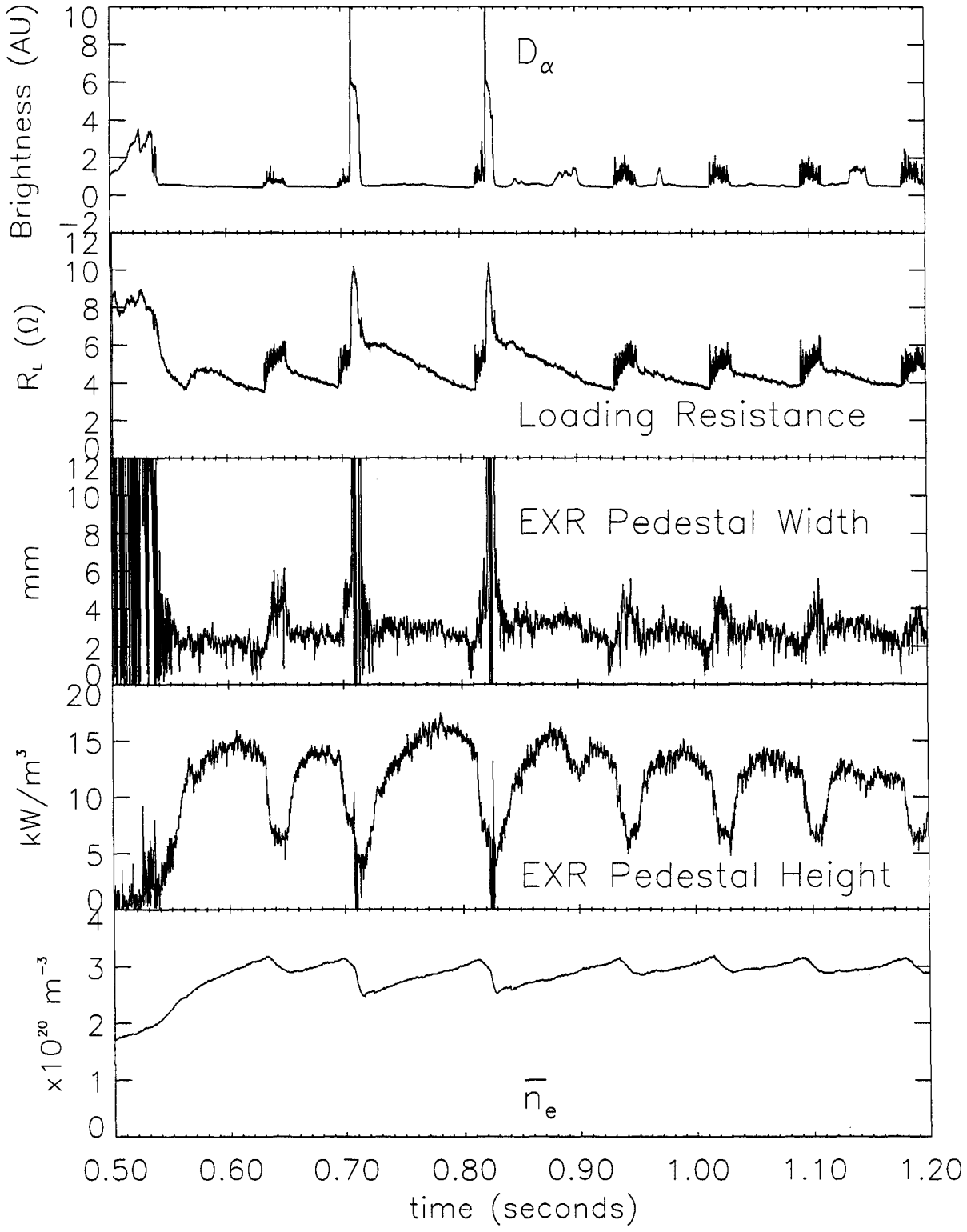

Figure 4.9: Comparison of Antenna Loading and Edge X-ray Emissivity

D, and which are too big to be explained by movement of the evanescent layer. On the first trace, showing the D_α brightness, an L-H transition can be identified at 0.54, 0.72, and 0.83 seconds, with type I ELM's occuring at 0.65, 0.94, 1.02, 1.10, and 1.19 seconds. The second trace shows the antenna loading, which changes by a factor more than two during the L-H and H-L transitions, with a change on the order of 20 % at the times of the ELMs. [45], following the analysis of [47], argues that large changes in the antenna loading are due to the change in the density gradient near the edge, with steeper gradients causing greater reflection of the incident fast wave and thereby lowering the loading. On C-Mod the best measurement of the edge density at the radius where the gradients are largest, which is near the H-mode confinement barrier a few mm inside the separatrix, is the edge X-Ray emissivity diagnostic [48]. This diagnostic returns an edge emissivity profile which is roughly proportional to $n_e * n_{IMP}$, where n_{IMP} is an impurity density, specifically the density of fully stripped Fluorine. During H-Mode the emissivity profile shows a narrow region with steep gradient, which is thought be associated with the H-mode confinement barrier. The width and height of this pedestal are shown in the third and fourth traces; both clearly show effects of transitions in and out of H-mode and also ELM's. An attempt was made to find a correlation between the edge X-ray pedestal parameters and the antenna loading, but no connection was found. As will be discussed in Chapter 5, it has been discovered that the C-Mod antenna loading is sensitive to changes in the plasma core, specifically those associated with the sawtooth crash (see Figure 5.13). The change in loading during transitions in and out of H-mode may not be caused by changing edge conditions, but rather by changing conditions in the main plasma. The loading resistance decreases slowly during the ELM-free phases, roughly in proportion to the increase in the line averaged density (shown in the fifth trace).

4.6 Limiter-Circuit Sheaths

It is expected that large RF potential fluctuations will be found on magnetic field lines that connect nearby metallic surfaces in the vicinity of the antenna, thus form-

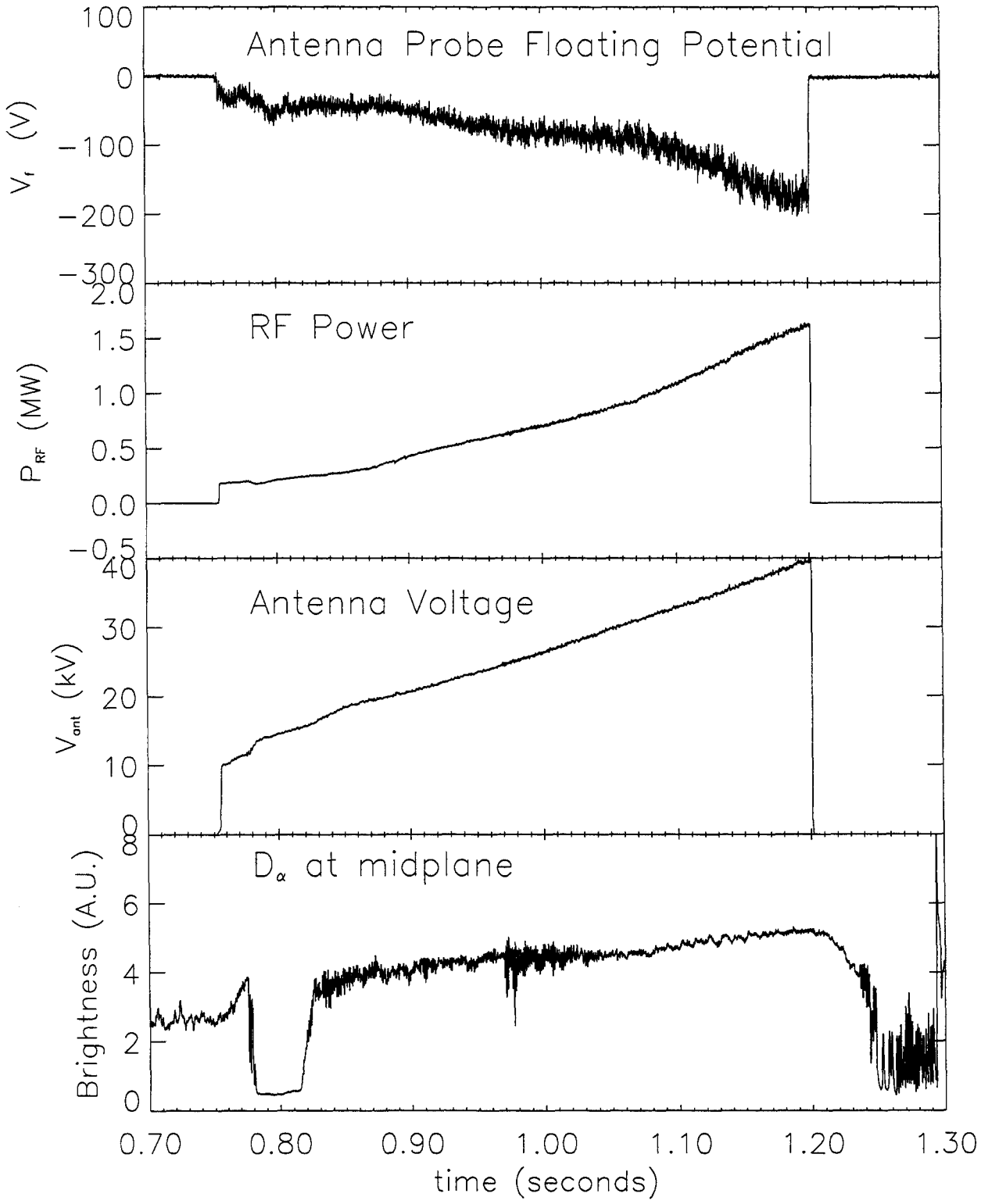

Figure 4.10: Probe Response to RF Power Ramp

ing a low-resistance circuit. Two circuits which have been studied on tokamaks are the "gap" circuit between neighboring Faraday screen elements, caused by misalignment of the elements and the steady-state magnetic field; and the "front-face" circuit connecting Faraday screen elements to antenna side protection tiles, or antenna side protection tiles to each other (see [49] for recent work, and [50] and the references therein). The RF magnetic flux linking such a circuit induces an RF electric field, which is restricted to the sheaths at either end of the magnetic field line if the plasma density is high enough [51]. A theoretical sketch of these "rf sheaths" is given by [52], and the variation of plasma quantities along a field line is modelled in [51].

The data shown in Figure 4.10 comes from an antenna probe which lies on a field line that connects to the AB limiter (Figure 4.11). "Limiter" circuits have been mentioned in the literature [53], [54], but have not received as much attention as the gap and front-face circuits. Figure 4.10 shows V_f measured by this probe while the power coupled to the D-port antenna is being ramped up. V_f (first trace) tracks the D-port RF power (second trace) somewhat more closely than the voltage on the D-port antenna[4] (third trace), and is insensitive to changes in confinement regime (L-mode, changing to ELM-free H-mode at 0.78 s,

Before identifying limiter circuits as the cause of this RF-related ΔV_f^{RF}, a number of other possible explanations must be evaluated. For example, an increase in T_e would cause $V_f \sim V_p - 3T_e$ to decrease. However, at the radius of the antenna tiles, $T_e \sim$ 20 eV $\ll |V_f|$, with no sign of many-fold increase on any of the other probes during RF. Then also, locally produced suprathermal electrons would cause a lowering of the floating potential, but this would depend on local plasma density, which changes at the L-H transition, while the observed ΔV_f^{RF} does not.

There are two reasons to suppose that ΔV_f^{RF} is not due to RF being rectified by the probe card electronics. The installation of a quarter-wave stub in the line at a

[4]What is shown is the maximum voltage in the resonant loop which drives the antenna. The resonant loop ensures that the power is divided evenly between the two straps, and that the phase between them remains locked at either 0 or π (π for all data in this research). The inductive part of the antenna impedance doesn't change much no matter what the plasma does (unlike the real part of the antenna impedance), so the voltage at the top of the current strap is a constant (albeit unmeasured) fraction of the maximum voltage in the resonant line for all plasma operation.

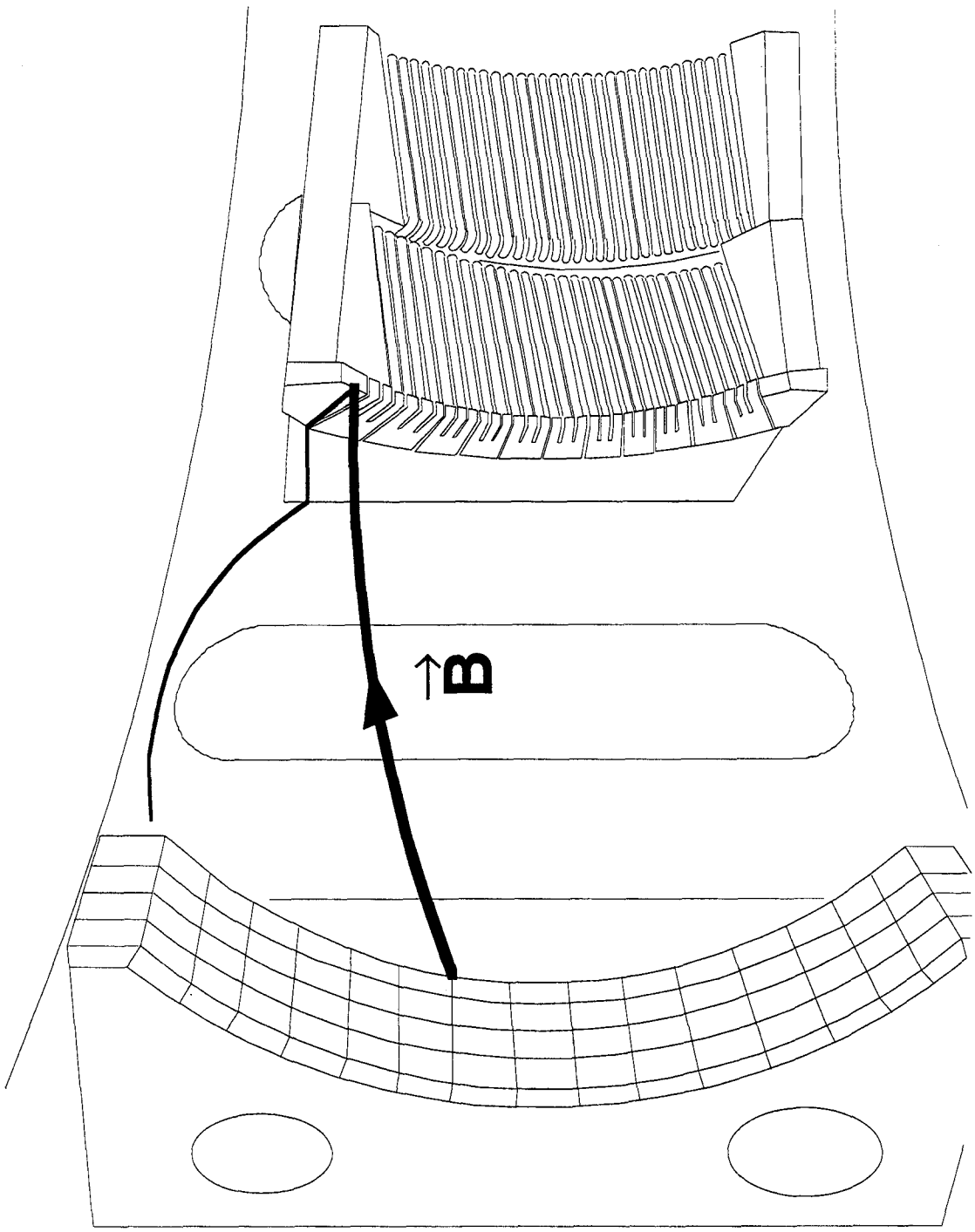

Figure 4.11: Limiter Circuit

place where it would function as an "RF trap" did not reduce ΔV_f^{RF}; and application of RF voltage at the probe input during bench tests caused gross electrical failures in the electronics well below the voltages necessary to produce the appropriate DC signal on the probe "Voltage" output. Therefore the potential of the probe tip must be effectively constant, with the large RF voltage drop occuring across the probe sheath. In the absence of other causes, ΔV_f^{RF} must be due to RF fluctuation in V_p. Then if the the Langmuir probe, which is embedded in the antenna protection tile, measures a floating potential which is many times T_e negative, then the antenna tile (which is at ground) must be drawing a significant electron current, as the TEXTOR ICRF antenna was found to do [41].

For a dense plasma the decrement in the floating potential due to sheath rectification is simply related to the magnitude of the RF potential fluctuations. The plasma must be dense enough to shield out the induced RF voltage from the main plasma, that is [51]

$$\Delta = \lambda_{De}(eV/T_e)^{3/4} \ll L \tag{4.12}$$

where Δ is the sheath thickness and L the length of the field line. This is well-satisfied for the limiter circuit ($n_e \sim 10^{18}/m^3$, $L \sim 1m$). In this case, when $eV_{RF}/T_e \gg 1$, $V_F \sim 0.6V_{RF}$ [49]. V_{RF} is defined as the zero-to-peak RF potential difference between the two surfaces; since the sheaths are symmetric, half of the voltage drop appears at each sheath, and the potential of the field line is always positive with respect to either surface, thus confining electrons and accelerating ions into both surfaces.

4.7 Coupling of RF Power to Limiter Circuit Sheaths

The energy lost to acceleration of ions in the sheath is given by [49]

$$P_{sh} = \int Ze\Delta V_f^{sh} J_i^{sat} dS \tag{4.13}$$

where J_i^{sat} is the ion saturation current density, and the integral is to be taken over all metallic surfaces, thus including the sheaths at both ends of each field line. We

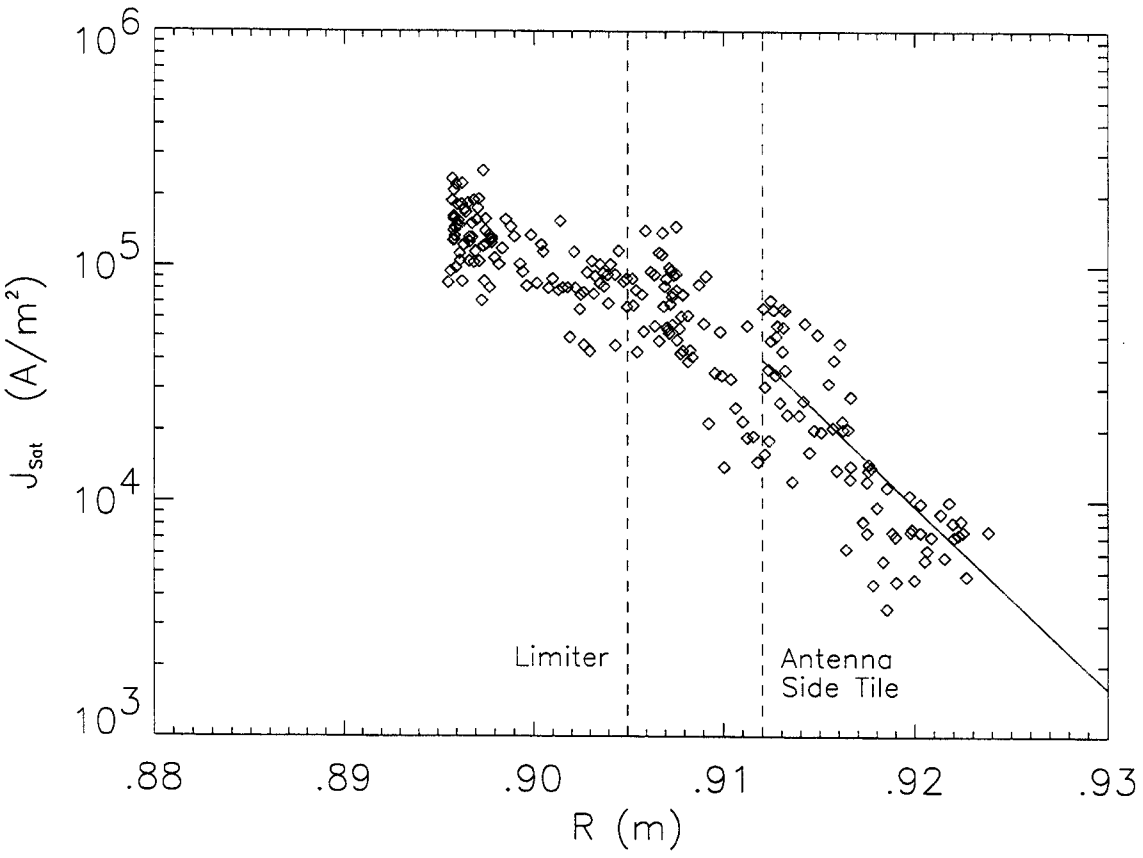

Figure 4.12: J_{Sat} Profile in RF L-mode

can estimate the power lost to sheaths in limiter circuits by applying Eq. 4.13 to the field lines which connect the antenna side tiles to the limiters. Figure 4.12 shows an RF L-mode J_i^{sat} profile with the location of the limiter and antenna side tiles shown, and a model exponential profile. Integrating over this model profile over the antenna side tiles, and assuming ΔV_f^{rect} is constant over the poloidal extent of the antenna,

produces an estimate

$$P_{sh}^{L} = 50kW \pm 50\% \tag{4.14}$$

for the power deposited in limiter-circuit sheaths during L-mode.

We can estimate the importance of the limiter-circuit sheaths to the global RF power balance by comparing P_{sh} to P_{abs}, the amount of RF power absorbed by the plasma. This is best diagnosed from the break-in-slope of the plasma stored energy W_{pl} at RF turn-off [55]:

$$P_{absorbed} = \left.\frac{dW_{pl}}{dt}\right|_{turn-off}, \tag{4.15}$$

where W_{pl} is calculated by EFIT. This number can be compared to P_{RF}, the difference between the forward and reflected power in the resonant loop driving the antenna, which is well-diagnosed. The derived heating efficiency $\eta = P_{abs}/P_{RF}$ is often much less than one. The destination of the remaining power is at present unknown. On shot 980123034 the ASP was scanned at RF turn-off in order to find out how much of the unabsorbed RF power is invested in limiter-circuit sheaths. At the time of RF turn-off the plasma is in an EDA H-mode. Figure 4.13 shows the time histories of P_{RF}, W_{pl}, and the antenna probe V_f, along with the J_{sat} profile from the ASP. The break-in-slope analysis indicates a heating efficiency $\eta = .53$.

Taking V_f to be $60V$, then integrating over the J_{sat} profile gives

$$P_{sh}^{H} = 30kW \pm 50\%, \tag{4.16}$$

which indicates that limiter-circuit sheaths do not play an important role in the global power balance.

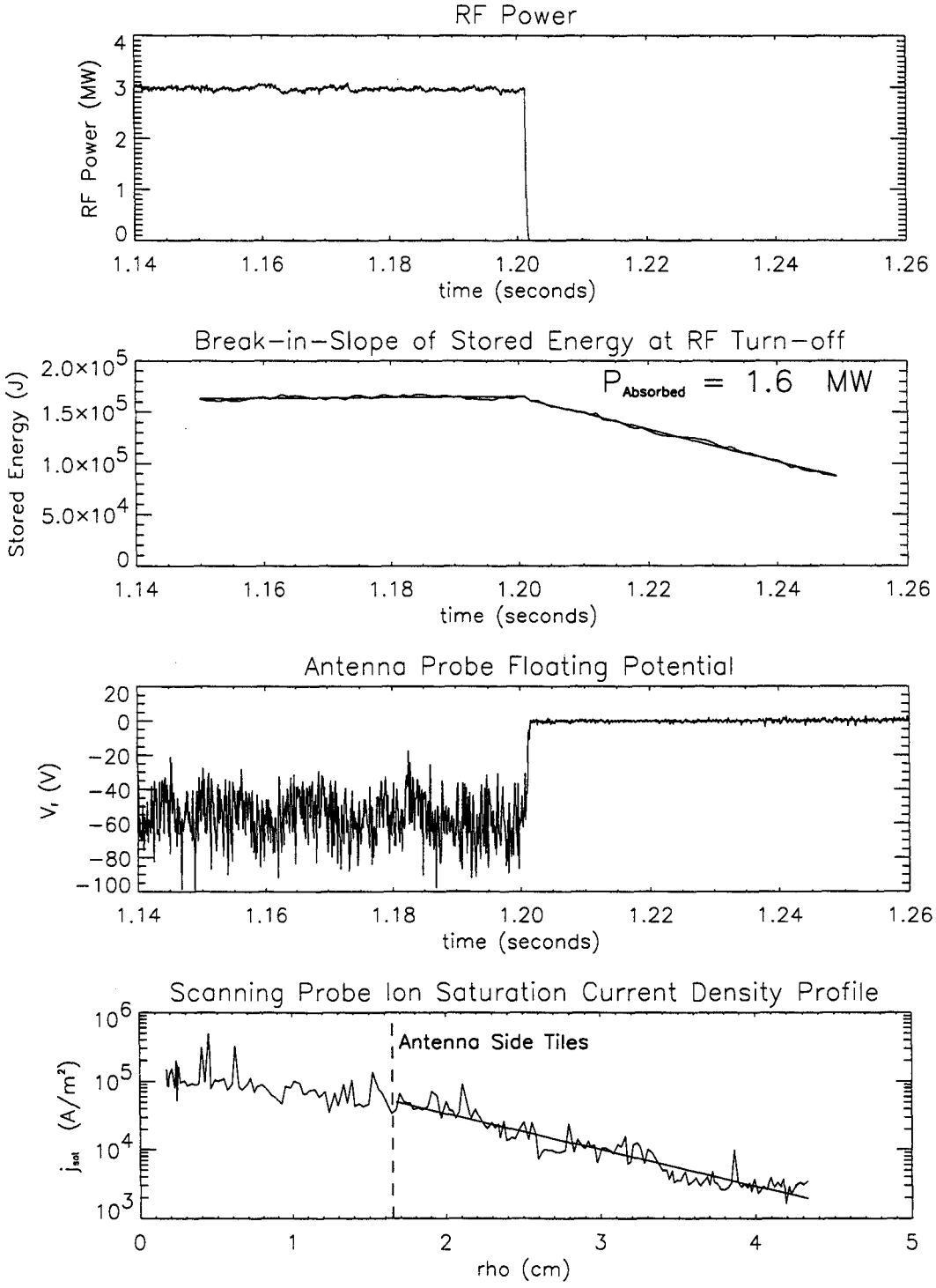

Figure 4.13: Plasma Behavior at RF Turn-off

Chapter 5

Fast Wave Transmission Measurements

This chapter concerns loop probe measurements of magnetic fields associated with the fast wave. The voltage induced on the loop probe is written

$$\widetilde{V_{loop}} = V_{loop} \cos(\omega t + \Phi_{loop}) \tag{5.1}$$

and can give two pieces of information—an amplitude V_{loop}, and a phase Φ_{loop}—which can be combined with other measured quantities to diagnose the disposition of the fast wave fields. This chapter concerns the loop probe signal amplitudes. The fast wave launchers used during the 1997-1998 run campaign were the D-port antenna (the D-port transmitter operated at 80.5 MHz), and the E-port antenna (the E-port transmitter operated at 80 Mhz), for all data in this chapter.

The analysis of probe signal amplitudes begins with the definition of the transmission factor T_{IW}:

$$T_{IW} = \frac{P_{loop}}{P_{RF}} = \frac{1}{Z_0}\frac{V_{loop}^2}{P_{RF}}, \tag{5.2}$$

where P_{RF} is the power measured leaving the antenna and Z_0, the impedance of the probe line and its termination, is 50Ω. T_{IW} for a given probe is found to vary not

only from one shot to the next, but also during a shot.

Scans of minority concentration in D(H) at 5.4 T (on 18 and 19 February, 1998) and D(^{3}He) at 7.9 T (on 12 February 1998) provided the most useful data. During these scans other parameters which might affect T_{IW}, such as the inner and outer gaps, and the target density, were kept constant. As described below, T_{IW} was found to be well-predicted by a single-pass analytic theory and by the computer code FELICE in D(H) at 5.4 T, which has high single-pass absorption. For D(^{3}He) at 7.9 T, which is predicted to have low single-pass absorption, T_{IW} is not well-predicted by theory.

T_{IW} was observed to show modulation with the same timing as the sawtooth instability. Careful examination of this timing showed that the modulation of the probe signals was synchronous with the central channels of T_e as measured by the Grating Polychromator (GPC), and not with the edge channels. This hitherto-unreported phenomenon can be explained by the single-pass theory on the assumption that the minority density profile is more radically affected by the sawtooth crash than the electron density profile.

5.1 Vacuum Tests and Benchmarks

In the absence of plasma, $P_{RF} \leq 50$ kW can still be launched from each antenna. Data from two vacuum test shots is shown in Figure 5.1. The D-port antenna was pulsed on the first test shot, the E-port antenna on the second. Data from the two shots are superimposed on the assumption that the antennas create identical field patterns; the x-axis is toroidal angle from the centerline of the active antenna. There appears to be a field null at $\phi = 7°$. The signals from one side of this field null are all in phase with each other, and 180° out of phase with signals from the other side. This is a signature of a standing wave (no net energy flow). The toroidal mode spectrum is symmetric about $n_{tor} = 0$. The power detected at each probe is linearly proportional to the input RF power.

During plasma operation T_{IW} is usually higher than during vacuum tests, except at very high Hydrogen concentration during D(H) heating at 5.4 T. The largest

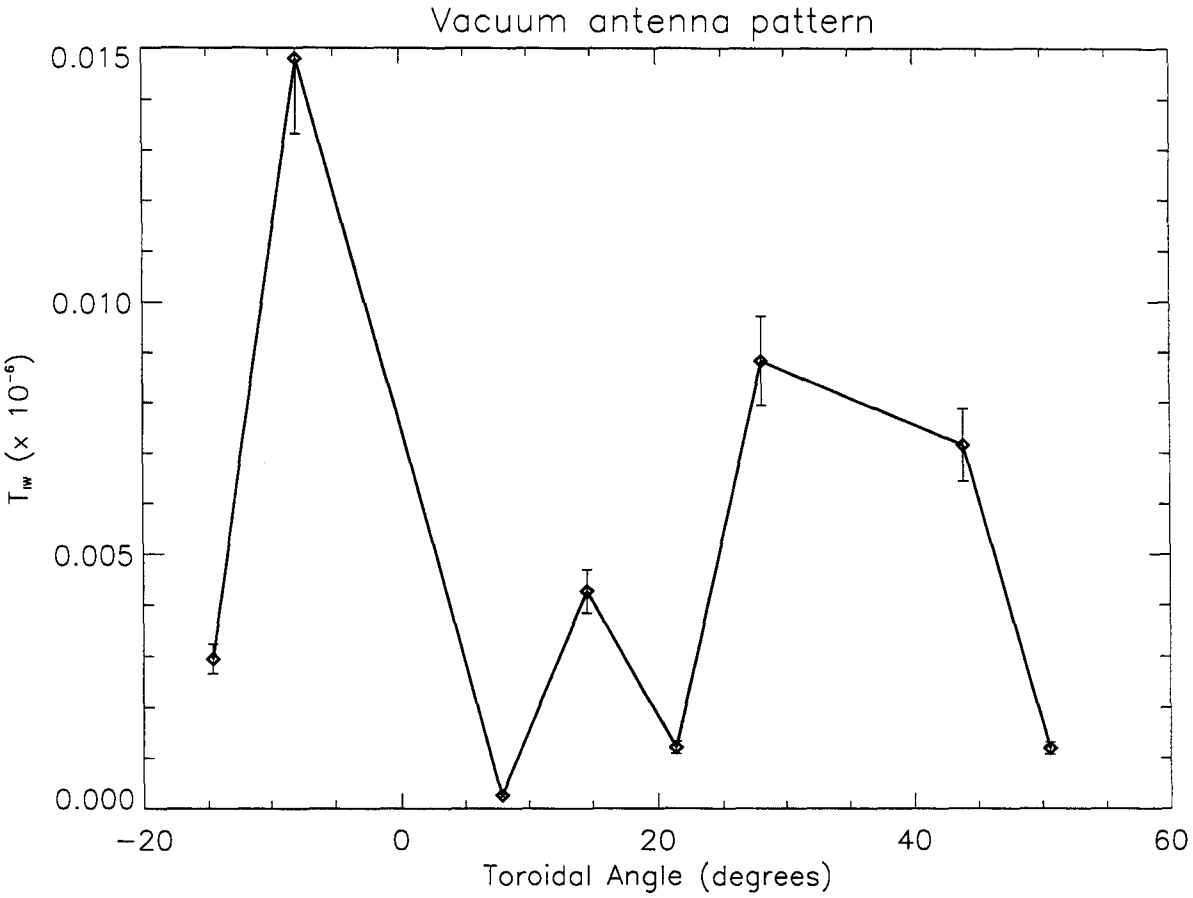

Figure 5.1: Inner Wall Loop Probe Signals During Vacuum Test

fields seen by the probe, which occur during D(^{3}He) heating at 7.9 T, correspond to $\tilde{B}_{RF}^{tor} \sim 2 \times 10^{-3}$ T at the probe. An in-vessel calibration performed after the run campaign indicated that the RF fields at the probes are attenuated by a factor $B_{ts}/B_{probe} \sim 20$ relative to the field B_{ts} at the tile surface, allowing an upper limit to be established of $B_{ts} \leq 5 \times 10^{-2}$ T at the tile surface.

5.2 Analytic Transmission Theory

Heating of a two-species plasma by fast magnetosonic waves was first discovered experimentally in the early 1970's and later quantified by T.H. Stix in 1975 [56]. The introduction of a small amount of a second *minority* species with Z/M higher than

the majority species allows the minority species to absorb some of the wave power at the location where the wave frequency ω is equal to the minority cyclotron frequency Ω_{cm}. The presence of the minority species also creates an evanescent layer in the middle of the plasma, on the high-field side of the minority cyclotron resonance. As the fast wave propagates in from the low-field side, it encounters first the $\omega = \Omega_{cm}$ resonance layer, then the $n_{\|}^2 = \mathcal{L}$ cutoff, then the $n_{\|}^2 = \mathcal{S}$ resonance. A diagram of this situation is shown in Figure 5.2.

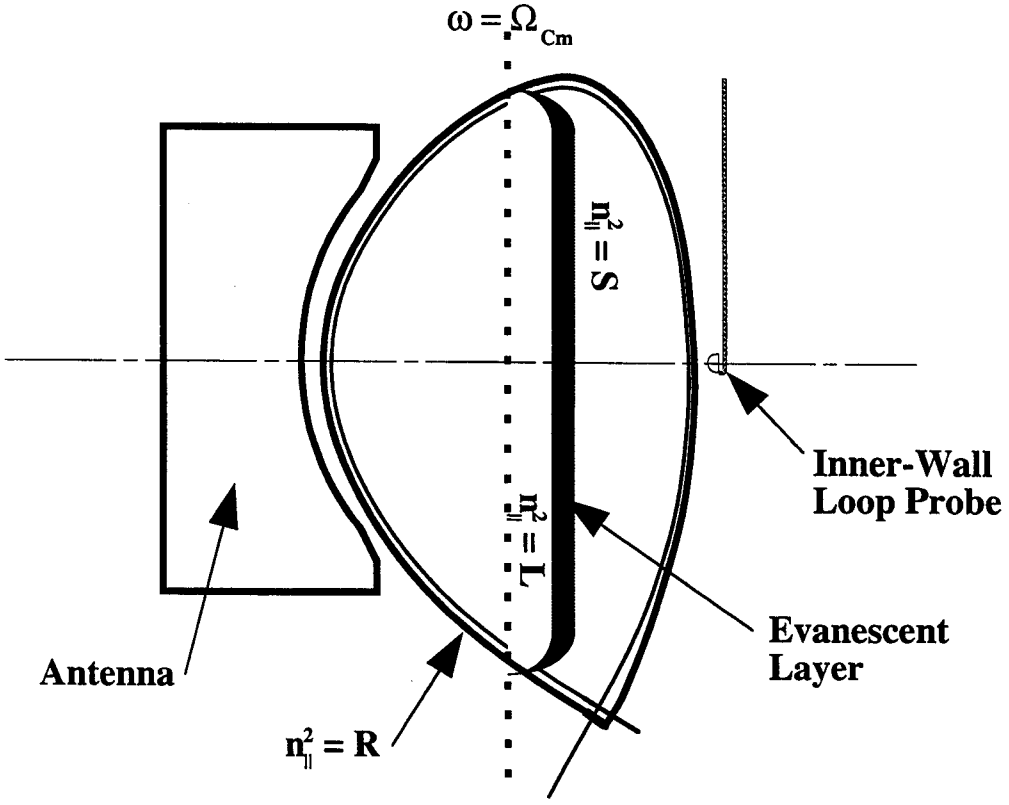

Figure 5.2: Cartoon of Fast-Wave Propagation

5.2.1 Simplifying Assumptions

The fraction of power transmitted through the resonance-cutoff-resonance triplet in the center of the plasma may be calculated analytically subject to two simplifying assumptions. First, the minority cyclotron resonance does not overlap the $n_{\|}^2 = \mathcal{L}$ cutoff. Second, the process of mode conversion at the $n_{\|}^2 = \mathcal{S}$ resonance layer is ignored.

The first assumption may be quantified by noting that the thickness of the absorption layer is approximately

$$\Delta \sim \frac{k_{\|} v_{thm} R}{\omega},$$

while the separation of the minority cyclotron resonance layer and the $n_{\|}^2 = \mathcal{L}$ cutoff (as calculated by cold-plasma theory) is

$$\delta \sim \frac{R n_m}{n_M}.$$

At sufficiently low minority concentrations,

$$\frac{n_m}{n_M} < \frac{k_{\|} v_{thm}}{\omega} \leq 0.08 \ , \tag{5.3}$$

the two layers are indistinct, the evanescent layer vanishes, and the transmission may be estimated by ignoring the attenuation at the evanescent layer and calculating only the absorption at the resonance layer.

The second assumption can be justified in the case where the evanescent layer is thick, and only a small percentage of the fast wave power is transmitted through; and also in the case when the evanescent layer is thinner than a wavelength of the fast wave. It may not be valid for intermediate cases.

5.2.2 Damping at Absorption Layer

The damping of a wave at an absorption layer was first calculated by Stix [4]; for the fast wave in a two-species plasma in tokamak geometry the fraction of the power T transmitted through the absorption layer is [43]

$$T_1 = e^{-2\eta_A}, \tag{5.4}$$

where the damping decrement

$$2\eta_A = \frac{\pi}{2}\frac{\omega_{pM}}{c}\frac{n_m}{n_M}\frac{Z_m}{Z_M}R\mathcal{P} \tag{5.5}$$

may be recognized as the product of an perpendicular Alfven wavenumber ω/v_A, the thickness Δ of the resonance layer, and $\mathcal{P}$, the polarization of the wave. Since there is no reflection at the resonance layer, the fraction of power absorbed at the resonance layer is

$$A = 1 - T_1 = 1 - e^{-2\eta_A} \tag{5.6}$$

This quantity is referred to as the "single-pass absorption".

$\mathcal{P}$ is calculated from the hot-plasma dielectric tensor to be

$$\mathcal{P} = \left|\frac{E_+}{E_y}\right|^2 = \frac{\left(\frac{\omega}{\omega_{cM}} - 1\right)^2}{1 + \frac{\pi}{4}\left[\frac{\omega_{pm}^2}{\omega_{pM}^2}\frac{\omega}{k_\parallel v_{thm}}\left(1 - \frac{\omega_{cM}^2}{\omega^2}\right)\right]^2}. \tag{5.7}$$

For small [H] in D(H) at 5.4 T, $\mathcal{P}$=1, and for small [^{3}He] in D(^{3}He) at 7.9 T, $\mathcal{P}$=1/9, so that the former scenario has high single-pass absorption and the latter scenario has low single-pass absorption.

5.2.3 Attenuation by Evanescent Layer

Under the two simplifying assumptions above, there is no absorption or dissipation at the evanescent layer and the behavior of the fast wave is described by the Budden tunneling problem (Section 21.15 of [57]). The fraction of power in the transmitted wave is

$$T_2 = e^{-\frac{\pi}{2}k_\infty x}, \tag{5.8}$$

where x is the thickness of the evanescent layer and $k_\infty = \omega/v_a$ is the phase velocity of the fast wave far from the evanescent layer. For two plasmas with the same minority

concentration, one being D(H) at 5.4 T and the other being D(^{3}He) at 7.9 T, the former will have a much thicker resonance layer, namely

$$x = R_0 \frac{2m + m^2}{8 + 28m + 24m^2}, \quad \text{D(H)}$$

where $m = n_H/n_D$. This has the effect of diminishing the importance of mode conversion in D(H) plasmas compared to D(^{3}He) plasmas.

The single-pass transmission is then

$$T = T_1 * T_2 \ .$$

Note that single-pass absorption and transmission do not add up to 1, since some power is reflected from the evanescent layer.

5.2.4 Internal Resonator

At minority concentrations high enough that the resonance and evanescent layers are distinct, the power absorbed at the resonance layer will be enhanced over the single-pass value by the "internal resonator" effect [58][1]. Power reflected by the evanescent layer passes back through the resonance layer, where a fraction given by Equation 5.6 is absorbed, while the remainder continues on to the $n_{\|}^2 = \mathcal{R}$ cutoff on the low-field side, where it is again reflected. The total power absorbed after multiple passes is

$$A_{IR} = A\left(1 + (1 + T_1)\sum_{n=1}^{\infty}(1 - T_2)^n T_1^{2n-1})\right), \tag{5.9}$$

and the total power transmitted after multiple passes is

$$T_{IR} = 1 - A_{IR} = T_2 \sum_{n=1}^{\infty}(1 - T_2)^{n-1} T_1^{2n-1} \ . \tag{5.10}$$

[1] In distinction to [58], the internal resonator is here on the low-field side of the evanescent layer, not the high-field side

For high single-pass absorption scenarios such as D(H), the multiple-pass transmission is not much larger than the single-pass transmission, but the multiple-pass absorption can significantly exceed the single-pass absorption.

5.2.5 Predictions of Theory

According to this theory, the quantities affecting the transmission are the minority concentration n_m/n_M, and the majority density, which enters as $\sqrt{n_M}$. The minority temperature enters only through the wave polarization term. At low minority concentrations the minority temperature does not affect the transmission, which is proportional to $\sqrt{n_M}\, n_m/n_M$. At high minority concentration the transmission should be very small, and scale like $\sqrt{n_M}\, n_M/n_m T_H$.

5.3 Plasma: Minority Concentration Scans

The fields at the inner wall appear to be sensitive to the Hydrogen concentration during D(H) heating at 5.4 T, but not to the Helium-3 concentration during D(^{3}He) heating at 7.9 T.

5.3.1 Data from D(H) at 5.4 T

A 31-shot scan of the minority concentration was conducted with D(H) plasmas on 18 and 19 February, 1998. These were 1 MA plasmas, with target densities in the vicinity of $nl_{04} = 9 \times 10^{19}\ m^{-2}$ before H-Mode,[2] corresponding to a central electron density $n_e(0) = 1.5 \times 10^{20}\ m^{-3}$. All shots in this scan went into H-mode. Experimentally measured density and temperature profiles are shown in Figure 5.3, along with a model profiles, of the form

$$X = X(r=a) + (X(0) - X(r=a))(1 - (r/a)^{\alpha})^{\beta}\ ,$$

[2]The experimentally measured quantity nl_{04} is the line-integrated electron density following a vertical chord through the plasma center, derived from the TCI. This signal is used to provide feedback for the gas puffing, allowing a target electron density to be maintained.

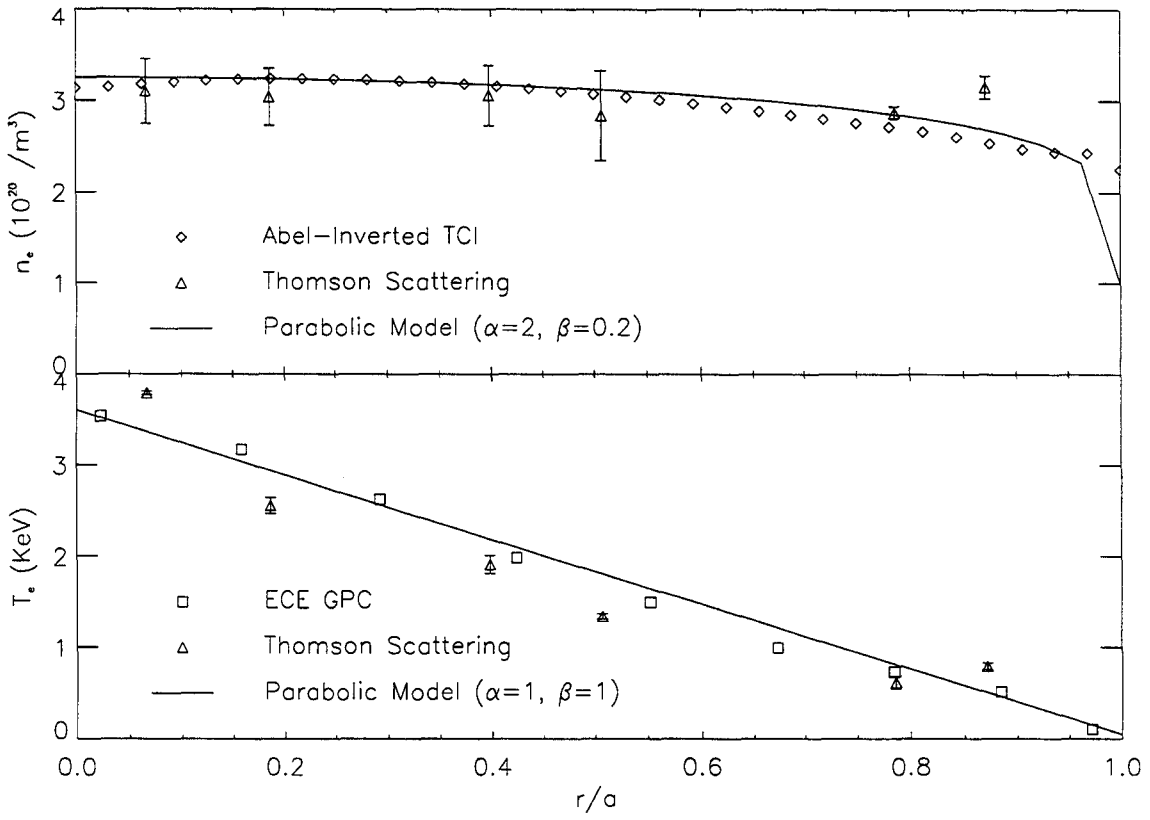

Figure 5.3: H-mode Density and Temperature Profiles

used as inputs to the code FELICE (see below). The inner and outer gaps were held constant during this scan. The RF power was greater than 1 MW for more than 400 ms for each of these shots, although the antennas were often beset with trips.

Transmission

Data from this scan is plotted in red in Figure 5.4. The abscissa [H] is the best estimate of $n_H/(n_H + n_D)$ available from the charge-exchange diagnostic. This estimate is the average of the values of [H] measured immediately before RF turn-on and immediately after RF turn-off, since the neutral particle flux during RF heating cannot be used to determine the percentage of Hydrogen in the bulk plasma [59]. The ordinate is T_{IW} from one of the inner wall loops, averaged over the times when the net RF power is larger than 100 kW, and the error bars are the RMS variation with time. T_{IW} has been multiplied by the factor 3.75×10^6 to make it quantitatively similar

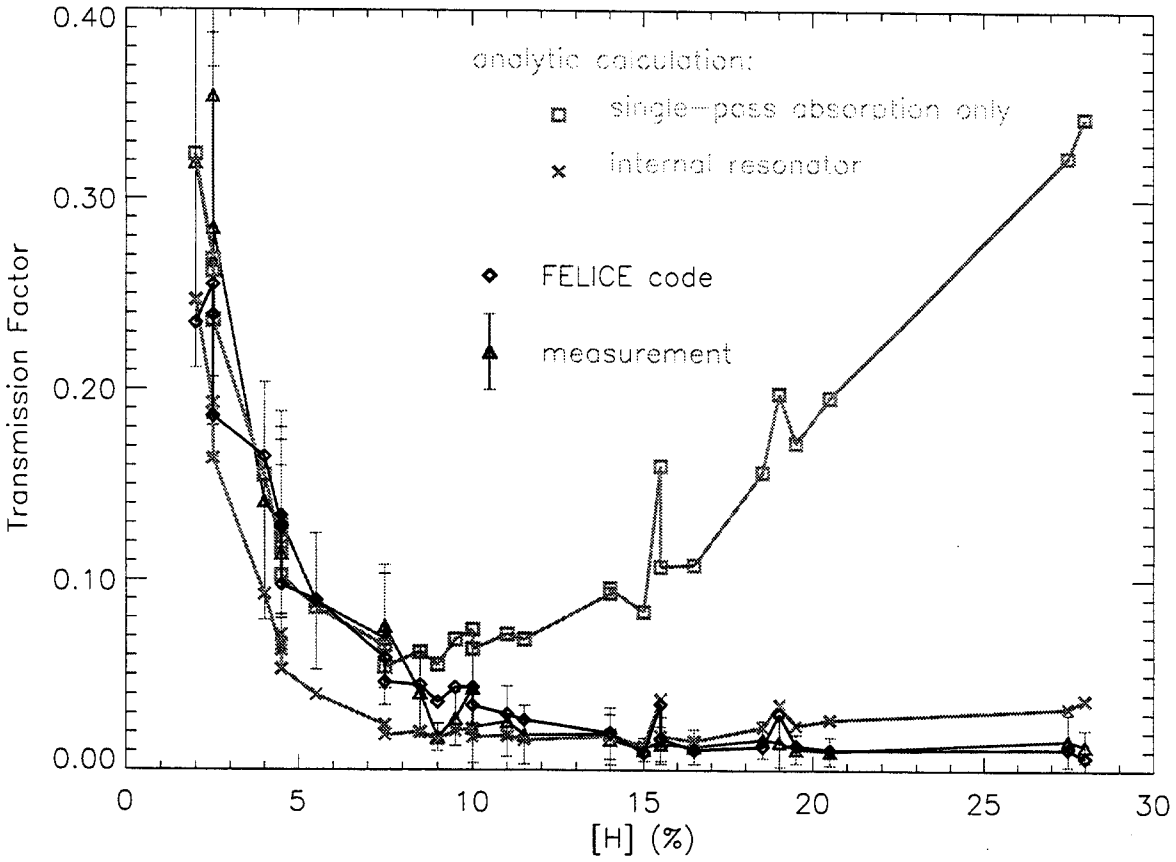

Figure 5.4: Transmission factor during [H] scan in D(H) at 5.4 T

to the predictions of theory and code; this empircally determined factor includes the evanescence of the fast wave outside the $n_{\|}^2 = \mathcal{R}$ layer (at both the high- and low-field edges of the plasma), the attenuation of the field by the tiles in front of the probes, and accounts for the effect of wave focussing and the toroidal nonuniformity of the wave fields.

The theoretically predicted transmission factors are plotted in green on Figure 5.4. The squares represent T_1, the power transmitted neglecting the evanescence layer, calculated by Equation 5.4. The single-pass absorption can be read off from this curve as $A = 1 - T_1$. Each data point corresponds to a plasma shot, so that the ratio n_H/n_D is computed from data from the charge-exchange diagnostic, and ω_{pD} uses this and

the Abel Inversion of the TCI measurement of the line- integrated electron density, suitably averaged over time, under the assumption of quasi-neutrality. The crosses represent T_{IR}, the power transmitted in the internal resonator model, calculated by Equation 5.10. Only the first two terms of the sum contribute significantly. Both curves assume $k_{||} = 15$ m^{-1} and minority temperature $T_H = 100$ KeV.

The measurement and calculation may finally be compared to the results of the full-wave code FELICE [60], specifically the quantity called "power radiated in the fast wave", which is plotted in blue in Figure 5.4. FELICE is a full-wave code in slab geometry, which evolves multiple toroidal and poloidal modes established as initial conditions by the current distribution in the antenna current straps. The code was run with outward radiating boundary conditions, corresponding to no reflected wave at the $n_{||}^2 = \mathcal{R}$ cutoff at the high-field side, for each of the 31 shots of the [H] concentration scan. This choice of boundary conditions allows the inclusion of the internal resonator on the low-field side. Where possible the input parameters were taken from measurement, thus: central electron density (Abel-inverted TCI measurement); n_H/n_D (charge exchange); central electron temperature (grating polychromator); central deuterium temperature (neutron detector, assuming n_H/n_D as estimated from CX); edge electron density and temperature (estimated from typical FSP data); outer gap (EFIT reconstruction); electron density and temperature profiles shown in Figure 5.3. A value of 100 keV was assumed for the minority temperature.

FELICE shows good agreement with the data for the entire range of minority concentrations. At low concentrations $n_H/n_D < 0.08$, the single-pass, non-evanescent calculation agrees very closely with FELICE and the data. At high-concentrations $n_H/n_D > 0.11$, the internal resonator model closely matches the data. This implies that the evanescent layer separates from the absorption layer over the concentration range $0.08 < n_H/n_D < 0.11$. Using $n_H/n_D = 0.08$ in Equation 5.3 gives an estimate $T_H = 100$ KeV.

Effect of Minority Temperature Varying the minority temperature in the analytic calculation (Equations 5.4 and 5.10) had a large effect on the transmission,

as shown in Figure 5.5. Comparing these results with Figure 5.4, the best agree-

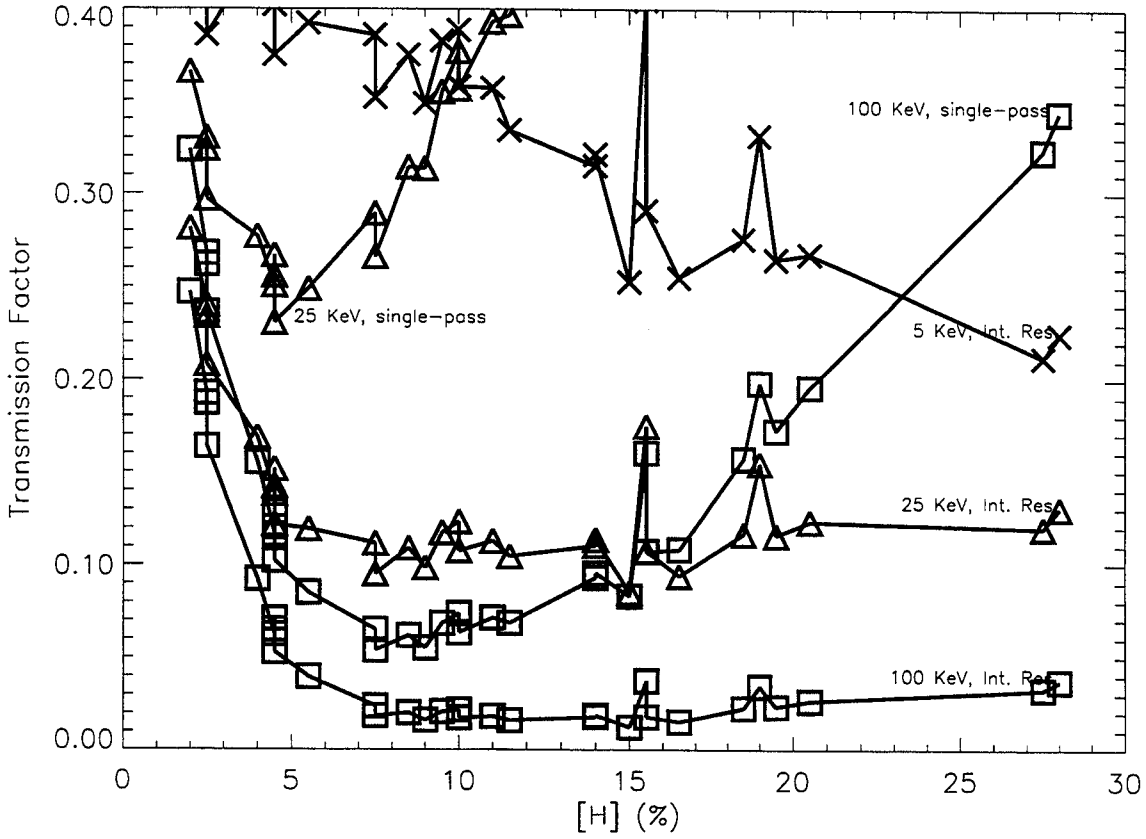

Figure 5.5: T_H Scan of Analytic Transmission Factor

ment is obtained for $T_H = 100$ KeV. Decreasing T_H leads to increased transmission. The internal resonator calculation (Equation 5.10) gives less transmission than the single-pass calculation (Equation 5.4) for all values of T_H.

In Figure 5.6 are shown complimentary results from the full wave code FELICE. Varying T_H with other parameters fixed did not greatly affect FELICE's output. At low minority temperatures ($T_H = 5$ KeV) FELICE seems to be more susceptible to eigenmodes (spikes on plot). The agreement between FELICE and the data is equally good whether $T_H = 100$ KeV or $T_H = 25$ KeV is used in FELICE. It is unclear why the quantitative results shown in Figures 5.5 and 5.6 are different.

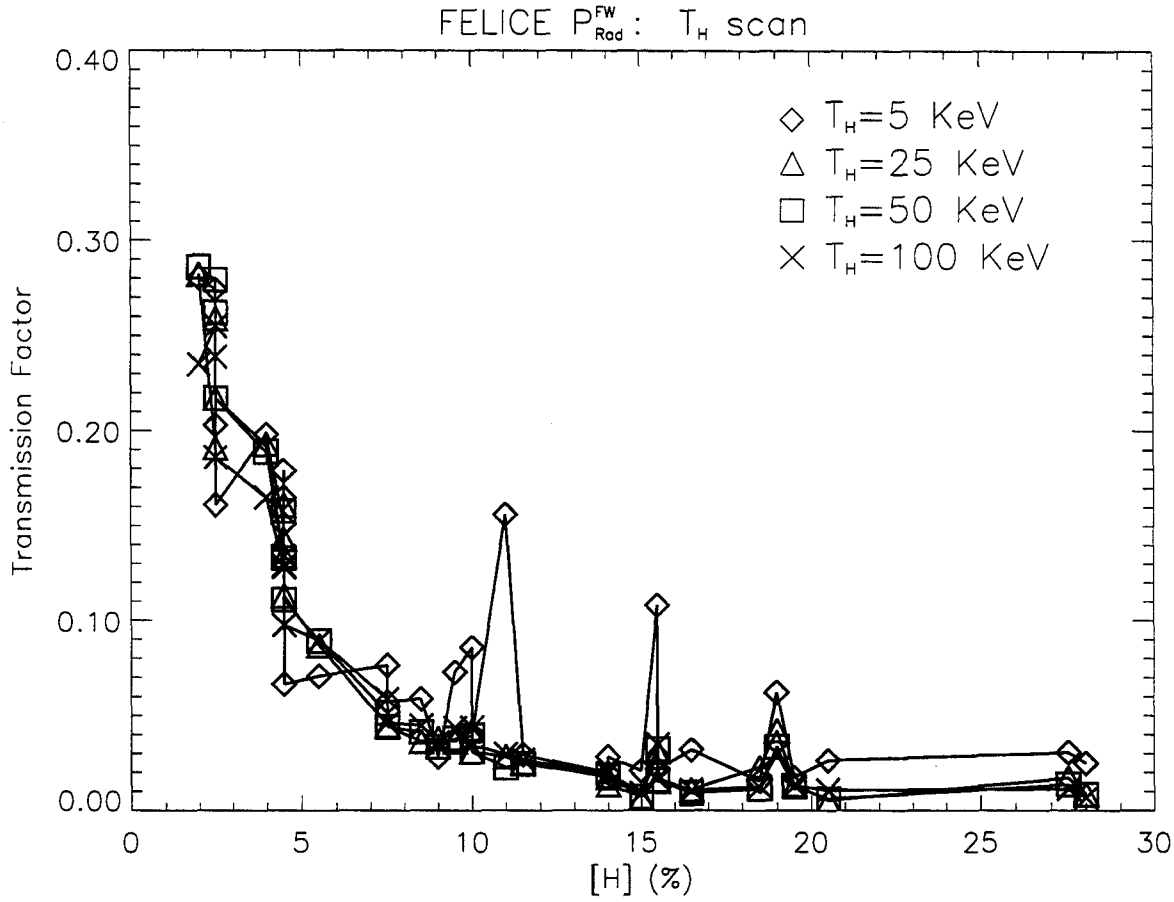

Figure 5.6: T_H Scan of FELICE Transmission Factor

Absorption

The minority concentration scans which provided most of the data in this chapter were proposed and carried out under the leadership of Dr. Stephen Wukitch. One of the goals of the scans was to find the optimum minority concentration for plasma heating. The fraction of RF power absorbed by the plasma was calculated by Dr. Wukitch using the break-in-slope of the stored energy at RF turn-off [55]. Figure 5.7 shows the absorbed power fraction calculated from the data, the absorbed power fraction predicted by single-pass theory (Equation 5.6), and the absorbed power fraction predicted by Equation 5.9, which the includes the effect of the internal resonator, assuming temperatures of 10 Kev and 100 KeV. The break-in-slope analysis tends to

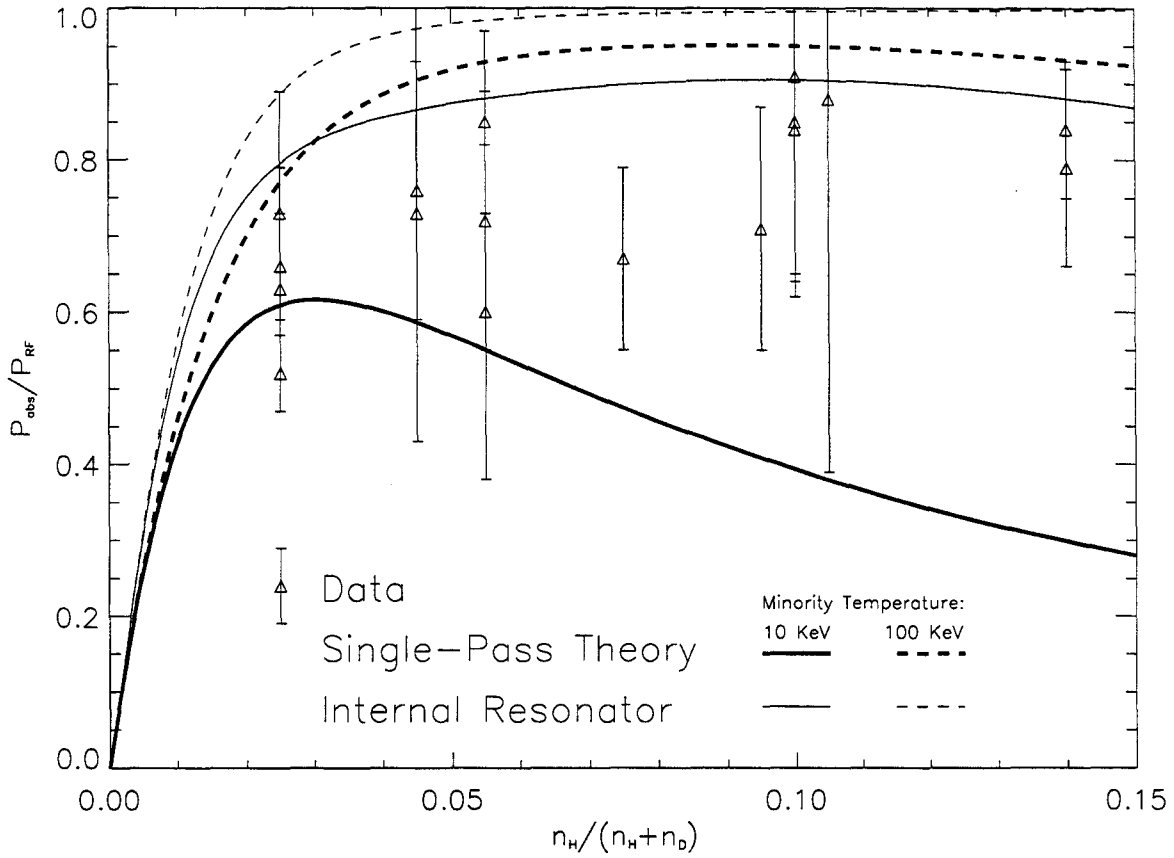

Figure 5.7: Absorbed power fraction as a function of [H]

underestimate the absorbed power fraction, so the comparison of theory to absorption thus calculated is less trustworthy than the comparison of theory to transmission measurements. Nonetheless, it is prudent to infer from these measurements that the minority temperature lies in the range 10 KeV $< T_H <$ 100 KeV.

Minority Tail Temperature

Stix [56] gives a simple estimate of the minority tail temperature:

$$T_{Tail} = T_e + \frac{P}{3n_H}\tau_s. \tag{5.11}$$

Here P is the power density flowing into the minority, and τ_s is the slowing down time of minority ions. For energies higher than the critical energy W_c,

$$W_c = 14.8AT_e\left\langle\frac{Z_i^2}{A_i}\right\rangle^{2/3}, \tag{5.12}$$

the minority ions slow down more on electrons than on ions; vice-versa for lower energies. Here

$$\left\langle\frac{Z_i^2}{A_i}\right\rangle = \frac{\sum_i n_i(Z_i^2/A_i)\log\Lambda_i}{n_e\log\Lambda_e}. \tag{5.13}$$

Taking $\log\Lambda_e = \log\Lambda_i$ gives $W_c \sim 15T_e$.

Assume $T_{tail} > W_c \sim 50$ KeV, so that the tail slows down on electrons. The slowing down time for minority ions on electrons is

$$\tau_s^{H/e} = \frac{6.32\times10^{14}AT_e^{3/2}}{n_eZ^2\log\Lambda_{He}} \text{ seconds}, \tag{5.14}$$

when T_e is in eV, and n_e is in m^{-3}. Taking $\log\Lambda_{He} \sim 15$, A=1; and $T_e \sim 3KeV$, and $n_e \sim 3\times10^{20}$ (parameters suitable for C-Mod H-mode), gives

$$\tau_s^{H/e} = 0.02\ s. \tag{5.15}$$

The power density P flowing into the minority is estimated as $P = P_{abs}/V_{abs}$, where P_{abs} is the power absorbed by the minority and V_{abs} is the volume over which power is absorbed. In those cases where the measured absorbed power fraction (Figure 5.7) is greater than 80 %, P_{abs} is known to within 10 %, since it cannot be any lower than measured by the break-in-slope analysis, and cannot be any higher than the forward power leaving the antenna. V_{abs} is less well diagnosed. If the power is assumed to be absorbed within $r/a < 0.3$, then $V_{abs} \sim 0.1$ m^{-3}. Using $P_{RF} = 2$ MW, an absorption efficiency of 90 %, and a Deuterium density $n_D = 3\times10^{20}$ m^{-3} gives an estimate of

minority temperature:

$$T_{tail} = T_e + \frac{3KeV}{n_H/n_D}. \tag{5.16}$$

This estimate of T_{tail} neglects all transport processes and ion orbit losses, and therefore overestimates the true T_{tail} by an unknown amount. However, it is consistent with T_{tail} obtained using the FPPRF Fokker- Planck code [61] for Alcator C-Mod H-mode discharges [62]. For these discharges $T_{tail} \sim 40$ KeV was obtained for $n_H/n_D = 0.08$ [63]. Thus the temperature $T_H = 100$ KeV required by the analytic calculations (Equations 5.4 and 5.10) for agreement with the data cannot be accounted for by independent calculations of T_{tail}.

5.3.2 Data from D(^{3}He) at 7.9 T

A 19-shot scan of the minority concentration was conducted with D(^{3}He) plasmas on 980212. These were 1.2 MA plasmas, with target densities again in the vicinity of $nl_{04} = 9 \times 10^{19} m^{-2}$ ($n_e(0) = 1.5 \times 10^{20} m^{-3}$). H-modes were much weaker and lasted less time than the H-modes occuring during the [H] scan in D(H) described above. The transmission factor calculated from the data (with the same normalizing factor), the analytic single-pass calculation, and the FELICE output for this scan are plotted in Figure 5.8.

The single-pass analytic calculation and the code agree at low minority concentrations but not at high minority concentrations, while no dependence of the measurement on the minority concentration is evident. The measurement thus agrees with neither the analytic calculation nor the code. The wave fields measured by the inner wall loop probe are higher in this heating scenario than they are during D(H) at 5.4 T, in qualitative agreement with the weaker single-pass absorption of this scenario.

5.3.3 Discussion

The analysis presented in Section 5.2 follows a slab model, and does not include loss mechanisms such as edge heating, joule heating of first-wall surfaces, and sheaths.

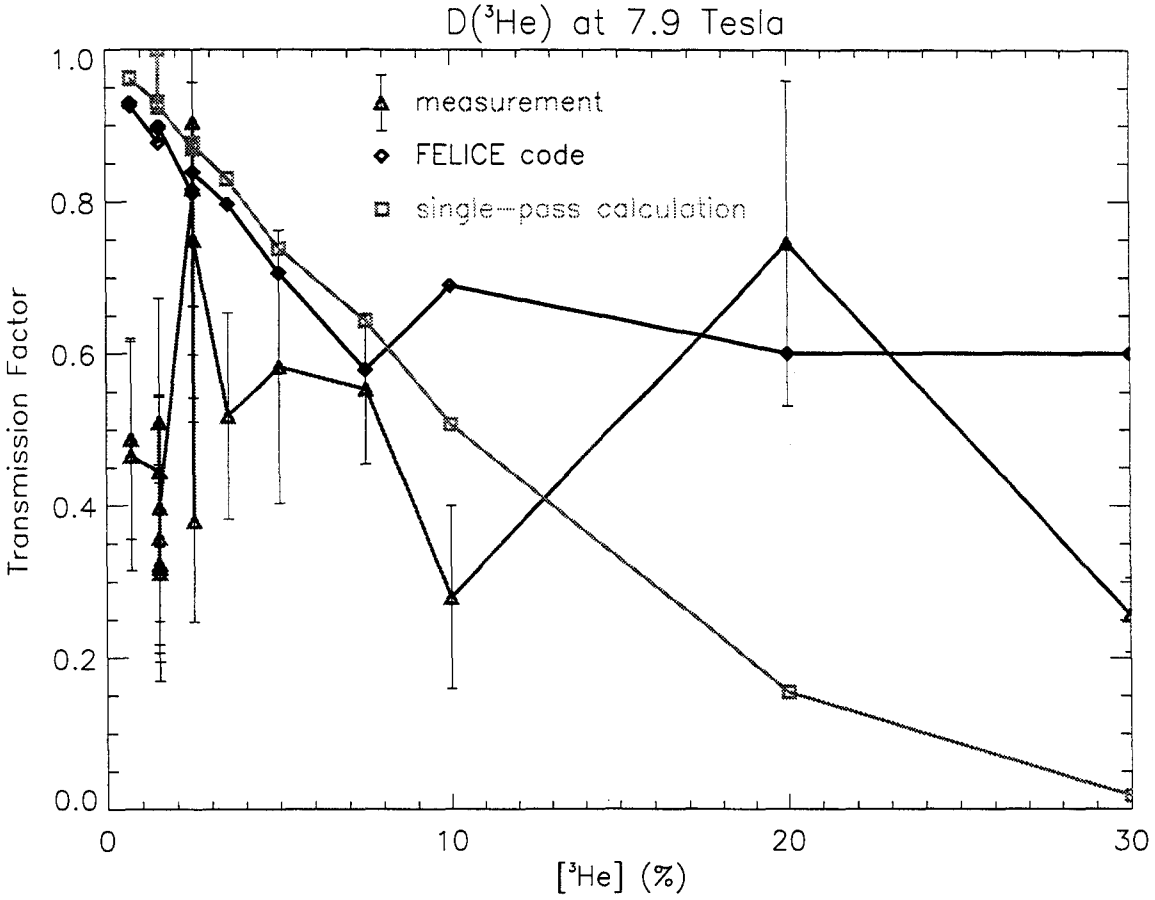

Figure 5.8: Transmission factor during $[^3He]$ scan in D(^3He) at 7.9 T

This neglect is justified, in the case of D(H), by the qualitative agreement with the data: if the single-pass absorption is high, then the energy the wave loses to sheaths, etc. is negligible. Furthermore the wave does not spread out in the toroidal direction. If the single-pass absorption is low, the wave may spread significantly in the toroidal direction, may interfere with itself to form cavity modes or toroidal eigenmodes, may lose significant energy to sheaths, and so on. In the low single-pass absorption case the toroidal extent of the wave may be measured by encircling the central column of the tokamak with an array of loop probes (such an array has not yet been installed on C-Mod, and hence no relevant data could be taken).

5.4 Sawtooth modulation of Loop probe signals

During RF heating of D(H) plasmas at 5.4 T, the signals from the inner wall loop probes commonly show modulation which follows the timing of the sawtooth instability, seen on T_e measured by the Grating Polychromator (GPC) and other diagnostics. The sense of this modulation depends on the Hydrogen concentration. At low Hydrogen concentrations, the sense of the sawtooth modulation on the loop probes is opposite ("inverse") the sawtooth modulation on the central GPC channel (Figure 5.9, data from a shot with $n_H/n_e \sim 2.5\%$). At high Hydrogen concentrations, the two signals show modulations with the same sense (Figure 5.10, $n_H/n_e \sim 19.5\%$). For both of these concentrations, the absorption and evanescent layers lie inside of the sawtooth mixing radius (r/a=0.5). The locations of the $n_{||}^2 = \mathcal{R}$, $\mathcal{L}$, $\mathcal{S}$ surfaces are shown in Figures 5.11 and 5.12. During D(^{3}He) heating at 7.9 T, sawtooth modulation is only seen at high [^{3}He], but both senses are sometimes present simultaneously on different probe signals.

Sawtooth modulation is also frequently seen on the signals from the directional couplers in the RF antenna transmission line and from the current probes behind the antenna current straps. Sawteeth of both senses may be seen simultaneously in these signals; for example, inverse sawteeth may be seen in the forward and reflected power from one antenna while sawteeth are seen on the forward and reflected power from the other antenna. The sawtooth crash can cause the loading resistance to change by as much as a factor of two in 0.1 ms (Figure 5.13).

There is no apparent correlation between the observation of sawteeth in these datasets (ie, in the power going into the plasma) and the observation of sawteeth in the IW loop probe signal (the power coming out the other side of the plasma).

5.4.1 Timing of IW Sawteeth

The effect of a sawtooth crash takes a measurable amount of time to propagate out to the plasma edge. Comparison of the timing of the IW loop probe signal crash and the T_e crash at various radii implies the path the RF power took to get to the probe:

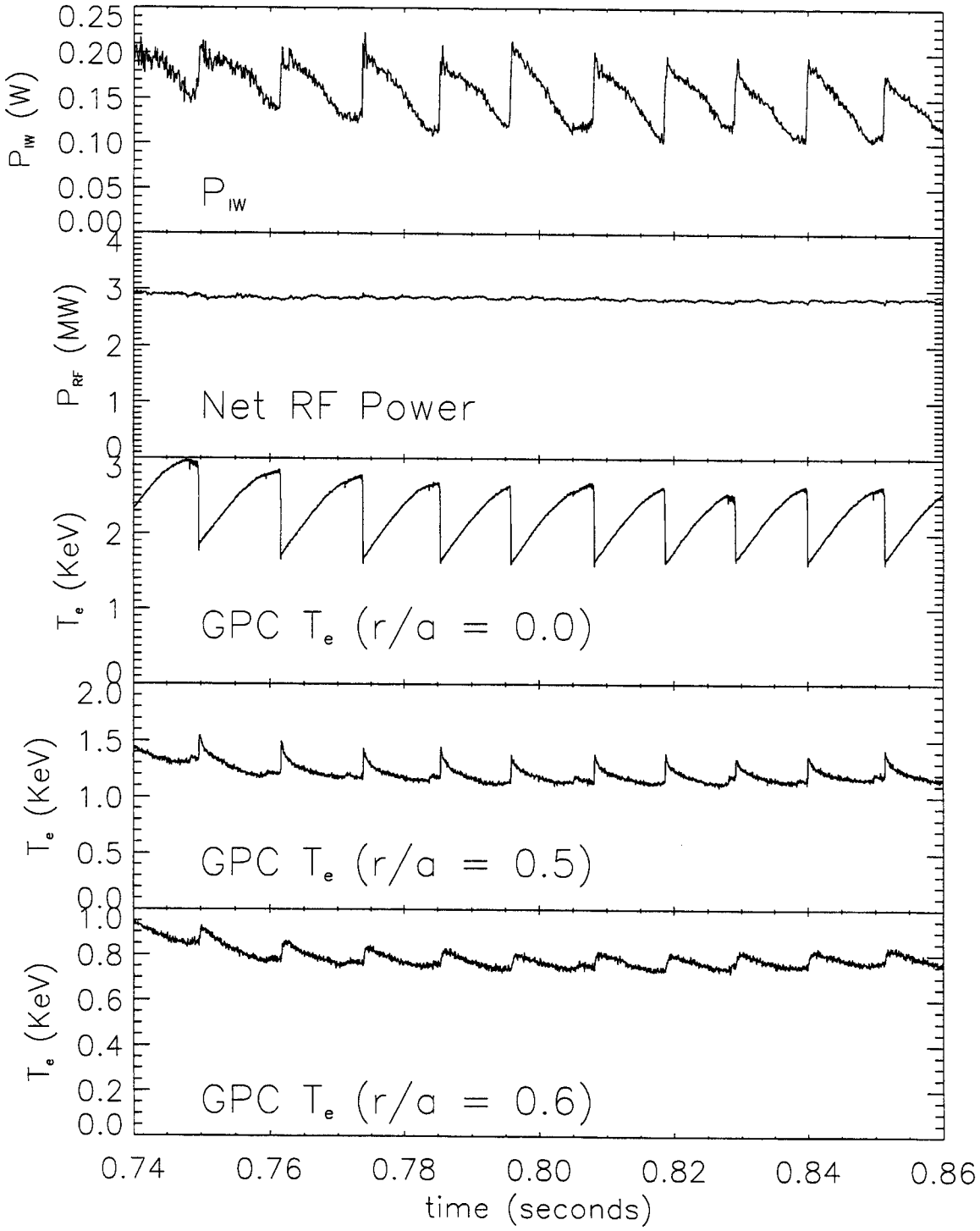

Figure 5.9: Inverse Sawteeth on Probe Signal (P_{IW}) at Low [H]

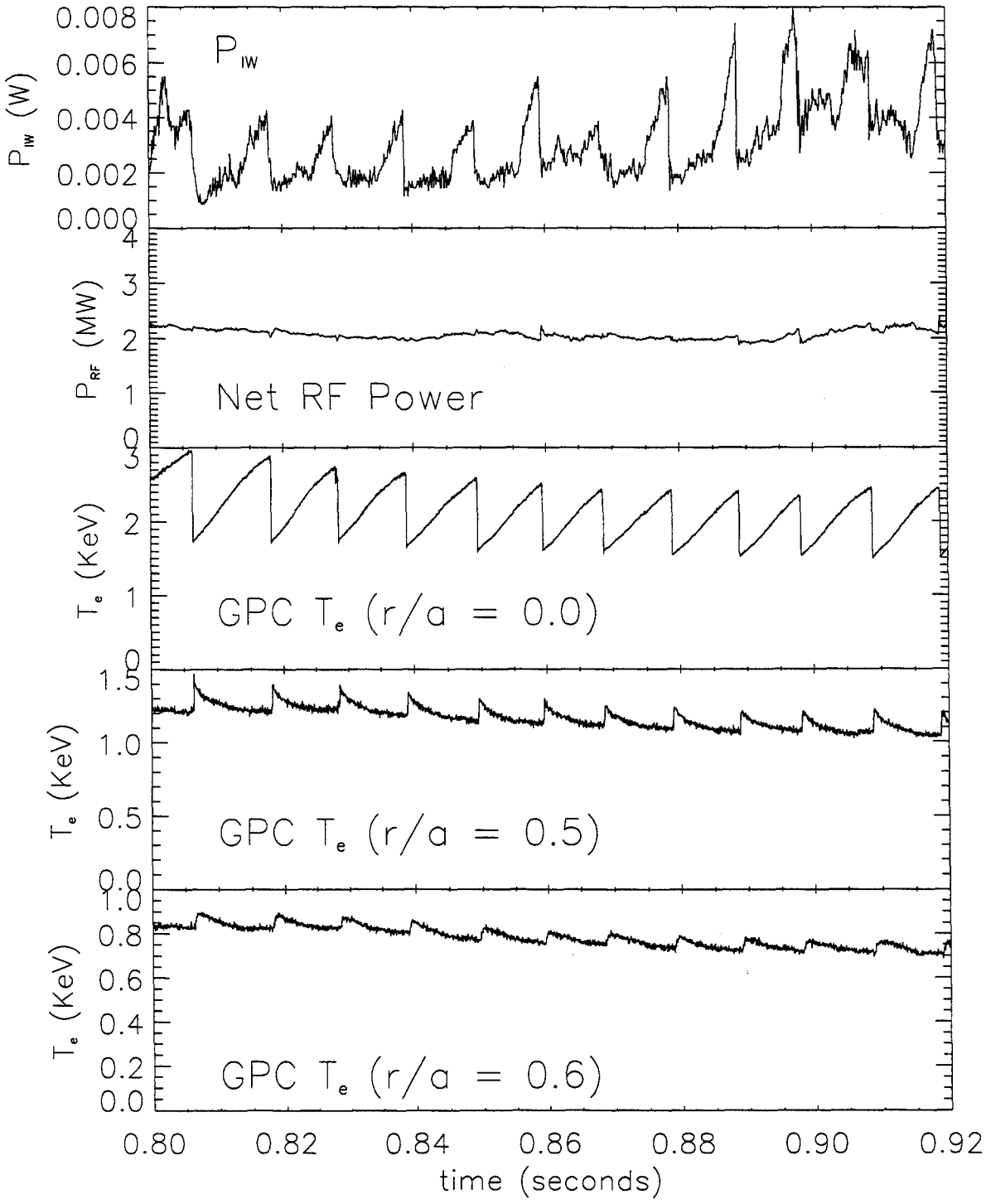

Figure 5.10: Sawteeth on Probe Signal (P_{IW}) at High [H]

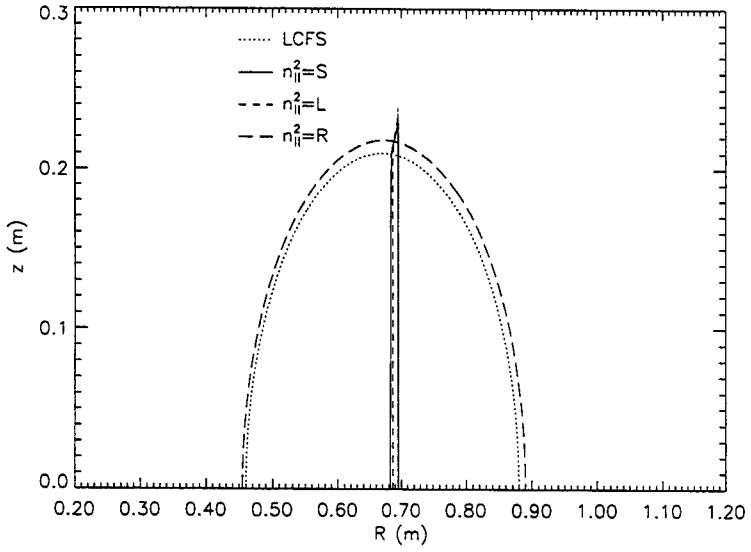

Figure 5.11: Stix Parameter Surfaces for n_H/n_D =.025

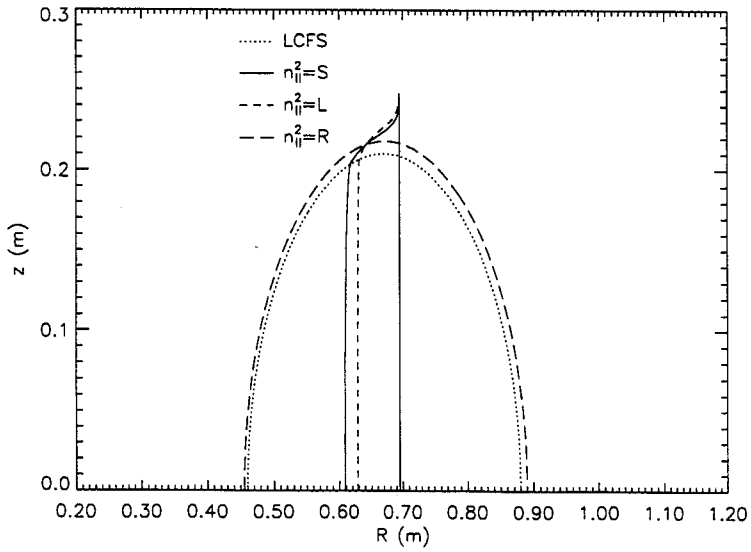

Figure 5.12: Stix Parameter Surfaces for n_H/n_D =.195

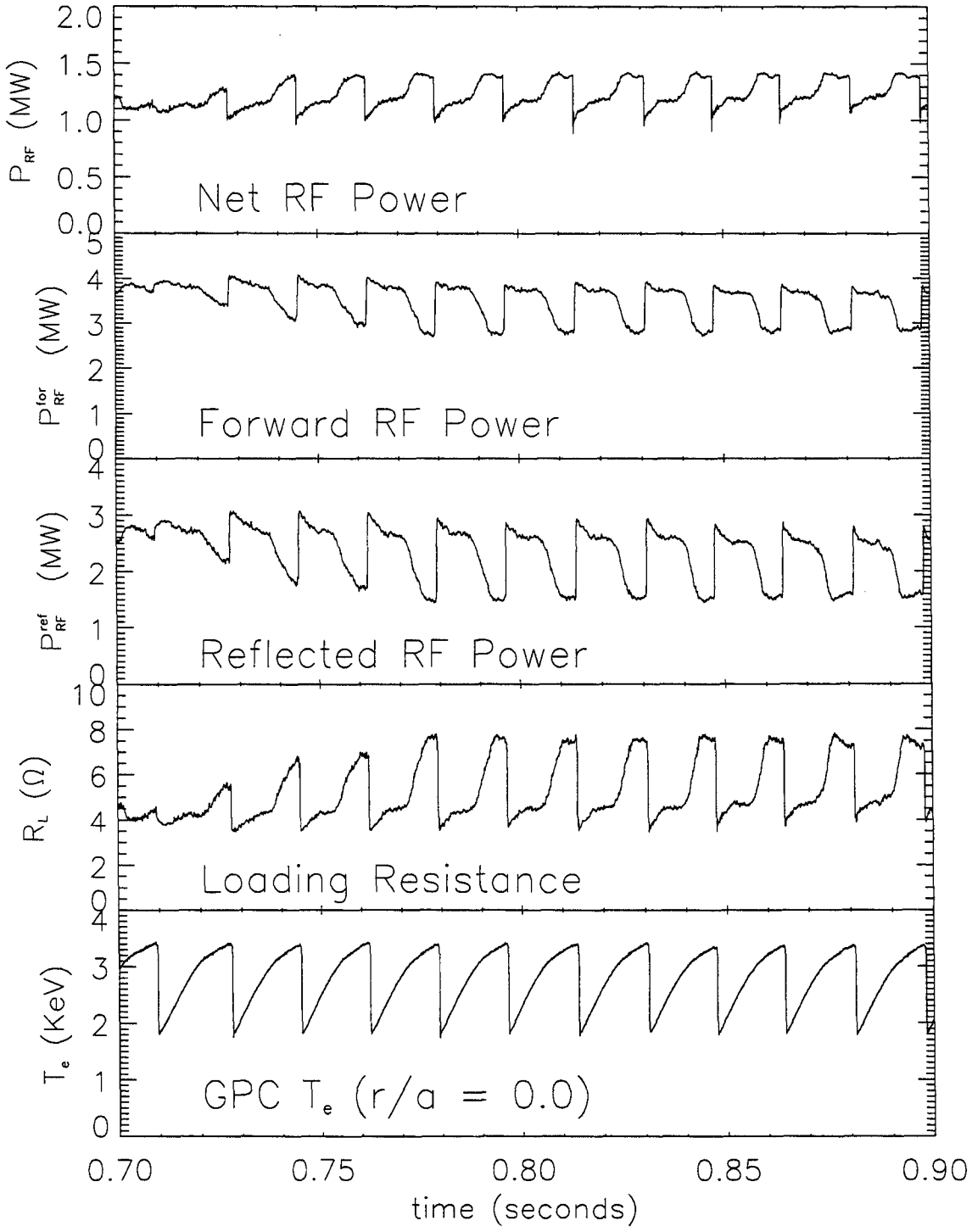

Figure 5.13: Sawteeth on Antenna Diagnostic Signals

if the IW loop probe signal crash is synchronous with a central T_e crash, then the RF power passed through the center; if instead the IW loop probe signal is synchronous with an edge T_e channel then the RF power did not pass through the center.

Returning to Figure 5.9, the three channels of GPC data (third through fifth traces), describing T_e at three minor radii, illustrate typical sawtooth behavior. The sawtooth crashes on the central GPC channel (third trace) and the inverse sawteeth on the channel at r/a=0.5 happen nearly simultaneously, with the inverse sawteeth being much smaller than the sawteeth. The inverse sawteeth on the channel at r/a=0.6 are smaller still, and do not rise as quickly as the inverse sawteeth at r/a=0.5. Which channel has the closest time history to the signal from the inner wall loops?

A computer program was written to find sawtooth crashes. The time of the sawtooth crash was identified as the time of the maximum magnitude of dT_e/dt. This program was run on the central GPC channel to establish reference times for the crashes. The program was then run on the other GPC channels and on the IW loop signals, for all of the shots in the [H] scan for which there was GPC data (28 shots total), and the relative timing calculated. A histogram of the relative timing is shown in Figure 5.14. The program did not find all sawtooth crashes on these signals that were apparent to the eye. The statistics are summarized in Table 5.1. As can be seen, the maximum magnitude of dT_e/dt occurs simultaneously at r/a=0.0

Signal	N	Mean Delay Time (ms)	Standard Deviation (ms)
GPC (r/a=.4)	278	-.02	.04
GPC (r/a=.5)	434	.04	.02
GPC (r/a=.6)	27	.09	.15
IW Loop	254	-.01	.11

Table 5.1: Sawtooth Crash Delay Statistics

and r/a=0.4, then 0.05 ms later at r/a=0.5 and 0.1 ms later at r/a=0.6 (the GPC digitization frequency is 20 kHz). At this rate of propogation, the heat pulse would reach the plasma edge 0.2 ms after the central crash (although it is rarely visible past r/a=0.6). Fewer "crashes" were identified of the GPC channel at r/a=0.4 than of the GPC channel at r/a=0.5 because the former channel is close to the T_e *inversion*

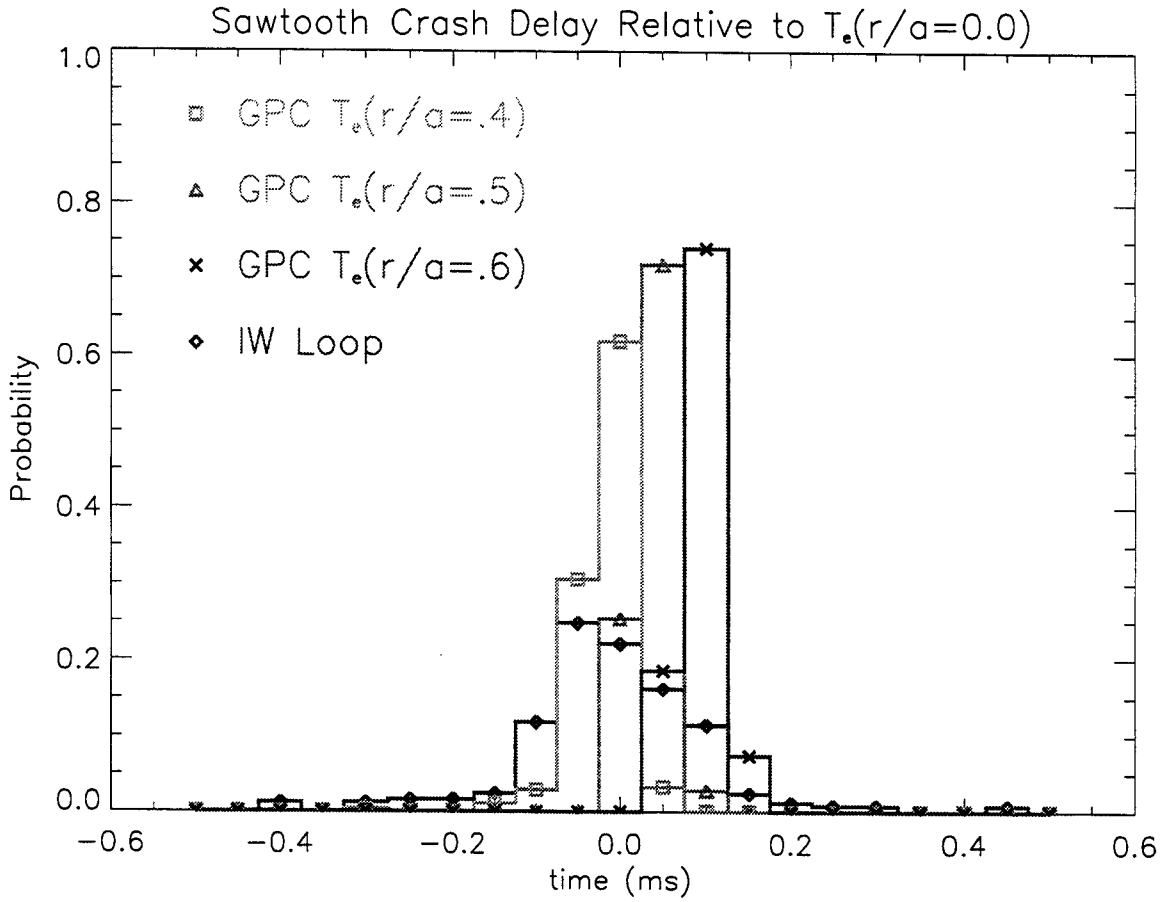

Figure 5.14: Histogram of Sawtooth Delay

radius, at which T_e remains constant during a sawtooth crash. Fewer still crashes of the GPC channel at r/a=0.6 were found, because even by this radius diffusion has greatly reduced dT_e/dt. No crashes were identified on GPC channels outside r/a=0.6.

Figure 5.14 includes data from all values of n_H/n_D. Figure 5.15 includes data from only those shots with $n_H/n_D > 0.12$, the high concentration shots, for which clear sawteeth were seen on the IW loop signal. On the other hand, Figure 5.16 includes data from only those shots with $n_H/n_D < 0.08$, the low concentration shots, for which clear inverse sawteeth were seen on the IW loop signal. There is no apparent difference between the two populations of data.

The timing of the IW loop crashes is closest to the GPC channel at r/a=0.0, and the IW loop crash precedes the crash of the GPC channel at r/a=0.6. The timing and number of identified crashes is inconsistent with the hypothesis that the RF power did not penetrate to the r/a=0.5 surfce. This rules out guided propogation along the plasma surface.

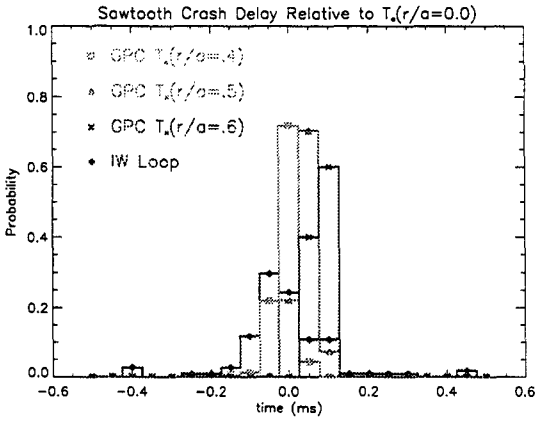

Figure 5.15: $\frac{n_H}{n_D} > 0.12$

As a side comment, it appears from this study that the GPC channel at r/a=0.4 actually jumps before the central GPC channel crashes. There are some shots on which this is obvious. It is plausible that the instability is triggered at the q=1 surface, which is generally near the inversion radius, and that therefore the GPC channels closest to the inversion radius should be the first to change.

5.4.2 Dependence of IW sawteeth on [H]

The magnitude and sign of the IW loop crash were found to depend on the minority concentration, as shown in Figure 5.17. The ordinate describes the magnitude of the T_{IW} crash, measured as percentage change in T_{IW}, averaged over a shot. T_{IW} features inverse sawteeth at low minority concentrations and ordinary sawteeth (the same sense as the GPC central channel) at high minority concentrations. T_{IW} itself is largest at low minority concentrations (as shown in

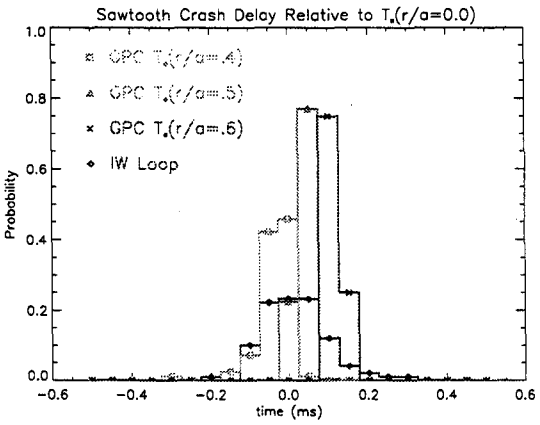

Figure 5.16: $\frac{n_H}{n_D} < 0.08$

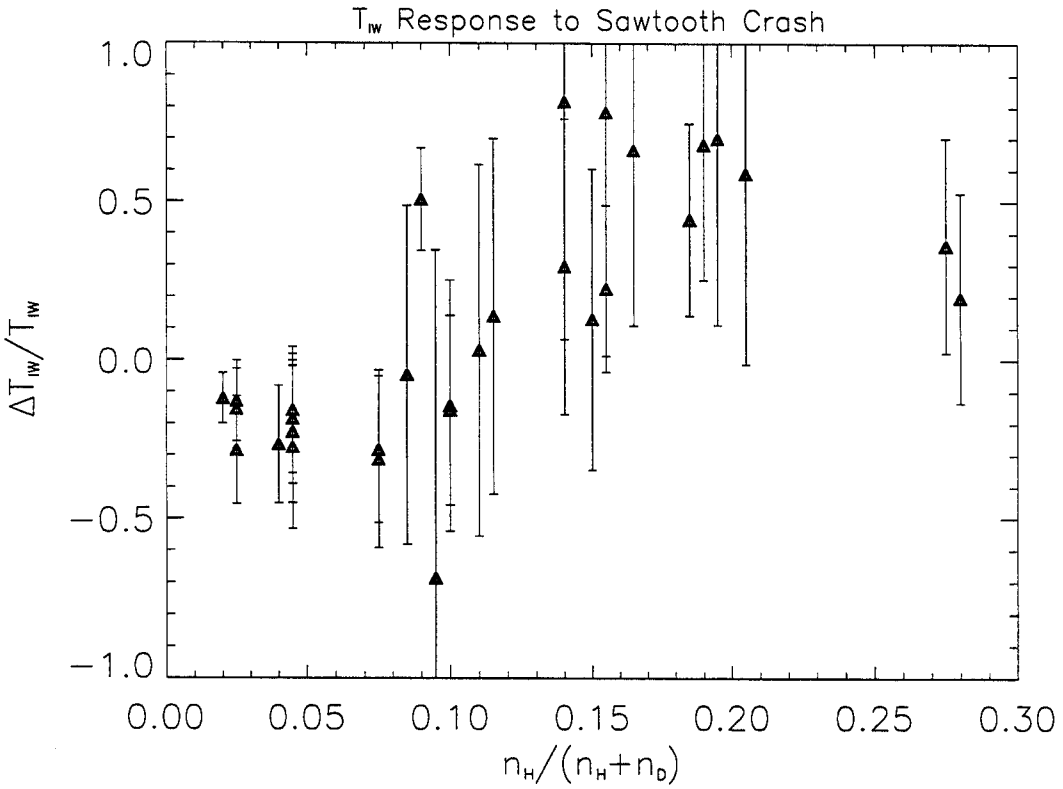

Figure 5.17: Dependence of IW sawteeth on [H]

Figure 5.4).

5.4.3 Observation of IW sawteeth in D[^{3}He]

The sawtooth modulation is not as prominent during D(^{3}He) heating at 7.9 T as it is during D(H) heating at 5.4 T. It is largest at the highest ^{3}He concentrations run to date ($n_{He}/(n_D + n_H) \geq 0.2$), a total of five shots. On three of these shots, sawtooth modulation was observed on one IW loop probe while inverse sawtooth modulation was observed on another. The cause of this phenomenon has not been understood.

5.5 Measurements of n_D during Sawteeth

Sawtooth modulation of n_e has been inferred on TEXT [64], using Abel inversions of integrated chord densities measured by an interferometer, and Alcator C [65], on the

visible continuum (which is dominated by brehmsstrahlung). The density sawteeth seen on TEXT were as big as $\Delta n_e/n_e \leq 0.1$, roughly the same size as the temperature sawteeth, while the density sawteeth inferred on Alcator C were somewhat smaller, $\Delta n_e/n_e \sim 0.06$, as compared to a sawooth modulation of T_e of more than 15%. On Alcator C-Mod, the TCI line-integrated chord densities show sawteeth only on rare occassions, such as after pellet injections, presumably when the density profile is exceptionally peaked. Therefore data from the Thomson Scattering (TS) system was analyzed for the presence of density sawteeth at the same times as RF diagnostic data showed sawteeth. While the TS sampling rate is only 30 measurements per second, the sampling window is much less than 1 ms, so that aliased sawteeth are apparent on the T_e measurement: if the TS data point is taken just before a sawtooth crash, the temperature is high; if the TS data point is taken just after a sawtooth crash, the temperature is low (the ECE measurement is assumed to be the "true" temperature).

A shot was chosen (980218004, $n_H/n_D = 0.025$) during which consistent sawtooth modulation was seen on the inner-wall probes' signals, of amplitude $\Delta P_{st}/P_{IW} \sim 0.5$. Two successive TS points were chosen, the earlier 0.5 ms after a sawtooth crash, the later 5 ms before a sawtooth crash (the sawtooth period at this time was $\tau_{st} \sim 13$ms. n_e TS profiles and simultaneous GPC T_e profiles before and after a sawtooth crash are shown in Figure 5.18. The sawtooth modulation of T_e is more than 25%, while the sawtooth modulation of n_e can be no more than the relative calibration error of the TS density measurement, which is estimated at 10% [66].

The transmission factors for these two times are $T = 0.11$ (just before crash), and $T = 0.19$ (just after crash), a variation $\Delta T_{st}/T_{av} \sim 0.5$, corresponding to a variation in damping decrement $\Delta\eta_{st}/\eta_{av} \sim 0.3$. This variation is too large to be accounted for by the observed sawtooth modulation on n_e, if one assumes that n_H/n_D is a constant during the sawtooth cycle. However, the variation in $\eta \propto \sqrt{n_D} n_H/n_D$ can be accounted for by postulating a reasonable variation in n_H/n_D during the sawtooth cycle as discussed in the next section.

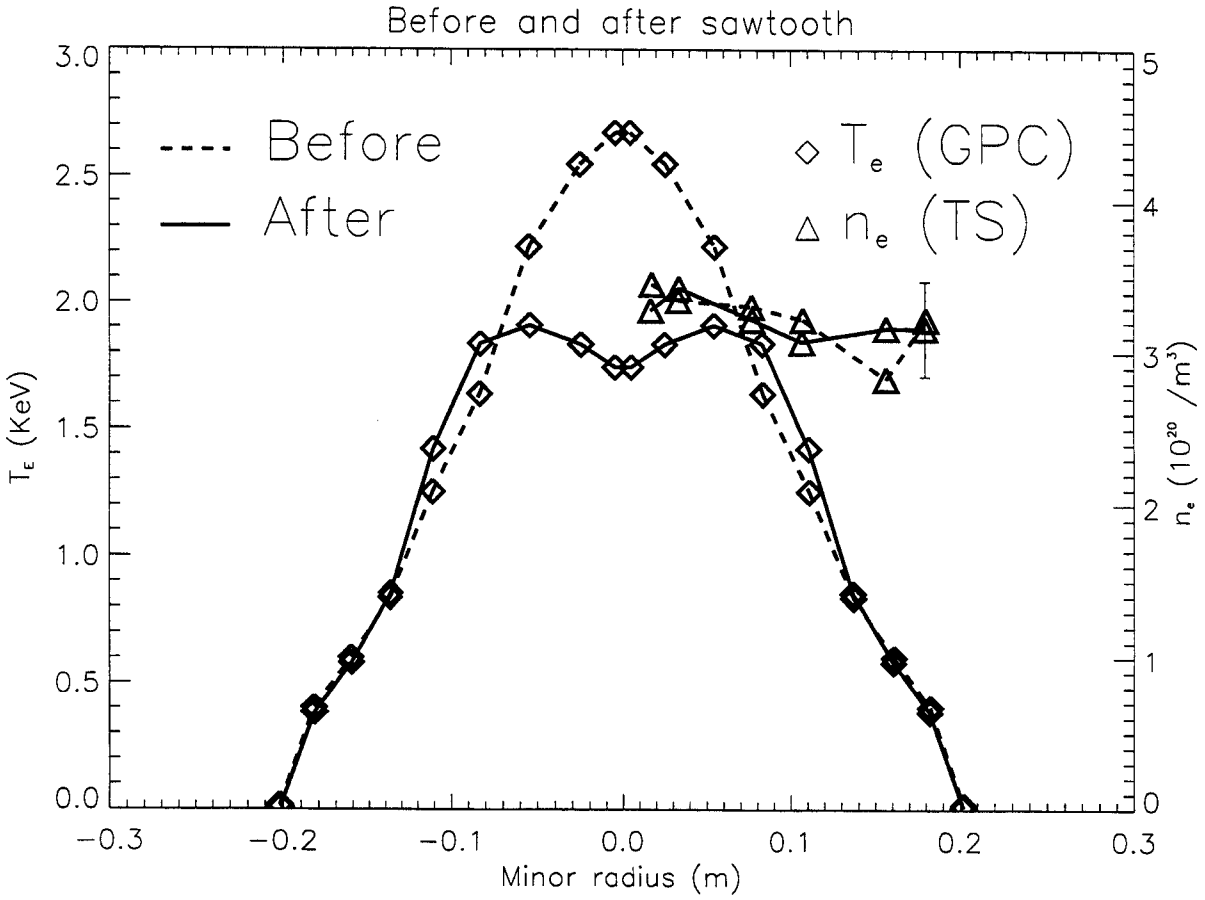

Figure 5.18: n_e and T_e profiles

5.6 Fast-wave polarization

For small [H], the fast wave polarization $\mathcal{P} = 1$, and the damping decrement varies like

$$2\eta_A \propto \frac{n_m}{n_M} ,$$

so that if the minority concentration decreases at a sawtooth crash, the transmission fraction increases, as has been described in the previous section. At large [H], $\mathcal{P} \ll 1$,

and the damping decrement goes like

$$2\eta_A \propto \frac{n_m}{n_M}\mathcal{P} \propto \frac{n_M}{n_m} ,$$

since $\mathcal{P} \propto (n_M/n_m)^2$ in this limit. The change in the transmission for a given change in n_m/n_M would not be as great at high [H] as at low [H], were it not for the action of the internal resonator, which magnifies small changes in the single-pass absorption.

There is no measurement on C-mod of the minority concentration in the plasma center. The sawtooth modulation seen on the IW probes can be explained by supposing that the ratio n_H/n_D decreases at a sawtooth crash by a greater percentage than n_e does. This explaination correctly predicts that the sense of the sawteeth seen on the IW probes reverses as the the minority conncentration increases.

5.7 Redistribution of Fast Ions

There is reason to believe that fast ions are preferentially ejected from the plasma core during the sawtooth crash. Analysis of JET data has led to the conclusion that 40% of the fast ions are ejected from the plasma core to outside the q=1 surface during a sawtooth crash [67], so that the fast ion density profile becomes hollow after a sawtooth crash.

If a similar redistribution happens on C-Mod, then n_H in the plasma core decreases by 40% at a sawtooth crash, then using the parameters for the low-concentration shot shown in Figure 5.9 ($n_e(0) = 2.8 \times 10^{20}$ m^{-3}, n_H/n_D= 0.025, averaged over many sawtooth crashes), then Equation 5.4 predicts a change in transmission of $\Delta T_{ST}/T_{AV} \sim 0.5$, which agrees with what is seen. For the high-concentration case, shown in 5.10 ($n_e(0) = 3.0\times 10^{20}$ m^{-3}, n_H/n_D= 0.195), the conjectured redistribution of fast ions predicts $\Delta T_{ST}/T_{AV} \sim 0.1$, which is considerably smaller than is observed, though in this case the observation consists of a large change in a small signal (the power detected by the loop probes).

The inverse sawteeth seen on the IW probe signals at low n_H/n_D may also be

explained purely by changing minority temperature, if one assumes that the minority starts out just after a sawtooth crash with $T_H \sim T_e$ and is heated during the sawtooth cycle to $T_H = T_{tail} \sim 40$ KeV. A combination of changing temperature and density may also be responsible for the low n_H/n_D data. The changing density model (ejection of fast ions from the core) appears the most likely, due to its ability to explain not only the low n_H/n_D data but also the high n_H/n_D data.

5.8 Discussion of minority concentration scan data

It is apparent that it is easier to analyze the propogation of RF waves across high-single-pass-absorption plasmas than across low-single-pass-absorption plasmas. Alcator C-Mod is well-suited to this analysis because its high-density, 5.4 T D(H) plasmas have single-pass absorption in excess of 90 %. In addition, the C-Mod edge plasma is generally free of ELMs, which affect the loop probe signal by changing the position of the $n_\parallel^2 = \mathcal{R}$ cutoff at the plasma edge.

For the case of D(H), a single-pass model extended by the inclusion of an internal resonator on the low-field side of the $n_\parallel^2 = L$ layer is found to agree well not only with measurements of the transmitted power, but also with measurements of the absorbed power. Since the model does not include mode conversion, this is grounds for concluding that mode conversion is not an important process in C-Mod D(H) plasmas at 5.4 T. The single-pass model fails for D(^{3}He) plasmas at 7.9 T, and the evidence for off-axis heating shown in [55] implies that in this scenario a significant fraction of the RF power undergoes mode-conversion at the $n_\parallel^2 = S$ layer.

To our knowledge, the effect of sawtooth oscillations on fast wave propagation has never before been noted or studied. The remarkable fact that the sense of the sawtooth modulation observed on the inner-wall loop probes changes from inverse to normal as the Hydrogen fraction increases can be understood as a consequence of the dependence of the fast-wave polarization on the Hydrogen fraction. From the appearance of sawtooth oscillations on the loop probe signals in the first place, a minority density profile may be inferred which differs considerably from the electron

density profile.

Chapter 6

Nonlinear Processes

This chapter concerns spectra taken from floating Langmuir probes during RF heating of a two-species plasma. On certain occassions spectral components appear at frequencies other than the transmitter frequency. These subsidiary spectral "peaks" are thought to be products of the Parametric Decay Instability (PDI), a non-linear process by which a propagating wave (the "pump") decays into two daughter waves, subject to the selection rules described in Section 6.5. The primary effects of PDI are the production of fast particles and the generation of decay waves, which are seen as subsidiary peaks on Langmuir probe spectra [68]. The subsidiary peaks on C-Mod spectra are always smaller in amplitude than the pump by at least 10 dB, and whenever the subsidiary peaks appear one of them is always close to one of the ion cyclotron frequencies, evaluated at the probe. The amplitudes of the subsidiary peaks appear to be dependent on the magnetic field, being large when the transmitter frequency is an integer multiple of the cyclotron harmonic of the majority or minority species in the edge. Subsidiary peaks are not observed on spectra from loop probes. During RF heating the Charge Exchange (CX) observes a large energetic neutral flux due to deposition of RF power in the edge caused by PDI [59]. The RF power threshold for this "edge heating" decreases from $P_{RF} \geq 700$ kW to $P_{RF} \sim 10$ kW when a cyclotron harmonic moves through the plasma edge. Impurity production does not appear to be correlated with the observation of PDI or edge heating. PDI has not been observed on any other C-Mod diagnostic.

6.1 Observation of PDI on Other Tokamaks

PDI and edge heating have been thoroughly studied on DIII-D during IBW heating [69]. The two phenomena were found to be correlated, and to reach maximum amplitude when an ion cyclotron harmonic was present in the plasma edge. The probe spectra in [69] show what appear to be higher levels of PDI than has been seen on C-mod, and PDI in front of the antenna is presented as a possible power-loss mechanism responsible for the observed lack of core heating during IBW launch. C-Mod does not usually suffer from a lack of core heating during ICRF. One possible conclusion is that PDI is more readily excited by IBW launchers than by fast wave launchers.

Edge heating and PDI were also found to be associated on JT-60 [46] during second harmonic heating in pure hydrogen plasmas, and during second harmonic minority heating in He(H) plasmas during (0,0) plasing. The amplitude of the PDI was found to increase as the toroidal field decreased, with no sign being seen of a "resonance" phenomena associated with the passage of a ion cyclotron resonance through the edge. The magnetic field scan shown in [46] includes discrete values of B separated by approximately 5 %, which would be too coarse to detect the resonance phenomena seen on C-mod. A secondary effect of PDI reported on JT-60 is enhancement of impurity production [70]. This was looked for but not observed on C-Mod [59].

Edge heating and PDI were observed, but no correlation was claimed, on TEXTOR [71]. Three types of PDI were identified: decay into an ion Bernstein wave and an ion cyclotron quasimode, decay into an ion Bernstein wave and an low-frequency electron quasimode, and decay into two propagating slow waves [72]. The theory of the former two decays is presented in [73] and the theory of the latter decay is presented in [74].

Edge heating and PDI were also observed during lower hybrid heating on WEGA [75]. The first observation of PDI in a tokamak was made during lower hybrid heating on ATC in 1976 [76]. PDI was observed on ASDEX during hydrogen second harmonic heating in one- and two-species plasmas [77], and attributed to large electric fields in front of the antenna. The PDI was only observed at a few specific values of magnetic

field. During lower hybrid heating on PETULA, spectral peaks at nf_{Ci} were observed on signals from electrostatic and unshielded loop antenas, and increased $F(v_\perp)$ at high $v_\perp$ was observed on the PCX. [78]. PDI has also been observed during ICRF heating on JET [79].

6.2 RF Probe Data during Magnetic Field Ramps

On 22 January 1998 nine shots were run with magnetic field ramps. These ramps caused the cyclotron harmonic $f_{RF}/f_{CD} = 3$ layer to sweep past the front of the antennas. P_{RF} was maintained above 2 MW, with roughly 1 MW from each antenna, except during brief periods when one antenna tripped out. The current was 1 MA for the first seven shots and was swept between 800 kA and 1.2 MA for the last two. The target density was set at $\overline{n}_e = 1.7 \times 10^{20}$ for the first eight shots and was raised to $\overline{n}_e = 2.0 \times 10^{20}$ for the ninth shot. All shots went into H-mode for at least part of the time the RF was on.

6.2.1 RF Probe Setup

During this run day spectrum analyzers were hooked to two RF probes, mounted on different poloidal limiters, at different major radii: Probe 1, at R=.891 m, on the GH limiter, and Probe 2, at R=.851 m, on the AB limiter. Figure 6.1 shows the relevant geometry, mapped to a single poloidal plane, including probe locations, limiter profile, and antenna profile including Faraday shield rod cross-sections (note that the horizontal scale has been expanded). Both probes lie on field lines which pass in front of one of the antennas; neither of these field lines passes in front of the antenna at the midplane. (Also plotted is the position of the separatrix and the location of the $f_{RF}/f_{CD} = 3$ layer, calculated with the help of EFIT, for a time when the subsidiary peaks appeared.)

The spectrum analyzers were set to free-run. Probe 1 was hooked to a Hewlett-Packard Model HP8554B, with a sweep time of 20 ms, a resolution bandwidth of 100 kHz, a span of 100 MHz centered on 48 Mhz, and a dead time of 5 ms between sweeps.

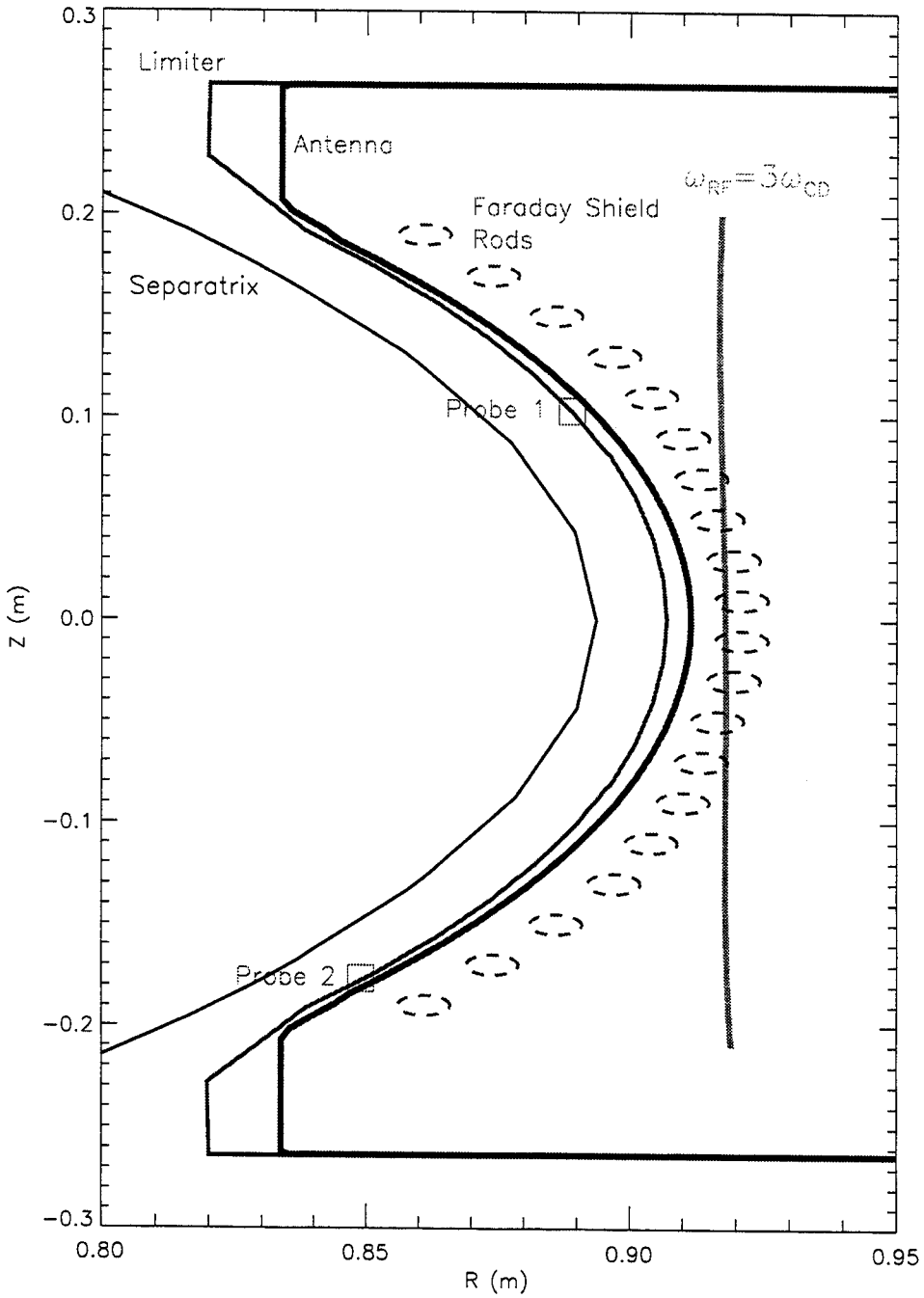

Figure 6.1: Diagram of Edge During PDI Observation

Probe 2 was hooked to an HP8565A, with corresponding parameters of 23 ms, 300 kHz, 100 MHz, 48 MHz and 18 ms. Each analyzer has 50 Ohm input impedance, so a capacitive inner-outer DC break (effectively a high-pass filter with $f_0 \sim 1$ MHz) was inserted between the probe and the analyzer to prevent DC current from being drawn.

6.2.2 RF Probe Data during Field Ramps

Data from the nine field-ramp shots is summarized in Figures 6.2 and 6.3. Figure 6.2 shows data a total of 329 spectra from Probe 1. The first and second traces show the amplitude and frequency of the upper subsidiary peak, as determined by a computer program. Solid diamonds indicate those spectra on which a single outstanding peak was apparent to the eye. The x-axis is the magnetic field at the probe, including the contributions from the plasma current and the EF coils, calculated by EFIT. The shaded region on the first trace indicates the range of magnetic fields (3.6 T < B < 3.7 T) for which the subsidiary peak was observed. As will be discussed below, in this range of magnetic fields the $f_{RF}/f_{CD} = 3$ layer is passing by the antenna Faraday screen, which is at R=0.92 m. The second trace shows the frequency of the subsidiary peak, where again the solid diamonds indicate spectra on which the subsidiary peak was apparent to the eye. The solid line indicates $f_U/f_{CD} = 2$, evaluated at the probe (R = 0.891 m, z = 0.103 m); the outstanding upper decay peaks appear to satisfy $f_U/f_{CD} = 1.9$ evaluated at the probe.

The third and fourth traces show the amplitude and frequency of the lower subsidiary peak. This peak appears at the same magnetic field as the upper subsidiary peak, but occurs less frequently and is of lower amplitude. Overplotted on the fourth trace is $f_L/f_{CD} = 1$ evaluated at the probe. The frequencies of the outstanding lower decay peaks exactly match f_{CD} at the probe.

Figure 6.3 summarizes the data from the same nine shots for Probe 2, a total of 194 spectra. The upper subsidiary peak grows large during the range 3.8 T < B < 3.9 T, which is 5 % higher than for the first probe. Note that the major radius of this probe is about 5 % smaller than the major radius of the Probe 1. The frequencies of

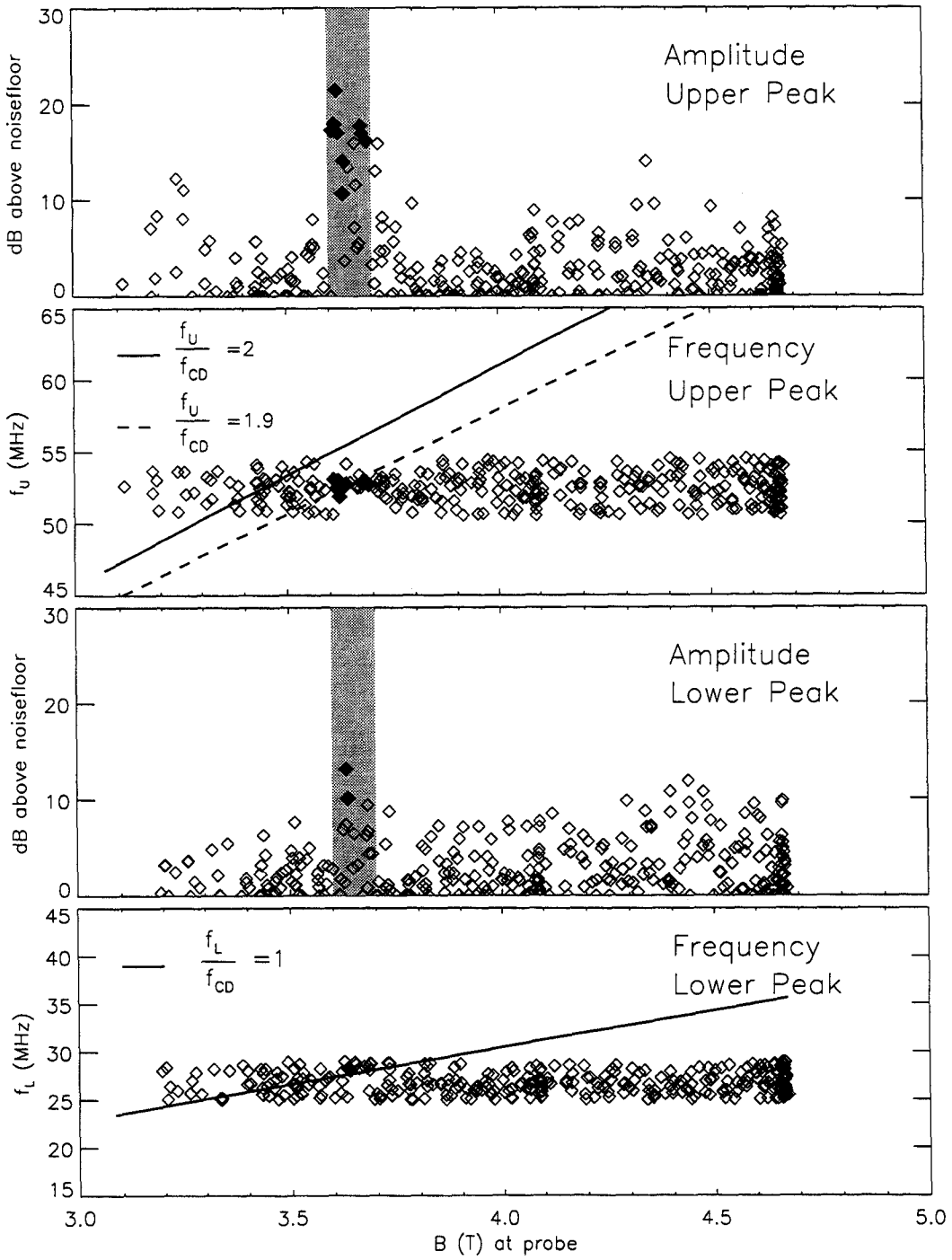

Figure 6.2: Data from Probe 1, R=.891 m

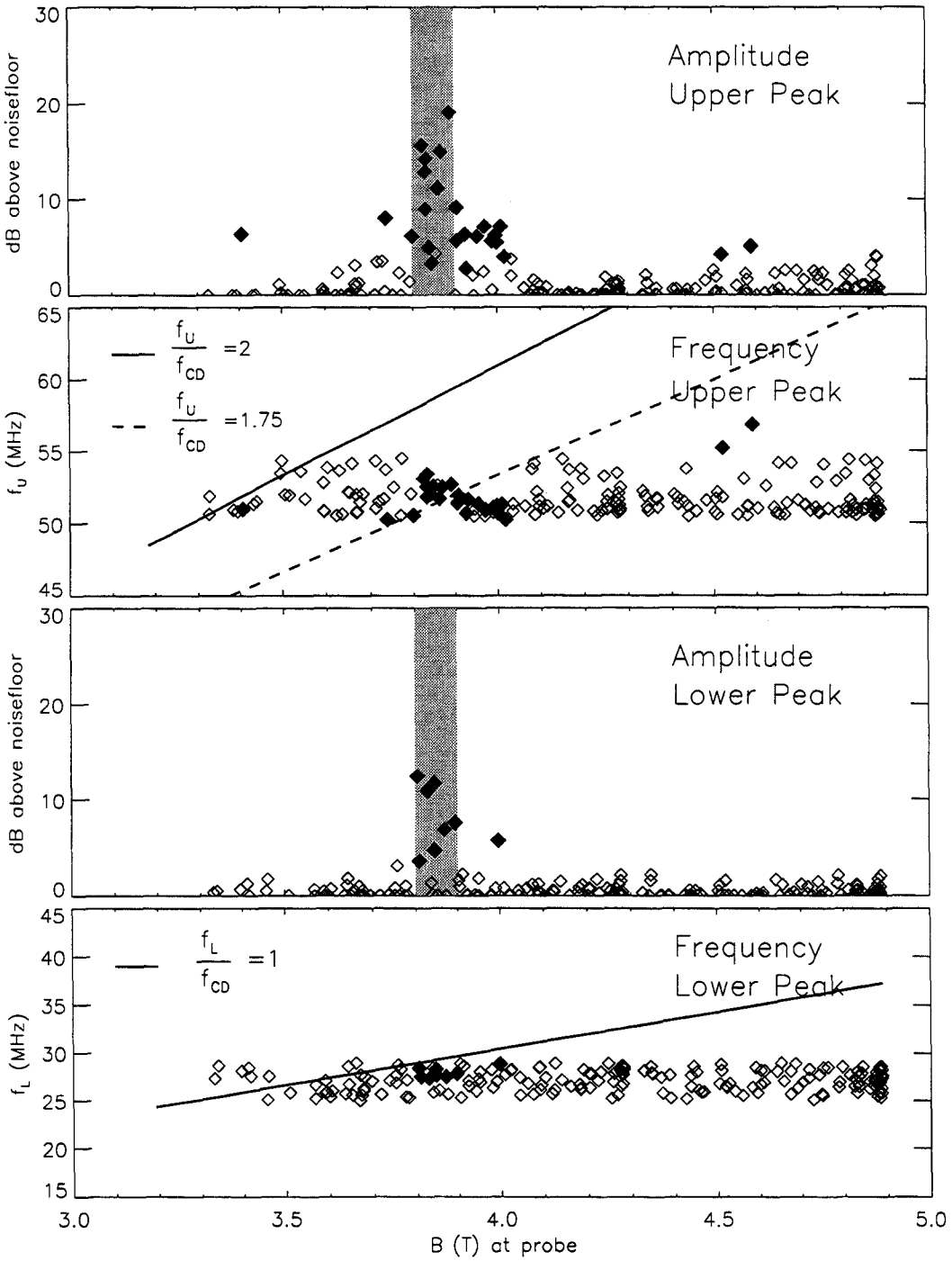

Figure 6.3: Data from Probe 2, R=.851 m

the outstanding upper decay peaks satisfy $f_U/f_{CD} = 1.75$ evaluated at the probe (R = 0.851 m, z= -0.177 m), as compared to $f_U/f_{CD} = 1.9$ for probe 1.

6.2.3 Comparison of Probe Data

Data from the two probes may be compared by plotting the amplitude of the subsidiary peak against the location of the majority cyclotron resonance harmonic. The third harmonic of the Deuterium cyclotron resonance, $f_{RF}/f_{CD} = 3$, occurs at a magnetic field B = 3.51 T when $f_{RF} = 80$ MHz. The location of the B=3.51 T surface may be calculated from EFIT data. In Figure 6.4 the amplitude data from Figures 6.2 and 6.3 is plotted against the radius of the $f_{RF}/f_{CD} = 3$ layer at midplane, which is homologous to time. The amplitude maxima for both probes occur when the $f_{RF}/f_{CD} = 3$ layer is at R=0.92 m at the midplane, and have widths of approximately 2 cm. It is important to note that the subsidiary spectral peaks reach maximum amplitude for both probes at the same time, even though the magnetic fields at the probes differ from each other by 5 %. The major radius R=0.92 m is approximately the radius of the center of Faraday shield rods (see Figure 6.1, on which the $f_{RF}/f_{CD} = 3$ layer is plotted as a nearly vertical green line). At lower magnetic fields ($f_{RF}/f_{CD} = 3$ layer at smaller radius) the amplitude of the subsidiary peaks drops rapidly below the noise floor, while at higher magnetic fields low-amplitude subsidiary peaks are detected until the $f_{RF}/f_{CD} = 3$ layer reaches about 0.99 m, at which time $f_{RF}/f_{CD} = 2.75$ at the major radius of the Faraday shield.

The low magnetic field limit can be traced to the dispersion relation of the IBW (shown in Figure 6.9). The IBW cannot propagate through an ion cyclotron harmonic layer; hence, when the $f_{RF}/f_{CD} = 3$ layer lies in between the probe and the front of the antenna, no PDI will be seen at the probe.

6.2.4 Importance of H-mode

The nine shots included in this dataset each experience H-mode for some interval. For eight of the shots, the plasma is in H-mode during the majority of the time when the

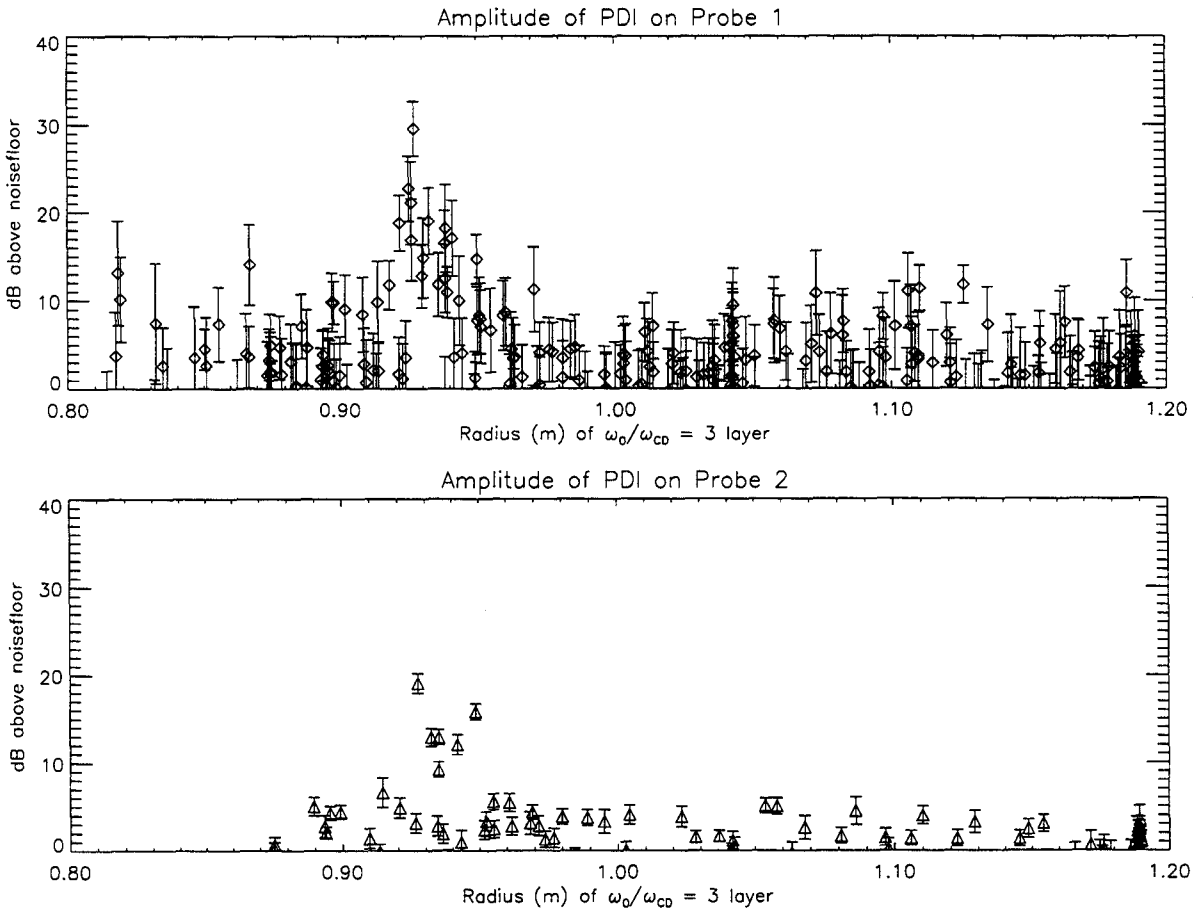

Figure 6.4: Amplitude of PDI vs. position of $\frac{f_{RF}}{f_{CD}} = 3$ layer

$f_{RF}/f_{CD} = 3$ layer is passing by the Faraday screen. On these shots PDI is observed on at least one spectrum. For the ninth shot the plasma is in L-mode for the duration of the passage of the resonance layer, and no PDI is observed.

6.2.5 Summary of RF Probe Data During Field Ramps

The interpretation of this data is complicated by the dependence of the IBW group velocity on magnetic field, but the simplest picture which fits the data may be summarized as follows: PDI occurs when the $f_{RF}/f_{CD} = 3$ layer passes the front of the antenna Faraday shield; the effective width of this layer is about 2 cm; low-amplitude PDI may occur at higher magnetic fields such that $f_{RF}/f_{CD} \geq 2.75$ at the antenna

Faraday shield; the amplitude of the upper decay peak is generally larger than the amplitude of the lower decay peak; PDI is not observed during L-mode.

6.3 Edge Heating During Field Ramps

The CX observes bursts of energetic particles marking the passage of a cyclotron harmonic through the edge. The bursts are caused by the transfer of power from the fast wave to ion kinetic energy by means of PDI. The threshold RF power required for the PDI to become unstable drops by an order of magnitude near a cyclotron resonance layer [59], so at constant RF power the PDI grows in size and dies away again as the magnetic field is ramped, causing the burst of particles.

Figure 6.5 shows the input RF power, the magnetic field, a typical deuterium CX

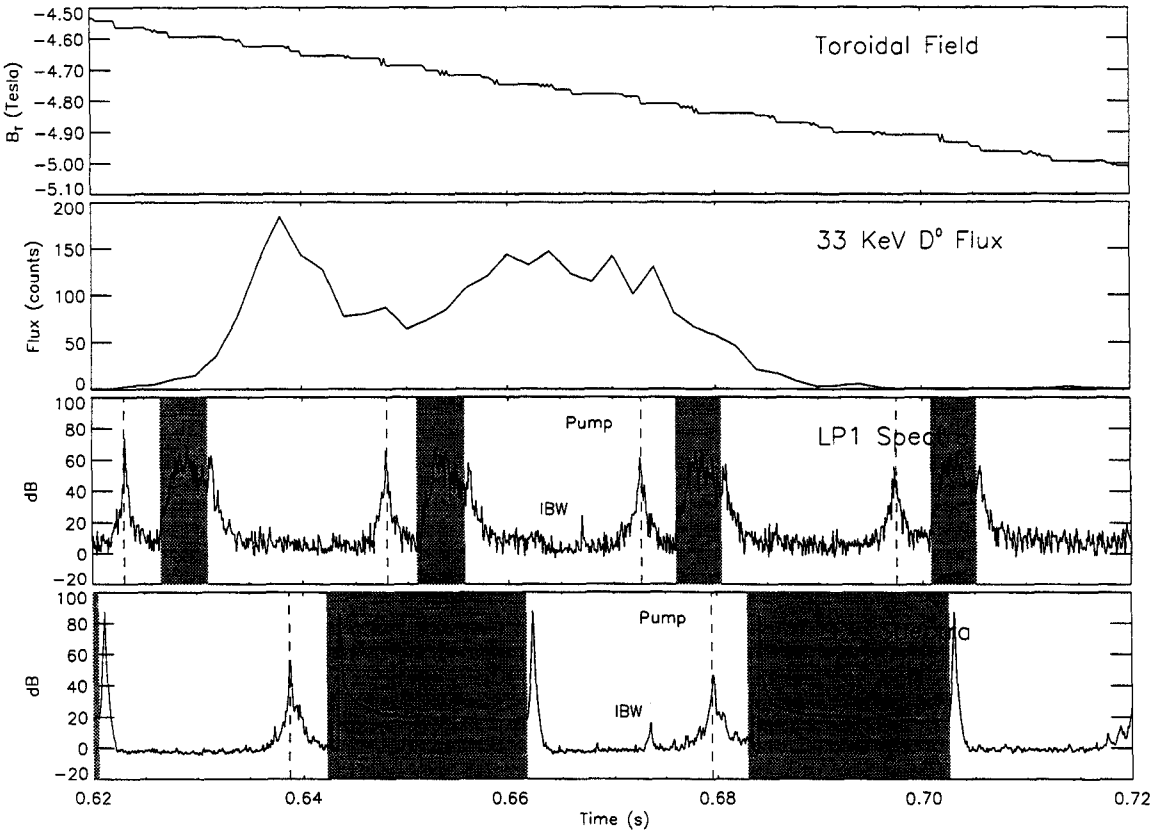

Figure 6.5: Comparison of Probe and CX Data

channel, and the raw data from the two Langmuir probes, all plotted as a function

of time. The probe data is the output of free-running spectrum analyzers. These devices sweep a band-pass filter through a spectrum in a preset time, then experience a dead-time (shaded region) as the filter is reset. The pump wave is flagged by a dashed line on each spectrum; also visible on each spectrum is the zero-frequency peak. On one spectrum from each probe an upper subsidiary peak may be seen. The CX flux appears before—at a lower magnetic field than—the subsidiary peak appears on either probe. The CX flux is also large for a larger range of magnetic field than the range over which subsidiary peaks on seen on the probe spectra.

6.4 RF Probe Spectra During Standard Heating Scenarios

Four minority heating scenarios have been investigated on C-Mod, all with deuterium majority: fundamental and second harmonic heating of H and ^{3}He. Effective minority heating has been observed on C-Mod for magnetic fields that differ by up to 10 % from the value required to put the minority cyclotron resonance on axis. Table 6.1 shows the standard heating scenarios, as well as two variants for which deuterium

Scenario	B_T *on axis*	*B at antenna*	*Harmonic at antenna*
D(H) at $2f_{CH}$	2.8 T	2.1 T	$5f_{CD}$
Off-axis D(^{3}He) at $2f_{CHe}$	3.7	2.6	$3f_{CHe}$, $4f_{CD}$, $2f_{CH}$
D(^{3}He) at $2f_{CHe}$	4.0	2.9	none
Off-axis D(H) at f_{CH}	4.8	3.5	$3f_{CD}$
D(H) at f_{CH}	5.3	3.8	none
D(^{3}He) at f_{CHe}	7.9	5.7	none

Table 6.1: PDI overview

cyclotron harmonics occur at the front of the antenna. The second column gives the toroidal field on the magnetic axis, the third gives the total field, including plasma current and shaping coil contributions, at the Faraday screen (R=0.92 m), and the fourth lists the cyclotron harmonic (if there is one) at the front of the antenna. The $2f_{CD}$ ($= f_{CH}$) layer lies at the front of the antenna for a toroidal field in the vicinity

of 7.0 T, but RF heating at this field has not been investigated for fear of damaging the antenna.

6.4.1 Spectra Showing Peaks at nf_{CD}

For all but one of the scenarios listed in Table 6.1, subsidiary peaks occur (if they occur at all) at the majority fundamental cyclotron frequency evaluated at the probe, and at the frequency which is the difference between this and the transmitter frequency. These scenarios include nearly all C-Mod shots. Subsidiary peaks at the minority cyclotron frequency only been seen in off-axis second harmonic heating in D(^{3}He), as described in Section 6.4.2.

The large majority of C-Mod shots use D(H) at 5.3 T, a high single-pass absorption scenario. An RF probe spectrum taken during D(H) heating in a 5.3 T shot is shown in Figure 6.6. The RF probe was mounted on a probe drive and was located in the private flux region in between two poloidal limiters. The peak at 80 MHz corresponds to the pump wave, while the lower-frequency subsidiary peak is close to the deuterium cyclotron frequency evaluated at the probe location, which is $f_{CD} = 29.1$ MHz. The subsidiary peaks on private-flux-region probe spectra are rarely more prominent than they are here, where they are at least 40 dB down from the 80 MHz peak. Often the subsidiary peaks are buried below the noise floor. Probes mounted on the RF limiter rarely produced spectra showing subsidiary peaks.

In the early days of Alcator C-Mod other heating scenarios were investigated which provided especially interesting spectra. An RF probe spectrum taken during a 2.75 T shot, which corresponds to second harmonic minority heating in D(H), is shown in Figure 6.7. This has low single-pass absorption compared to fundamental minority heating in D(H) at 5.4 T. At the time this spectra was taken the plasma was in ELM-free H-mode. The subsidiary peaks show considerably more power, the larger of the two being barely 10 dB down from the peak at the transmitter frequency (this is the largest subsidiary peak yet seen on RF probe spectra on C-mod). At this toroidal field the $f_{RF}/f_{CD} = 5$ layer is at R=0.90 m, in between the front of the antenna and the probe, which was at R=.889 m, just in front of the limiter. The

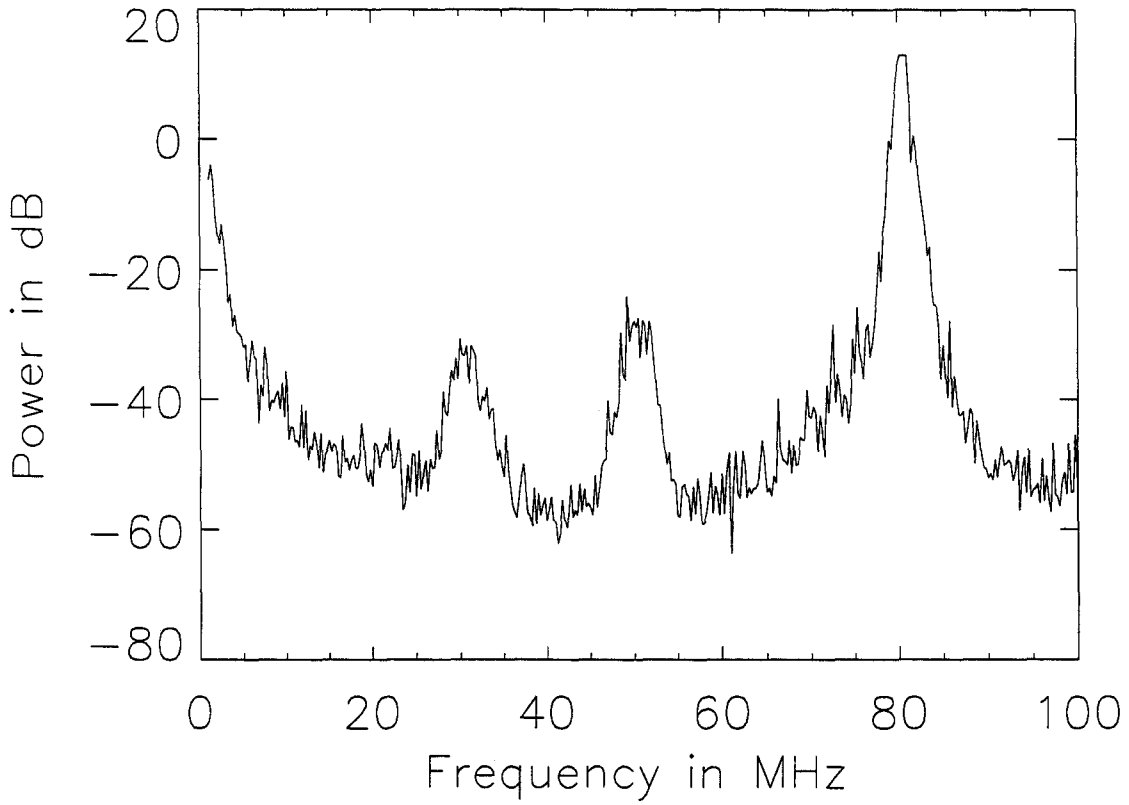

Figure 6.6: RF probe spectrum during 5.4 T shot

subsidiary peaks have 3 dB half-widths of at least 2 MHz, much more than the width of the transmitter peak at 80 MHz. At the probe, $f_{CD} = 16.2$ MHz; there are peaks apparent near f_{CD} and its first two harmonics.

Probe spectra taken during D(^{3}He) shots at 7.9 T are qualitatively similar to those taken during D(H) at 5.4 T, although the former scenario has a much lower single-pass absorption. Small subsidiary peaks regularly appear at 37 MHz and 43 MHz, the latter being very close to the deuterium fundamental at the probe, $f_{CD} = 43$ MHz. These small subsidiary peaks are again rarely present on spectra from limiter probes. Subsidiary peaks have not been seen on probe spectra taken during the few ($N < 10$) D(^{3}He) shots at 4.0 T. Subsidiary peaks have, however, been seen on the two of the three D(^{3}He) shots during which the field was ramped through 3.7 T in

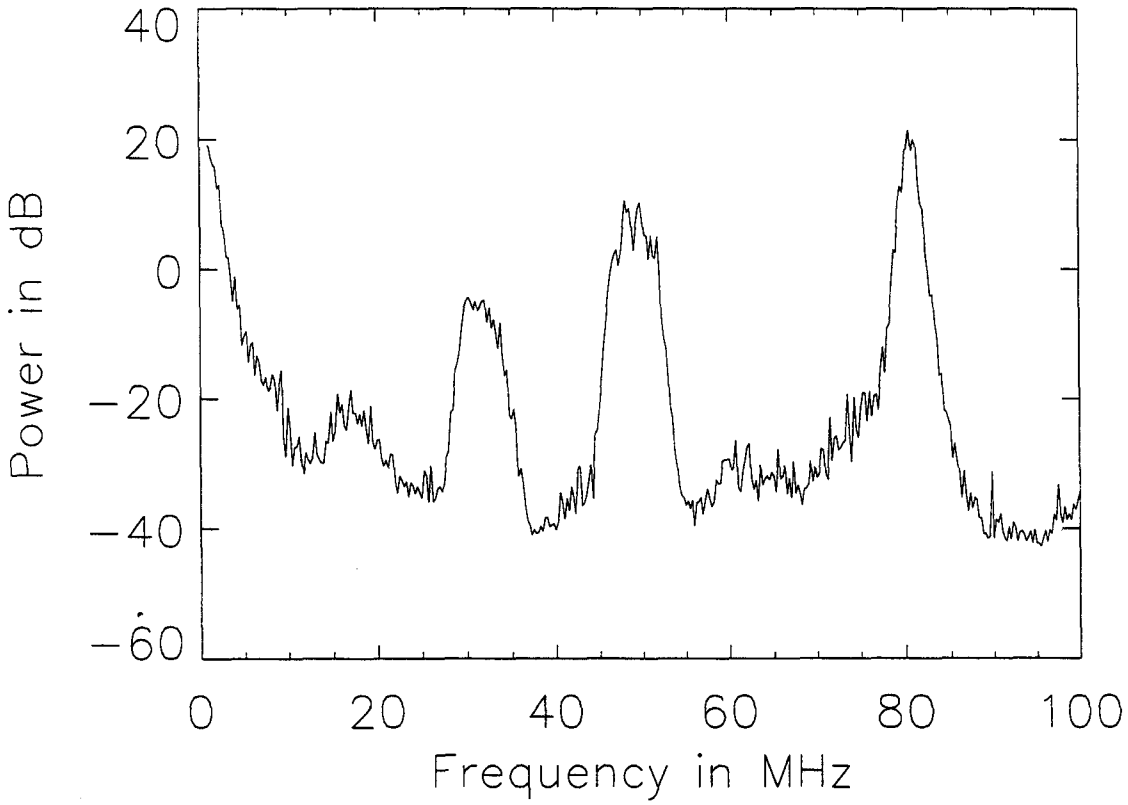

Figure 6.7: RF probe spectrum during 2.75 T shot

search of optimal heating.

6.4.2 Spectra Showing Peaks at nf_{CHe}

The three successive shots on which the field was ramped through 3.7 T in search of optimal second-harmonic minority heating in D(^{3}He) are of interest because they show subsidiary peaks at multiples of the minority fundamental, instead of the majority fundamental, and because these peaks disappear as the minority gas puff is diminished, while a single peak appears at the hydrogen fundamental. This progression is illustrated in Figure 6.8. At the probe f_{CHe} = 28.3 MHz and f_{CH} = 42.4 MHz. The amount of Helium-3 in the plasma is undiagnosed but the trend can be

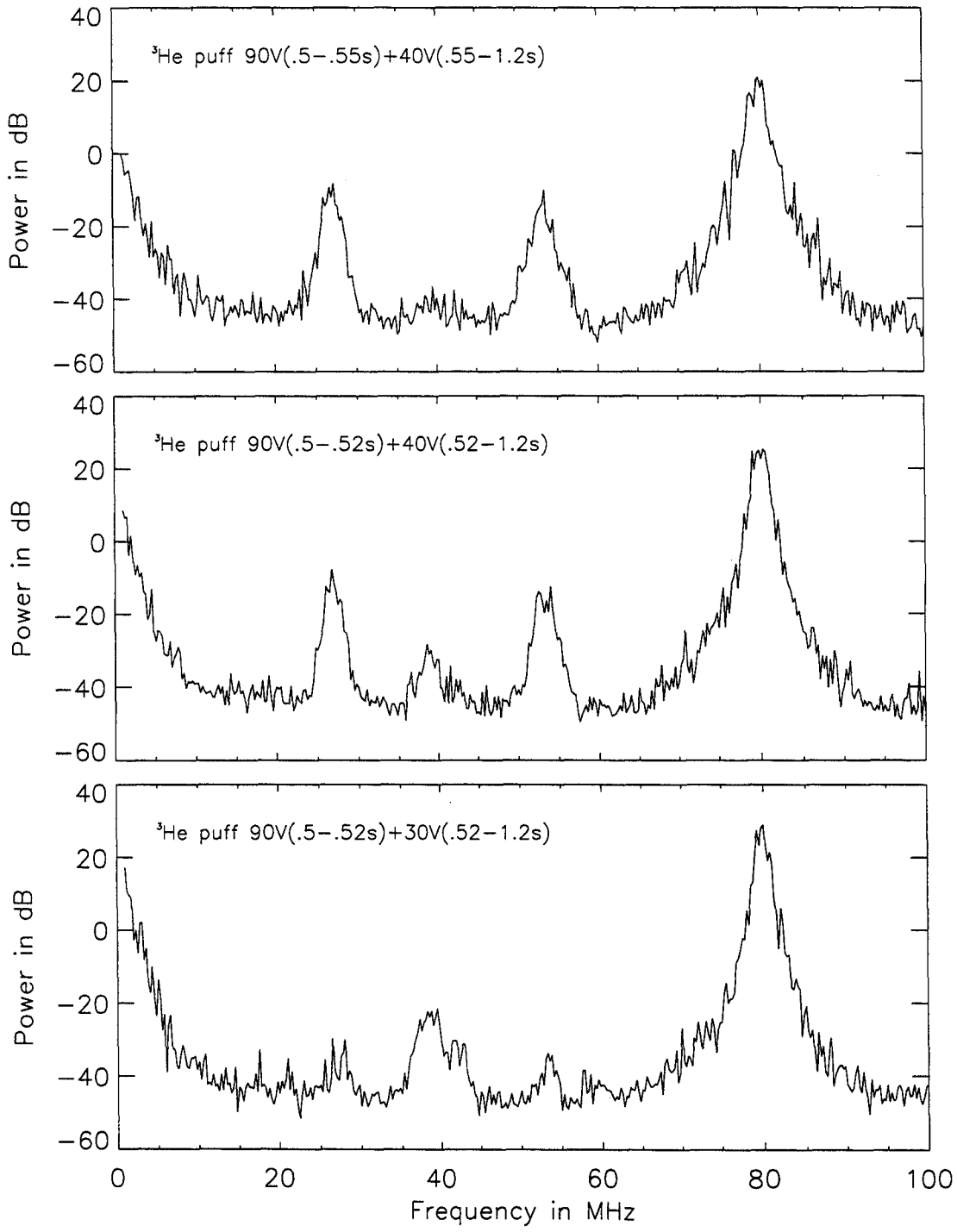

Figure 6.8: Spectral peaks at minority f_C

followed from the voltage applied to the gas puff valve, which shows that the number of Helium-3 atoms puffed into the vessel decreases during these three shots. No hydrogen was puffed during these shots, but the walls had been boronized and would have sourced hydrogen during the shot.

6.5 Theory of PDI

In order to solve Maxwell's equations for continuous media one must assume a relation between the currents $\mathbf{j}$ and the fields $\mathbf{E}, \mathbf{B}$. In the non-relativistic limit, it is usually sufficient to assume that $\mathbf{j} = \sigma\mathbf{E}$. This is understood as the first term in the expansion of $\mathbf{j}$ in a power series in $\mathbf{E}$, accurate for small $\mathbf{E}$. In this case the various Fourier components of $\mathbf{E}$ evolve separately. For finite values of $\mathbf{E}$ it may be necessary to include the second order term in the expansion. The presence of this nonlinearity allows different Fourier components of $\mathbf{E}$ to be mixed. The simplest nonlinear interaction involving a propagating wave redistributes energy from the orignal "pump" field to those Fourier components of the randomly fluctuating plasma which themselves obey the dispersion relations of propagating waves. In order to conserve energy and momentum, three waves must be involved and must satisfy the selection rules [80]:

$$\mathbf{k}_1 = \mathbf{k}_2 + \mathbf{k}_3 \ , \ \omega(\mathbf{k}_1) = \omega(\mathbf{k}_2) + \omega(\mathbf{k}_3) \ . \tag{6.1}$$

This three-wave interaction is called the resonant Parametric Decay Instability (PDI). If the coupling is strong enough, the pump field may lose energy to waves which are strongly damped, in which case the PDI is "non-resonant"

If the fast wave pump field satisfies $\omega_1 \geq 2.5\omega_{Ci}$, then these selection rules may be satisfied if the daughter waves are an ion Bernstein wave (IBW) and an ion cyclotron quasi-mode (ICQ), or IBW and an electron cyclotron quasi-mode (ECQ) [73]. If $\omega_1 < 2\omega_{Ci}$, decay into two propagating slow waves is possible [74], and in multi-species plasmas decay into two EIC waves is possible [81].

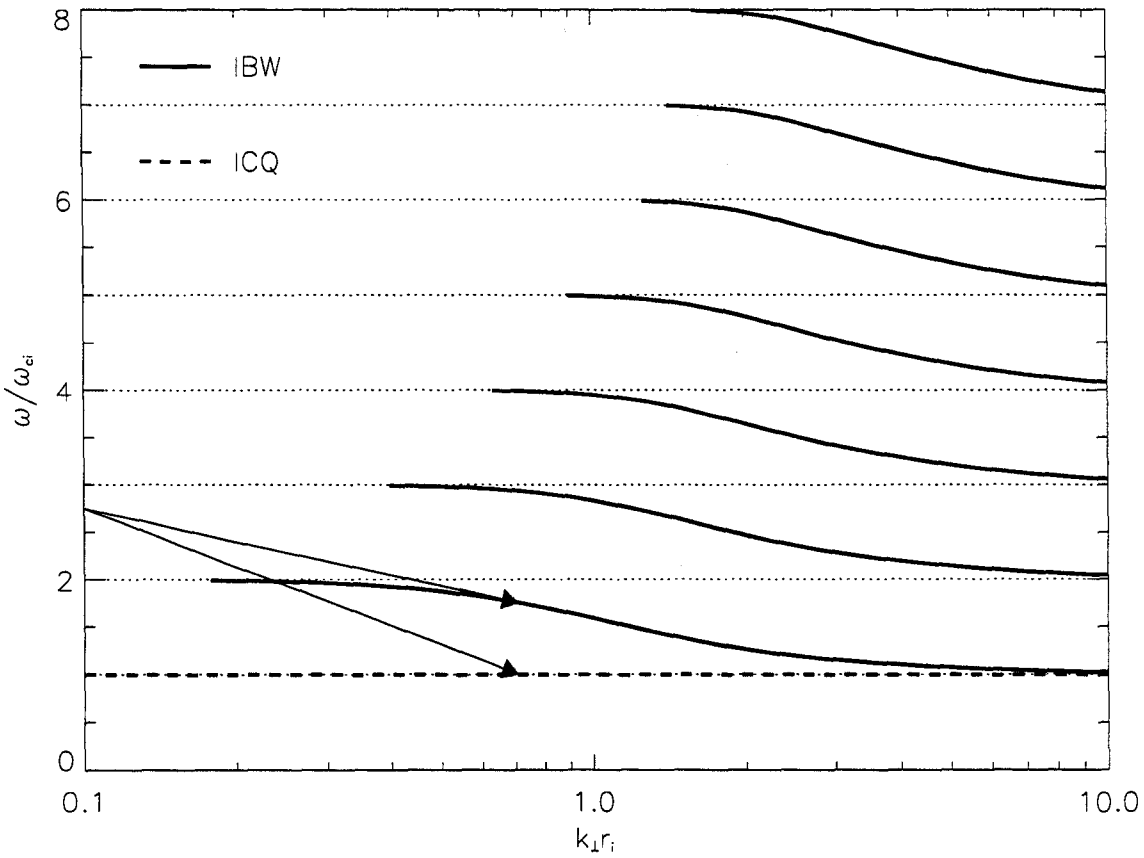

Figure 6.9: PDI into IBW and ICQ

6.5.1 PDI in Non-uniform Plasmas

When the plasma density, temperature, and magnetic field are spatially varying, as in a tokamak, the most unstable decay available to the fast wave is decay into an IBW and an ICQ. Solutions for the IBW dispersion relation for a typical choice of edge parameters ($n_e = 1 \times 10^{19}$, $T_e = 10$ eV, $k_\parallel = 40$ m^{-1}, $B = 4.0$ T) are shown in Figure 6.9. The IBW is restricted to $\omega/k_\parallel v_{the} \geq 3$ by Landau damping at large $k_\parallel$, but both $k_\parallel$ and $k_\perp$ change as the wave propagates through regions of changing magnetic field, density, or temperature. The IBW suffers strong cyclotron damping at $\omega = n\omega_{ci}$ and does not propagate across cyclotron harmonic layers. The 'dispersion relation' of the

non-propagating ICQ is $\mathrm{Im}(\chi_i) >> 1$, where the ion susceptibility

$$\chi_i = \frac{2\omega_{pi}^2}{k^2 v_{thi}^2} e^{-b} \sum_{n=-\infty}^{n=\infty} I_n(b)\,[1 + \zeta_0 Z(\zeta_n)]$$

depends on finite Larmor radius $b = k_\perp^2 \rho_{ci}^2/2$ and on kinetic effects via the Fried-Conte plasma dispersion function $Z(\zeta_n)$, where $\zeta_n = (\omega - n\omega_{ci})/k_{\|} v_{thi}$. For frequencies $\omega \sim n\omega_{ci}$, χ_i is large and imaginary for a wide range of $k_\perp$ and $k_\|$, allowing it to match the wavevector of the IBW and satisfy the selection rules (Equation 6.1) for a wide range of plasma parameters, ensuring that the PDI has a large spatial region in which to grow.

6.6 Occurrence of PDI on C-Mod

The occurrence of PDI on C-mod is attributed in [59] to the large poloidal RF electric field E_θ^{RF} associated with the propagating fast wave in the vicinity of the antenna, from which energy is transferred to an IBW and a strongly-damped ICQ. Specifically, E_θ^{RF} is found to exceed the convective threshold for the non-resonant PDI to be driven unstable. E_θ^{RF} is assumed to be large in a region in front of the antenna. Energy is coupled from E_θ^{RF} to "seed" fluctuations at the IBW and ICQ frequencies, which are continually convecting into the region of large E_θ^{RF}. These fluctuations then grow, and take on the dispersion relations appropriate to the IBW and the ICQ. The growing IBW remains in the region where the pump wave is large for a time $\tau \sim L/v_g$, where L is the spatial extent of the region wherein the pump wave is large, and v_g is the group velocity of the IBW. In linear analysis the amplitudes of the decay waves grow with time like $e^{\gamma t}$, and the convective threshold is exceeded if $\gamma\tau > \pi$.

This threshold E_θ^{RF} decreases as the temperature decreases, and $T_e >> T_i$ in order for decay into an ICQ to be more unstable than decay into an ECQ. Since the temperatures of both species decrease at increasing distances from the separatrix, PDI is most unstable in the outer reaches of the scrape-off layer.

6.6.1 Spatial Structure of the Pump Wave

The fast wave approximately follows the dispersion relation $\omega = k_r v_a$, implying a group velocity $v_g = v_a e_r$, so that very little wave energy flows in the toroidal or poloidal directions. We therefore expect the pump wave to be restricted to the region in front of the antennas. Only if single-pass absorption were low would the pump wave have a significantly greater extent. This is bourne out by the decrements to Langmuir probe floating potential seen on the F-port scanning probe, due to sheath rectification, ΔV_f^{sh}, reported in Sec. 4.3.1. This probe is approximately 20 cm from the corner of the E-port RF antenna. During D(H) heating at 5.4 T (high single-pass absorption), the RF voltage afflicting this probe is much smaller than the RF voltage seen on a probe mounted on the antenna tiles; while during D(^{3}He) heating at 7.9 T, the two probes see comparable RF voltages. The data shown in Sec. 6.2 was taken during off-axis heating in D(H) in the vicinity of 4.8 T, which has high single-pass absorption, so the pump wave for those data would have been restricted to the region in front of the antennas.

The radial profile of E_θ^{RF} in the scrape-off layer describes a decrease from the maximum, at the current strap, to a value appropriate to the propagating wave, just inside the $n_\parallel^2 = \mathcal{R}$ cutoff. The field at the current strap is estimated from measurements in the transmission line leading to the antenna as $E_\theta^{CS} = (\sqrt{P_{For}} - \sqrt{P_{Ref}})\sqrt{Z_0}/L)$, where $L = 0.6$ m is the height of the antenna and Z_0 is 50 Ω, which produces $E_\theta^{CS} \sim 50$ KV/m during high-power operation. The field inside the plasma can be estimated from Faraday's law $c\nabla \times E = -\partial B/\partial t$, and the dispersion relation for the fast wave $\omega/k_\perp = v_a << c$. The latter relation shows that the energy contained in fluctuating E_θ is much less than is contained in fluctuating B_z. Equating the energy flux measured to be leaving the antenna with the Poynting flux associated with the fast wave gives

$$\frac{P_{RF}}{A} = \frac{c}{4\pi}(E \times B) = \frac{c^2}{4\pi v_a} E_\theta^2 \ ,$$

where A is the surface area of the antenna, approximately 2000 cm^2. Taking $n_D \sim 10^{14}$

cm^{-3} to characterize the main plasma, $E_\theta \sim 3000V/m$ just inside of the separatrix at an RF power of 1 MW (for the propagating fast wave $E_r \sim E_\theta >> E_z$). The radial profile of E_θ^{RF} may conveniently be approximated by an exponential fall-off from current strap to plasma edge, convoluted with an enhancement in the vicinity of the Faraday shield radius. The Faraday shield, which consists of rods d =9.5 mm thick, separated by gaps of $a = 3.4$ mm, enhances E_θ^{RF} in the gaps by a factor $d+a/a = 3.8$; the enhancement decays on a scale length $\sim a$ [82]. $E_\theta^{RF}(r)$ for a power level of 1 MW is illustrated in Figure 6.10. Note that the pump wave electric field grows in the

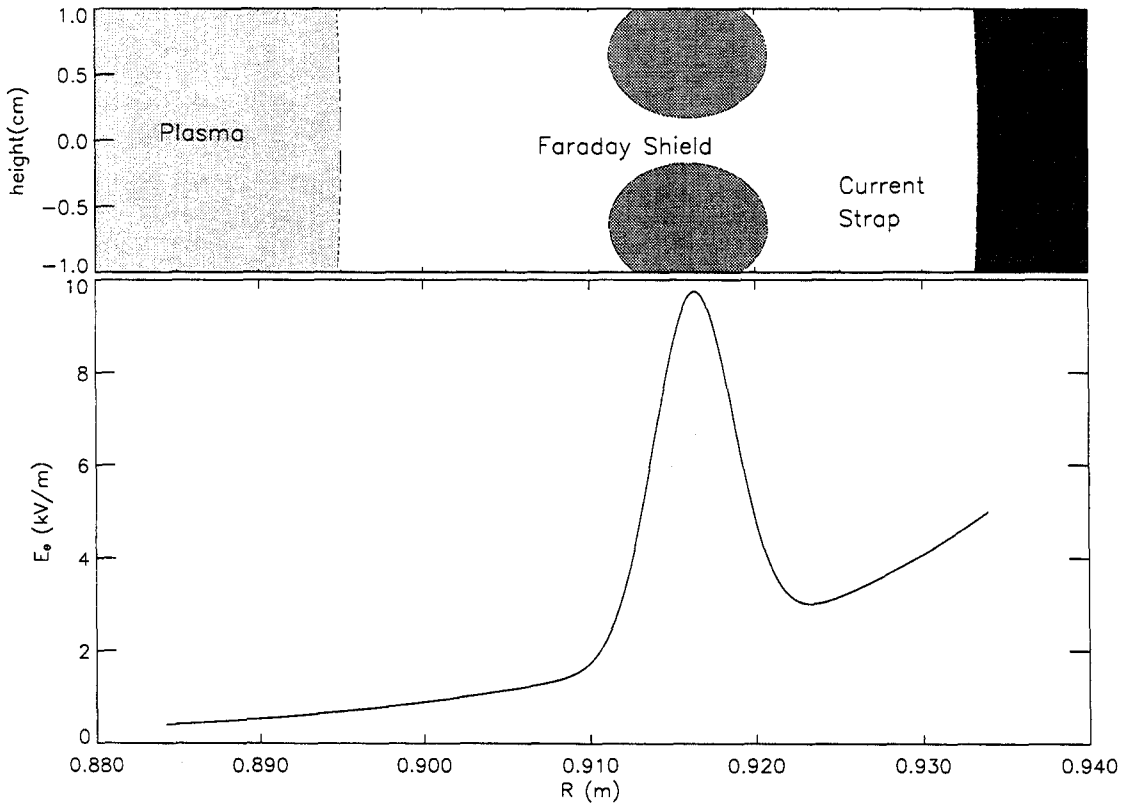

Figure 6.10: Estimated Radial Profile of Pump Wave

direction of pump wave propagation on the low-field side of the Faraday screen.

6.6.2 Spatial Structure of the Decay Waves

The spatial structure of the decay waves is determined by the evanescence of the antenna near-field (Figure 6.10) and the dispersion relation of the IBW (Figure 6.9). The convective threshold for PDI growth is more easily exceeded as the group velocity of the IBW

$$v_g \sim \left.\frac{d\omega}{dk_\perp}\right|_{k_\parallel}$$

approaches zero, as it does just above and just below a cyclotron harmonic.

Any IBW originating near the Faraday screen at $(n+\epsilon)f_{Ci}$ would not be detected by the probes on the limiters, being unable to propagate through the intervening $f = nf_{Ci}$ resonance layer. An IBW originating near the Faraday screen at $(n-\epsilon)f_{Ci}$ would be able to propagate inward in major radius. f_{IBW} being constant, f_{IBW}/f_{Ci} and therefore $k_\perp \rho_{Ci}$ decrease as the wave progresses into regions of higher magnetic field.

The calculation of threshold E_θ^{RF} required for PDI to be driven unstable, as a function of magnetic field, is given in [59]. It is found that the threshold $E_\theta^{RF} \propto \sqrt{P_{RF}}$ is attained at an RF power of $\sim$ 700 kW unless an $f_{RF} = nf_{CD}$ layer is present at the Faraday shield, in which case the threshold E_θ^{RF} is reached at an RF power of only $\sim$ 10 kW. This calculation assumes that the pump wave is spatially uniform. It has been shown that spatial nonuniformity in the pump wave can increase the amplification of the decay waves [83]; this effect has been measured on a linear device [84]. The PDI growth rate in the region where the pump fields themselves are increasing—the low-field side of the Faraday screen—may be larger than predicted in [59].

In the high single-pass absorption case, the pump field is localized to the antenna, dropping off quickly in the toroidal and poloidal directions. The growth rate of the IBW would be largest where the pump field is large and growing, just behind the Faraday screen. The amplitude of the IBW should be maximum in the vicinity of the Faraday screen, and largest at the times when $f_{FW} = (n+1-\epsilon)f_{Ci}$ at the location

of the largest E_θ^{RF} at 91.5 cm.

In the low single-pass absorption case, the pump field is demonstrably not localized toroidally and poloidally, and may even increase away from the antenna due to constuctive interference of the pump wave after multiple passes. The data does not suggest that PDI occurs with greater amplitude during lower single-pass absorption scenarios (eg fundamental minority heating in D(^{3}He) at 7.9 T), unless a cyclotron harmonic is present near the Faraday screen (eg second harmonic minority heating in D(H) at 2.75 T), indicating that the amplification of the decay wave due to spatial non-uniformity of the pump wave is of secondary importance compared to the location of the cyclotron harmonic layer.

6.7 Recommended Diagnostics for PDI Studies

Monitoring PDI in a complicated device like a tokamak requires thoughtful placement of diagnostics. Langmuir probes are needed at the antenna on the midplane (where the pump fields are largest), and some toroidal distance away, for example on adjacent limiters. A poloidal array of Langmuir probes (such as was used in this study) is needed to track the decay waves at constant minor radius but different major radius. A scanning Langmuir probe, located toroidally close to the antenna, would measure the radial profile of the decay waves. The decay waves could in principle be seen by other diagnostics, since one or both of them carry density fluctuations. Parametrically excited lower hybrid waves were observed by use of laser scattering during lower hybrid heating on Alcator C [85]; density fluctuations of sufficient magnitude would also be visible on reflectometer measurements, and on Phase Contrast Imaging, which could also be expected to provide information about the wavevectors of the decay waves. When the latter two diagnostics become available, it is important to use them to cross-check the validity of the Langmuir probe data. A passive CX diagnostic with a line-of-sight including the front of the antenna (as was present on C-Mod during the 1997-1998 run campaign) is necessary to monitor any edge heating caused by the PDI.

6.8 Limitation of RF Probe Data

The occurrence of PDI on tokamaks is sometimes inferred from RF probe spectra, in the absence of other diagnostic evidence [77], [70]. This is perilous when large RF potential fluctuations are known to exist near the probe. On C-Mod, as described in Chapter 4, RF potential fluctuations of many times T_e/e are known to exist in the edge plasma. An RF potential of order 100 V can act across the sheath surrounding the probe, which is less than 1 mm thick. The resulting electric field of 100 kV/m surpasses the field at the antenna's Faraday screen and can itself cause PDI[1].

On C-Mod, two assumptions are necessary to link measurements of spectral peaks by remote Langmuir probes to PDI theoretically predicted to occur in front of the antenna. The first concerns the propagation of the decay waves to the probe, the second concerns the relation of threshold cause to saturation effect. The IBW propagates along a direction which depends on whether f_{IBW} is just above or just below nf_{CD}, for example the IBW does not propagate through cyclotron resonances. It is possible the change in subsidiary peak amplitudes is a result of the passage of a "beam" of IBW power by the probe. It would take data from an array of probes to rule out this hypothesis. Since an array of functioning probes is not available, it is necessary to assume that the changes in amplitudes of the subsidiary peaks follow the change in amplitude of the PDI predicted to occur in front of the antenna. This is an especially important assumption in the low single-pass absorption scenario of second harmonic minority heating in D(H) at 2.75 T, when the pump fields may actually increase away from the antenna, and large PDI is observed on remote Langmuir probes. This is the most likely scenario for the observation of spatial amplification of PDI due to spatial growth of the pump wave.

The second assumption touches upon the limit of the linear theory. Once a process like PDI becomes unstable, the instability instantaneously begins to grow with time $\propto e^{\gamma t}$, as predicted by the linear theory. Since $1/\gamma \sim 10\mu s$ when a cyclotron harmonic is in the edge, the amplitude of the instability, as measured by signal of a free-

[1]The simultaneous appearance and disappearance of PDI on two remote probes isolated from each other suggests that this is not happening on C-Mod.

running spectrum analyzer, digitized at 10 kHz, reflects the process which has caused the instability to stop growing and to saturate. There is no theory of saturation; in fact even the process causing saturation is unknown. Perhaps the amplitude of the instability never saturates, that is never "equilibrates" with the changing edge conditions. For the purpose of this work it must be assumed that the measured amplitude of the subsidiary spectral peaks somehow correlates with γ/v_g which can be calculated from linear theory.

Chapter 7

Summary and Conclusions

Alcator C-Mod is an excellent tokamak on which to study RF phenomena with probes in the edge because it has the highest RF-power-to-surface-area ratio of any tokamak, and the RF system is used for the vast majority of shots; and since the edge group has developed highly sophisticated hardware and software for the analysis of Langmuir probe data. The three chapters 4, 5, and 6 represent the connections such a study must make to existing areas of research. Chapter 4 originated from a desire among members of the edge physics community to have Langmuir probe measurements during RF which were unaffected by sheath rectification, in order to study H-mode. On C-Mod Ohmic H-mode is obtained very rarely, so in order to obtain H-mode edge plasma parameters an RF-immune Langmuir probe is needed. The comparison between the ASP and the FSP links the data from the ASP to a large existing database. Similarly, the comparison of the loop probe data in Chapter 5 to the widely-used code FELICE validates the data, and makes it accessible to the RF heating community. Finally, the evidence for PDI shown in Chapter 6 is the most spectacular objective phenomenon seen by the Langmuir probes on C-Mod and deserves attention for that reason.

7.1 Summary of Results

Two new diagnostics were built and installed on Alcator C-Mod. A fast reciprocating probe was built from an existing design, modified to allow quantification of RF phenomena in the plasma. An array of loop probes were installed behind tiles on the inner wall. These loop probes are likewise distinguished from existing loop probes by their high bandwidth, which extends above the frequency of the RF heating.

7.1.1 ASP Results

The ASP was benchmarked against the FSP by multiple simultaneous scans into an Ohmic plasma. ASP profiles were considerably different from FSP profiles. In particular, the ASP T_e profile was much flatter than the FSP T_e profile. The ASP measured T_e on the separatrix to be 30 eV, compared to 60 eV measured by the FSP. This difference was found to be consistent with the operation of Ohm's law on a magnetic field line. One possible explanation for the low temperature measured by the ASP is recycling from the AB limiter immediately adjacent to it.

The ASP was not affected by RF sheath rectification during RF operation. This was due to its location, three ports away from the antennas, and not due to the attempt to suppress sheath rectification with quarter-wave stubs. The ASP measured the edge profiles in RF L-mode to be similar to Ohmic L-mode. The density gradient scale lengths seen in RF L-mode and RF H-mode were each about 1 cm, with the density at a given location in RF H-mode being about half the density at the same location in RF L-mode.

The density profile in the edge controls the evanescence of the fast wave and hence the antenna loading. The measured changes in the edge profiles between L-mode and H-mode are consistent with 20 % changes in loading seen during L-H transitions. The antennas also show occassional changes in loading of 50 % or more which are too large to be explained by changes and the edge parameters, and must therefore be caused by changing plasma conditions inside the separatrix.

Large floating potential fluctuations are generally observed on Langmuir probes

mounted on the RF antenna side tiles. These potential fluctuations are caused by magnetic field lines which link the side tiles to the poloidal limiter. These limiter circuits dissipate RF power by accelerating ions into the antenna side tiles and the limiters. The amount of dissipated power was calculated by integrating the product of the ASP ion saturation current density profile and the (fixed) antenna probe floating potential fluctuations over the surface areas of the antennas and limiters. The total dissipated power was found to be less than 50 kW in L-mode at 5.4 Tesla. It is likely that more power would be dissipated in 8 T L-mode.

7.1.2 Inner Wall Loop Probe Results

The inner wall probes detected a large RF magnetic field at the inner wall, extrapolated to be $B_{RF} \leq 5 \times 10^{-2}$ T at the tile surface. This field varied considerably during a shot, and decreased as the minority concentration increased in fundamental minority heating in D(H) at 5.4 T, but not in D(^{3}He) at 8.0 T. This field is due to the fast wave power which has crossed straight through the plasma from the antennas to the probes. The transmission factor was calculated as the power detected by the loop probes divided by the power launched from the antenna, and multipied by 3.75 $\times$ 10^6 to make it numerically equal to the "power radiated in the fast wave" calculated by the full-wave code FELICE. The probe measurement and FELICE showed good quantitative agreement through the entire minority concentration scan in D(H) at 5.4 T. A simple analytic model excellently predicted the data code results. At concentrations $n_H/n_e \leq 0.08$ a single-pass model with indistinct central absorption and evanescent layers fit the data, and at concentrations $n_H/n_e \geq 0.11$ a multiple pass model with an internal resonator on the low-field side of the evanescent layer fit the data. The tail temperature inferred from these measurements is 100 KeV.

The loop probe signals often shows modulation with the same timing as the central sawteeth. The loop probe signals definitely change before the sawtooth heat pulse has propagated past the r/a=0.5 layer. The size and sense of the sawteeth change with minority concentration in D(H) at 5.4 T. The sawteeth on the probe signal have the opposite sense from the sawteeth on the central T_e at low minority concentration, and

have the same sense at high minority concentration. This is quantitatively consistent with the analytic model at low concentrations and qualitatively consistent at high concentrations. The inverse sawteeth on the probe signal at low concentration are due to changing thickness of the resonance layer, and the sawteeth at high concentration are due to changing fast wave polarization. The sawteeth are too big to be caused by changes in the plasma density and must be due to redistribution of the minority ions during the sawtooth cycle, specifically the expulsion of minority ions from the core at the sawtooth crash. The antenna loading is also observed to change synchronously with the central sawteeth. This surprising observation proves that the antenna loading is not determined solely be conditions in the plasma edge.

7.1.3 Measurement of PDI

During magnetic field ramps PDI was transiently observed on spectra from floating Langmuir probes on the limiters during fundamental minority heating in D(H). The PDI becomes large when the $f_{RF} = 3f_{CD} = 80$ MHz cyclotron harmonic layer is passing by the antenna Faraday screen. PDI was not seen to occur in L-mode. As harmonic layer moved outward, the PDI level rose quickly to maximum as it passed the Faraday screen, the dropped slowly away. Observation of PDI on the Langmuir probes was correlated with observation of energetic neutral Deuterium by the CX diagnostic. The observation of PDI did not correlate with production of impurities.

PDI was observed to occur during all heating scenarios, but at high levels only during second harmonic heating in D(H) at 2.8 and in D(^{3}He) at 3.7 T. In the latter scenario PDI was seen at the harmonics of the minority cyclotron frequency, while in all the other scenarios only harmonics of the majority cyclotron frequency are observed.

The PDI decay waves are identified as the Ion Bernstein Wave (IBW) and the Ion Cyclotron Quasi-mode (ICQ). The decay is caused by nonlinear mixing of the large polidal electric field associated with the fast (pump) wave. The spatial structure of the decay waves depends on the spatial structure of the pump wave and on the edge plasma temperature. The pump wave electric field is largest in the gaps between the

Faraday shields. The decay waves are also expected to be largest in the gaps between the Faraday shields.

7.2 Recommendation for Future Work

This research implies two other topics of research worthy of PhD. dissertations, and one topic worthy of a Masters thesis. The ASP data should be systematically compared to FSP data, and data from the Helium Beam probe, the edge Thomson Scattering system, the edge X-Ray array, and the the divertor probes to understand the variations of plasma parameters along field lines. These diagnostics rely to varying degrees on EFIT, and can be used to isolate problems in EFIT's calculation of flux surfaces.

The inner wall loop probes are necessary but not sufficient for the understanding of the global RF power balance. The recently installed Phase Contrast Imaging system can measure the power going into mode conversion at the $n_{\|}^2 = \mathcal{S}$ layer, and the soon-to-be-installed Diagnostic Neutral Beam will provide measurements of the majority T_i profile for the first time on C-Mod, via Charge-Exchange Recombination Spectroscopy. With the new 18-channel GPC providing T_e profiles with twice the spatial resolution as the old 9-channel GPC, there will be enough diagnostic information to overcome the absence of reliable measurements of the minority density and temperature, and find out how much RF power goes to ions, how much to electrons; how much to cyclotron damping at the minority fundamental, and how much to mode conversion; how the RF changes the central transport, and so on.

In future investigations of RF fields with Langmuir probes, there remain two issues to clear up. First, probes should be built that allow the stub cancellation technique to be effectively applied, and installed in regions where the RF fields are large, such as in the RF antenna side tiles. Second, the ASP should be redesigned to remove the probe tip—probe head capacitance, and allow the use of stubs. Once this can be done, then the radial structure of the decay waves from PDI can be quantified.

Appendix A

Langmuir Probes

A.1 Langmuir Probes

The variably-biased electrode is the most venerable of plasma diagnostic techniques, widely used for many years before a correct theory of its operation was worked out by Langmuir and Mott-Smith in 1924 [86], for which achievement the technique is now universaly known as the *Langmuir probe.* Langmuir probes have been used in a wide variety of configurations (swept, double, triple, emissive, etc.) in innumerable plasma genera, and have been the subject of many review articles and several books [87], [88], [9], [89].

A.1.1 Swept Langmuir Probes

In swept operation, there is one "knob" the experimentalist controls (the bias voltage V), and one output which contains information about the plasma (the probe current I). The two are related by

$$I = I_{sat}\left(1 - e^{-\frac{e(V-V_f)}{kT_e}}\right) , \tag{A.1}$$

where V_f is the potential at which the probe draws no current (the "floating potential"), and the ion saturation current I_{sat} is

$$I_{sat} = 0.61 n_e e c_s A_p \ . \tag{A.2}$$

Here $c_s = \sqrt{kT_e/m_i}$ and A_p is the area of the probe projected along the magnetic field. See chapter 3 of [9] for a modern derivation of these equations. From the dependence of current on bias voltage (the "probe characteristic") T_e, n_e, and V_f can be deduced. Other quantities, such as the electron pressure $p_e = n_e k T_e$, and the plasma potential $V_p \sim V_f + 3kT_e/e$, can then be derived from these.

Figure A.1 shows a schematic of the electronics which run the swept Langmuir probes on C-Mod, designed by Dr. Brian LaBombard. The probe current is measured by monitoring a voltage which appears across a resistor in series with the probe. The probe voltage is monitored on the probe side of the current monitor; the voltage monitor has an input impedance of greater than 400 $k\Omega$ to avoid loading the probe. On C-Mod, raw probe data is digitized in the form of two signals, (voltage vs. time) and (current vs. time). Figure A.2 shows raw data taken from one of the series of ASP scans which went into Figure 4.2. The first and second traces are the raw current and voltage data from one of the probes, showing one complete cycle of the 2 kHz bias voltage, from which two probe characteristics are created (third trace).

The fitting software, written by Dr. LaBombard, uses the most negative bias voltages to estimate the ion saturation current, then independently determines the floating potential. A fitting program then finds T_e by fitting an exponential to that part of the characteristic with bias voltages $V \leq V_{Max}$, where V_{Max} was eventually chosen to be 7 V. The fits and fit parameters for the two characteristics are included on the third trace.

Error analysis There is no simple way to arrive at the error in Langmuir probe measurements, which comes not only from noise in the raw data, but also from approximations and assumptions in the theory and even perturbations of the plasma

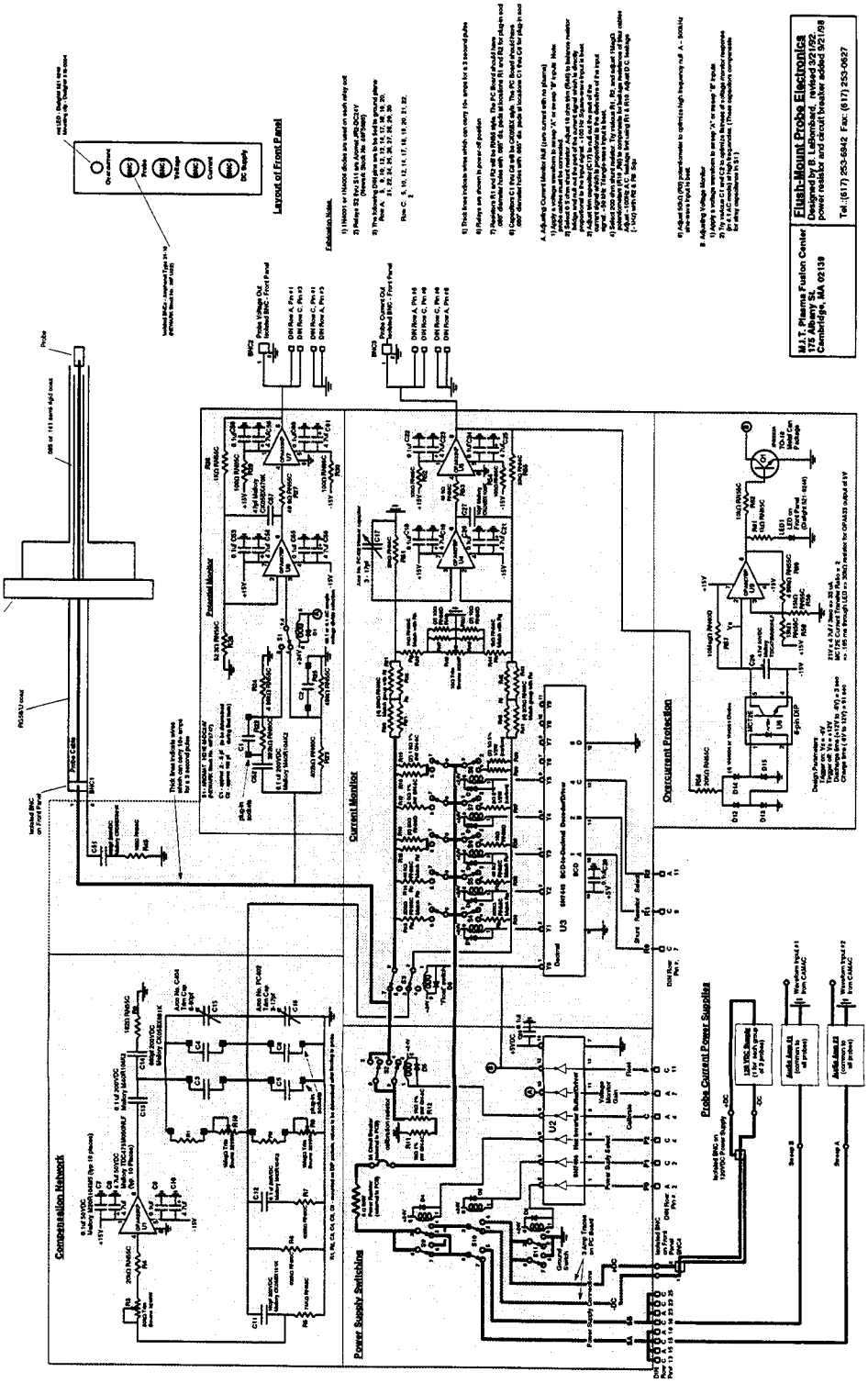

Figure A.1: Schematic of Langmuir probe controller

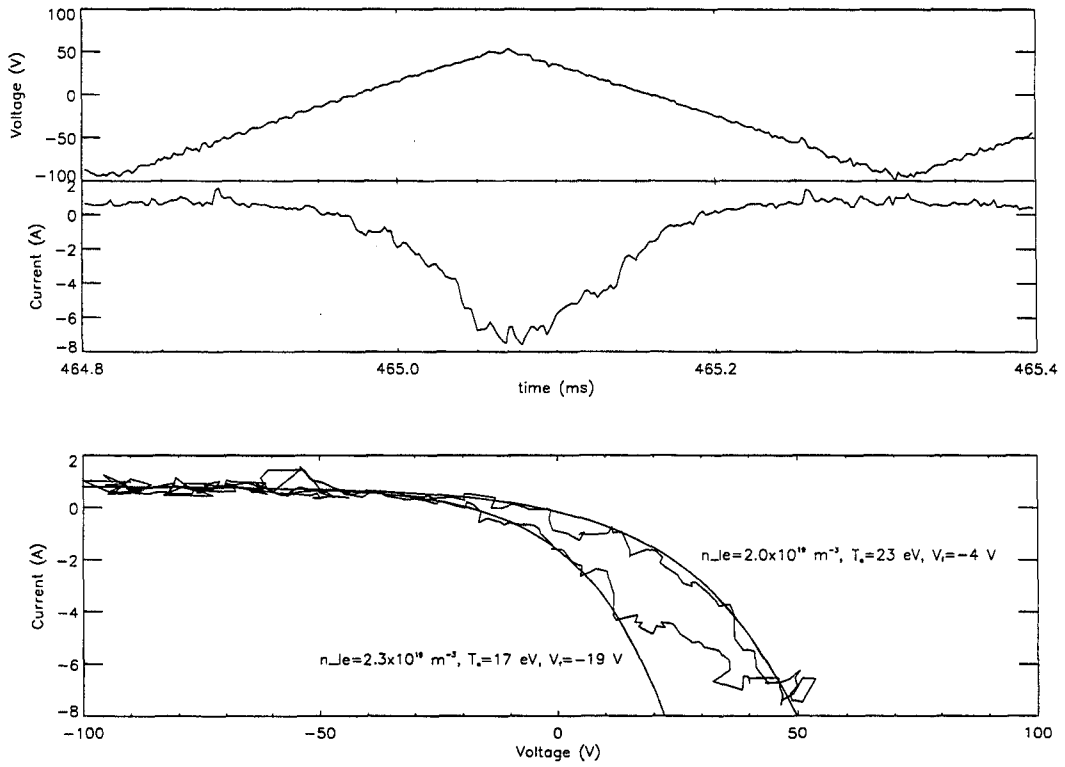

Figure A.2: Raw Probe Data and Characteristics

caused by the probe. The fitting program rejects sufficiently noisy traces as unfittable, and calculates errors for the parameters of the remaining fits. Since the plasma parameters are deduced from the exponential part of the I-V characteristic, their accuracy depends on the adherence of a comparatively small number of electrons, far out on the tail, to the Maxwellian distribution function. The presence of a suprathermal tail (of runaways, for example) would result in an incorrectly high estimate of T_e, and incorrectly low estimates of n_e and V_f.

Even on the exponential part of the IV curve, probes in the dense C-Mod edge plasma may still draw enough current to heat up, perhaps to the point where thermionic emission of electrons begins to distort the probe characteristic. This problem has been studied by Stangeby [90], who finds that secondary emission reduces the electron current by a factor of $1-\gamma$, where γ is the secondary electron emission coefficient, which depends on the probe material and its temperature. An effect of this sort would

produce an incorrectly high estimate of V_f (though n_e and T_e would not be changed).

The probe perturbs the plasma by depleting particles from the field lines it interrupts. These particles can only be replaced by cross-field diffusion. In the limit of no ionization in the SOL, the probe will deplete the density along a length

$$L = 8d^2 c_s / D_\perp \ ,$$

where d is the radial density fall-off scale length, $c_s = \sqrt{2kT_e/m_i}$, and $D_\perp$ is the cross-field diffusion coefficient, assumed to be dominated by ambipolar diffusion. If $L \geq L_c$, L_c being the connection length (measured along a field line) between the probe and the nearest material surface, the probe measurements will be unfathomably wrong.

The best tactic is to assume that the probe measurements are accurate to within a factor of two, and average over as many probe traces as possible to minimize fluctuations.

A.2 Sheath Rectification

Probe characteristics taken during RF heating are liable to noise and distortion due to the RF. The probe characteristic may be distorted in a predictable way due to rectification of the RF by the sheath. Suppose an RF bias voltage $\tilde{V} = V_1 \cos \omega t$ is applied to a Langmuir probe tip. The probe current may then be written [91]:

$$\frac{I}{I_{sat}} = 1 - e^{-\frac{e(V-V_f)}{kT_e}} \left(\mathcal{I}_0(z) + 2 \sum_{k=1}^{\infty} \mathcal{I}_k(z) \cos k\omega t \right) \ , \tag{A.3}$$

where $\mathcal{I}$ is a modified Bessel function, and $z = eV_1/kT_e$. The $\mathcal{I}_0$ term represents a DC electron current. The probe must be biased at a voltage negative by ΔV with respect to the true floating potential V_f in order to draw no net current. Setting $I = 0$ in Eq.

A.3 gives

$$\Delta V = V_1 - O(\ln V_1) \tag{A.4}$$

in the limit $eV_1 >> kT_e$.

The question remains of how to relate V_1 to a quantity associated with a plasma wave. The variation of plasma potential on a magnetic field line connecting two grounded material surfaces is studied in [49], [51]. Defining a zero-to-peak voltage $V_{RF} = \int ds E_{||}$, a the field line rises to a steady-state voltage V_0

$$V_0 = 0.6 V_{RF} \ , \qquad \frac{eV_{RF}}{kT_e} >> 1 \tag{A.5}$$

which serves to confine electrons and accelerate ions into the material surfaces terminating the field line. In Section 4.6 this relation was used to estimate the energy deposited by ions in the RF antenna and the limiters.

The fluctuating RF voltage causes the probe to trace out a portion of its characteristic on time scales much faster than the response time of the detection electronics, which therefore detect a non-zero increment in current. This increment appears as a spurious electron current for probe voltages well below the plasma potential. Figure A.3 models the distortion in a probe characteristic, and the decrement to the floating potential, caused by the RF; the electron temperature is 20 eV and the amplitude of the RF fluctuation is 40 V. This model is valid for RF frequencies $\omega_{RF} \leq v_{ti}/d \approx \omega_{Pi}$, where d is the thickness of the sheath. This is the condition that the typical ion has time to cross the sheath before the RF polarity changes.

In the C-Mod the plasma the amplitude of the RF fluctuation itself varies with time, and the RF fluctuations cause enhanced broadband noise; so that when the RF fluctuations are large the probe characteristics, in addition to being distorted as shown in Figure A.3, are also much noisier. The best sign that RF sheath rectification is taking place is an impossibly negative value for V_f.

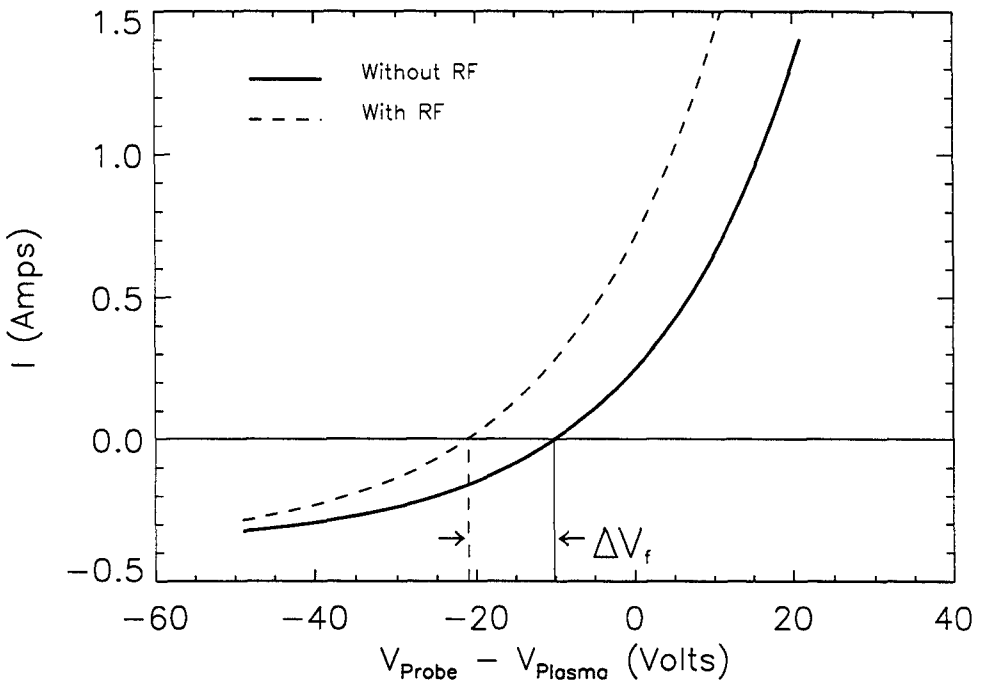

Figure A.3: Probe characteristic distorted by RF

A.3 Langmuir Probe: Floating

During the 1960's plasma turbulence came into vogue, and experimentalists evolved probe techniques capable of measuring fluctuations in I_{si} and V_f. It became important to address epistemological issues: how could one be sure that the fluctuations observed on a probe signal were related to the fluctuations in plasma quantities which would have existed had the probe not been inserted into the plasma? The problem was twofold. First, the plasma fluctuations might have an effective non-zero output impedance, so that the insertion of a probe into the plasma would "load" the plasma fluctuation, removing enough energy from it to significantly damp it, and leading to incorrectly low estimates of the fluctuation level. This would be caused by stray capacitances to ground, and the degree of underestimation would rise with increasing frequency as the impedance to ground decreased.

Second, the probe, with its attendant sheath, might somehow create spurious fluctuations, for which no simple model existed. For example, Langmuir probes biased

positive with respect to the plasma potential are known to generate electrostatic ion cyclotron waves in the sheath [89].

The best solution to the these problems turned out to be the development of the capacitive probe (eg. [92]), which presents an extremely high input impedance to the plasma. In paired comparison tests [93] it was found that indeed, the Langmuir probe signal dropped off relative to the capacitive probe signal above some critical frequency, which depended on plasma parameters; and that while the capacitive probe signal monotonically decreased with frequency, the Langmuir probe signal bottomed out and began to increase (exceeding the capacitive probe signal) above some second and higher critical frequency, which also apparently depended on plasma parameters.

Capacitive probes tend to be fragile, and no one has yet attempted to mount a capacitive probe on a reciprocating drive for use in a tokamak. Spectra from floating Langmuir probes are easy to take and can yield qualitative data about fluctuations at different frequencies, for example the relative magnitudes of the pump and decay waves in the parametric decay instability.

Bibliography

[1] J. Huba, *NRL Plasma Formulary*, Naval Research Laboratory, 1994.

[2] F. F. Chen, *Introduction to Plasma Physics and Controlled Fusion*, volume 1, Plenum Press, 2nd edition, 1984.

[3] J. P. Freidberg, *Ideal Magnetohydrodynamics*, Modern Perspectives in Energy, Plenum Press, 1987.

[4] T. H. Stix, *The Theory of Plasma Waves*, McGraw-Hill, 1st edition, 1962.

[5] J. Wesson, *Tokamaks*, Oxford Science Publications, 2nd edition, 1997.

[6] J. Freidberg, M. Greenwald, D. Gwinn, I. Hutchinson, B. Lipschultz, E. Marmar, D.B. Montgomery, R.R. Parker, M. Porkolab, J. Schultz, D. Sigmar, R. Thome, S.M. Wolfe, T. Yang, Alcator C-Mod Proposal, MIT Plasma Fusion Center Technical Report PFC/RR-85-18, 1985.

[7] M. Greenwald et al., *Phys. Rev Lett.*, **53**, 352 (1984).

[8] S. Wolfe, Personal communication, 1997.

[9] I. H. Hutchinson, *Principles of Plasma Diagnostics*, Cambridge University Press, 1987.

[10] L. Lao, H. S. John, R. Stambaugh, A. Kellman, and W. Pfeiffer, *Nucl. Fus.*, **25**, 1611 (1985).

[11] Y. Takase et al., Engineering Design and Analysis of the Alcator C-Mod Two-Strap ICRF Antenna, in *Proceedings of the 14th IEEE/NPSS Symposium on Fusion Engineering (San Diego, CA)*, 1992.

[12] M. Porkolab, Radio-Frequency Heating of Magnetically Confined Plasma, in *Fusion*, edited by E. Teller, Academic Press, 1981.

[13] T. Luke, *Measurements of Particle Diffusion Coefficients on Alcator C-Mod*, Ph.d. thesis, Massachusetts Institute of Technology, 1994.

[14] T. Hsu, *The Submillimeter Wave Electron Cyclotron Emission Diagnostic for the Alcator C-Mod Tokamak*, Ph.d. thesis, Massachusetts Institute of Technology, 1993.

[15] R. Guharay and D. Boyd, *RSI*, **61**, 3520 (1990).

[16] R. Granetz, I. Hutchinson, J. Gerolamo, W. Pina, and C. Tsui, *RSI*, **61**, 2967 (1990).

[17] M. May et al., *RSI*, **66**, 561 (1995).

[18] M. Graf, *Impurity Injection Experiments on the Alcator C-Mod Tokamak*, Ph.d. thesis, Massachusetts Institute of Technology, 1995.

[19] P. C. Stek, *Reflectometry Measurements on Alcator C-Mod*, Ph.d. thesis, Massachusetts Institute of Technology, 1997.

[20] J. C. Miller, Calibration and Parametric Study of the Alcator C-Mod Charge Exchange Neutral Particle Analyzers, Master's thesis, Massachusetts Institute of Technology, 1995.

[21] B. Labombard, B. Lipschultz, and D. Jablonski, First Results from the Divertor Probe Array in Alcator C-Mod, in *APS-DPP Conference, 1993 (St. Louis)*, 1993.

[22] B. Labombard et al., *Phys. Plas.*, **2**, 2242 (1995).

[23] S. V. Goeler, W. Stodiek, and N. Sauthoff, *Phys. Rev. Let.*, **33**, 1201 (1974).

[24] F. Wagner et al., *Phys. Rev. Lett.*, **49**, 1408 (1982).

[25] M. Keilhacker et al., *Plas. Phys. Cont. Fus.*, **26**, 49 (1984).

[26] P. O'Shea, *Measurements of ICRF Power Deposition and Thermal Transport with an ECE Grating Polychromator on the Alcator C-Mod Tokamak*, Ph.d. thesis, Massachusetts Institute of Technology, 1997.

[27] A. Hubbard et al., *Phys. Plasmas*, **5**, 1744 (1998).

[28] K. Burrell, *Phys. Plasmas*, **4**, 1499 (1997).

[29] J. Snipes et al., ELMs and Fast Edge Fluctuations in Alcator C-Mod, Technical Report PSFC/JA-97-23, Massachusetts Institute of Technology, 1997.

[30] N. Sauthoff, S. V. Goeler, and W. Stodiek, *Nucl. Fus.*, **18**, 1445 (1978).

[31] R. Granetz et al., *Nucl. Fus.*, **36**, 545 (1996).

[32] G. Cutsogeorge, Amplitude and Phase Detector for Radio Frequency Measurements, Technical Report PPPL-2550, Princeton Plasma Physics Lab, 1988.

[33] K. Shimizu, A. Hallil, and H. Amemiya, *Rev. Sci. Inst.*, **68**, 1730 (1997).

[34] F. Chen, Modern Uses of Langmuir Probes, Technical Report IPPJ-750, Institute of Plasma Physics—Nagoya University, 1995.

[35] S. Adam, *Microwave Theory and Applications*, Prentice-Hall, Inc., 1st edition, 1969.

[36] T. Fredian, J. Stillerman, and M. Greenwald, *RSI*, **36**, 9999 (1996).

[37] J. Stillerman, T. Fredian, K. Klare, and G. Manduchi, *Rev. Sci. Inst.*, **36**, 9999 (1996).

[38] B. Labombard and B. Lipschultz, *Nucl. Fus.*, **27**, 81 (1987).

[39] S. Braginskii, *Reviews of Plasma Physics*, **1**, 205 (1965).

[40] H. Gerhauser and H. Claassen, Calculation of Poloidal Rotation in the Edge Plasma of Limiter Tokamaks, Technical Report JUL-2125, Kernforschungsanlage Julich, IPP, 1987.

[41] R. V. Nieuwenhove and G. V. Oost, *Jour. Nucl. Mat.*, **162-164**, 288 (1989).

[42] S. Clement et al., Effect of ICRH on the JET Edge Plasma with Carbon and Beryllium Coated Limiters, Technical report, JET, 1990.

[43] M. Porkolab, Plasma Heating by Fast Magnetosonic Waves in Tokamaks, in *Advances in Plasma Physics, Symposium in Honor of T.H. Stix*, number 314 in Advances in Plasma Physics, American Physical Society, 1994.

[44] M. Brambilla, *Nucl. Fus.*, **14**, 327 (1974).

[45] M. Mayberry et al., *Nucl. Fus.*, **30**, 579 (1990).

[46] T. Fujii et al., *Fus. Eng. Des.*, **12**, 139 (1990).

[47] F. Perkins and R. Kluge, *IEEE Trans. Plas. Sci.*, **PS-12**, 161 (1984).

[48] T. Pedersen and R. Granetz, *Rev. Sci. Inst.*, (1998).

[49] D. D'Ippolito and J. Myra, *Phys. Plasmas*, **3**, 420 (1996).

[50] D. D'Ippolito, J. Myra, M. Bures, and J. Jacquinot, *Plas. Phys and Contr. Fus.*, **33**, 607 (1991).

[51] J. Myra, D. Dippolito, and M. Gerver, *Nucl. Fus.*, **30**, 845 (1990).

[52] F. Perkins, *Nucl. Fus.*, **29**, 583 (1989).

[53] J. Jacquinot, Effect of icrh on the edge, Unpublished work, 1990.

[54] T. Tanaka, R. Majeski, D. Diebold, and N. Hershkowitz, *Nucl. Fus.*, **36**, 1609 (1996).

[55] S. Wuktich, D(^{3}He) Heating in Alcator C-Mod, in *Second EPS Europhysics Topical Conference on RF Heating and Current Drive of Fusion Devices (Brussels)*, 1998.

[56] T. Stix, *Nucl. Fus.*, **15**, 737 (1975).

[57] K. Budden, *Radio Waves in the Ionosphere*, Cambridge University Press, 1st edition, 1961.

[58] A. Ram, A. Bers, S. Schultz, and V. Fuchs, *Phys. Plas.*, **3**, 1976 (1996).

[59] J. Rost, *Fast Ion Tails during Radio Frequency Heating on the Alcator C-Mod Tokamak*, Ph.d. thesis, Massachusetts Institute of Technology, 1998.

[60] M. Brambilla, *Nucl. Fus.*, **28**, 549 (1988).

[61] G. Hammett, *Fast Ion Studies of Ion Cyclotron Heating in the PLT Tokamak*, Ph.d. thesis, Princeton University, 1986.

[62] P. Bonoli et al., ICRF Heating Scenarios in Alcator C-Mod, in *Proceedings of the 16th IAEA International Conference on Fusion Energy (Montreal)*, volume 3, 1996.

[63] P. Bonoli, 1999, Personal communication.

[64] S. Kim, D. Brower, W. Peebles, and J. N.C. Luhmann, *Phys. Rev. Let.*, **60**, 577 (1988).

[65] M. Foord and E. Marmar, *Nucl. Fus.*, **25**, 197 (1985).

[66] D. Mossessian, 1998, private communication.

[67] U. W. L.-G. Eriksson, T. Hellsten, *Nucl. Fus.*, **33**, 1037 (1993).

[68] M. Ono, M. Porkolab, and R. Chang, *Phys. Fluids*, **23**, 1673 (1980).

[69] R. Pinsker, C. Petty, M. Mayberry, M. Porkolab, and W. Heidbrink, *Nucl. Fus.*, **33**, 777 (1993).

[70] M. Saigusa et al., Observation of Parametric Decay Waves During Second Harmonic ICRF Heating Experiment in JT-60, in *Proceedings from 8th Topical Conference on RF Power in Plasmas, Irvine 1989*, page 326, AIP, 1989.

[71] G. V. Oost et al., *Fus. Eng. Des.*, **12**, 149 (1990).

[72] R. V. Nieuwenhove, F. Durodie, R. Kock, and G. V. Oost, *Fus. Eng. Des.*, **12**, 203 (1990).

[73] M. Porkolab, *Fusion Eng. and Des.*, **12**, 93 (1990).

[74] S. Chiu, *Phys. Fluids*, **31**, 3295 (1988).

[75] P. Blanc et al., Experiments at the Lower Hybrid Frequency in the WEGA Tokamak, in *Proceedings from the 6th IAEA Conference on Plasma Physics and Controled Nuclear Fusion Research (Berchtesgaden)*, volume 3, 1976.

[76] M. Porkolab, S. Bernabei, W. Hooke, R. Motley, and T. Nagashima, *Phys. Rev. Lett.*, **38**, 230 (1977).

[77] R. V. Nieuwenhove et al., *Nucl. Fus.*, **28**, 1603 (1988).

[78] P. Briand et al., Non-linear Effects and Plasma Heating by Lower Hybrid Waves in the PETULA Tokamak, in *Proceedings from the 7th IAEA Conference on Plasma Physics and Controled Nuclear Fusion Research (Innsbruck)*, volume 1, 1978.

[79] M. Bures et al., *Bull. Am. Phys. Soc.*, **33**, 2032 (1988).

[80] G. Vekstein, *Physics of Continuous Media*, Adam Hilger, 1st edition, 1992.

[81] M. Ono, M. Porkolab, and R. Chang, *Phys. Fluids*, **23**, 1656 (1980).

[82] I. Lehrman, P. Colestock, and E. Jaeger, *Nucl. Fus.*, **30**, 1399 (1990).

[83] M. Porkolab and R. Chang, *Phys. Fluids*, **13**, 2054 (1970).

[84] R. Chang and M. Porkolab, *Phys. Fluids*, **15**, 297 (1972).

[85] Y. Takase et al., *Phys. Rev. Lett.*, **53**, 274 (1984).

[86] I. Langmuir and J. Harold Mott-Smith, *General Electric Review*, page 449 (1924).

[87] F. Chen, Electric Probes, in *Plasma Diagnostic Techniques*, edited by R. Huddlestone and S. Leonard, Academic Press, 1965.

[88] J. Swift and M. Schwar, *Electrical Probes for Plasma Diagnostics*, American Elsevier, New York, 1st edition, 1969.

[89] N. Hershkowitz, How Langmuir Probes Work, in *AIP–Plasma Diagnostics: Discharge Parameters and Chemistry*, edited by O. Auciello and D. Flamm, volume 1, page 113, Academic Press, 1989.

[90] P. Stangeby, *Phys. Fluids*, **27**, 682 (1984).

[91] M. Abramowitz and I. Stegun, *Handbook of Mathematical Functions*, Dover, 1st edition, 1965.

[92] J. Schmidt, *Rev. Sci. Inst.*, **39**, 1297 (1968).

[93] J. Roth and W. Krawczonek, *Rev. Sci. Inst.*, **42**, 589 (1971).